A HIERARCHICAL INITIATION MECHANISM APPROACH TO MODELING FATIGUE LIFE VARIABILITY IN 35CO-35NI-20CR-10MO ALLOY MEDICAL GRADE FINE WIRE

A Thesis
Submitted to the Faculty
of
Purdue University
by
Jeremy E. Schaffer

In Partial Fulfillment of the
Requirements for the Degree
of
Master of Science in Mechanical Engineering

August 2007
Purdue University
West Lafayette, Indiana

For Krista, my amazingly patient and endearing wife, and Austin, who deftly mastered life at broadband pace while I travailed in mastering but one feat.

ACKNOWLEDGMENTS

I would like to thank Professor Eric Stach, whose knowledge in analytical electron beam techniques are second to none, for his invaluable tips on SEM methods. I would also like to thank Professor Benjamin Hillberry, whose laudable works in fatigue research extend through many decades of the latter century, for his wealth of insightful comments and purposeful guidance. My thanks to Professor Grandt and Professor Craig for serving on my advisory committee and for their help reviewing this thesis.

Over the course of my research, many other individuals offered crucial input that maintained the forward progress needed to procure success. These individuals deserve acknowledgement and include:

Dmitri Zakharov, for keeping the S4800 operational by pulling numerous samples from the SEM chamber dropped by disheveled graduate students and for his excellent training. Thanks to Jan Eberle for keeping all the SEMs running smoothly and answering countless questions, and for all his efforts on the ESEM we couldn't use this semester. Thanks to Bob Boling for machining the precision parts no one else cared to attempt (at least on the "languorous" equipment of the FWM machine shop). Thanks to Jim Meyer for offering a hand on countless items. Thanks to Professor Keith Bowman in Materials. Thanks to Shawn Chaney and his Metlab crew for their support in many facets of materials analysis. Thanks to Kurt Schenk for his valuable input in many conversations. Thanks to Pete McIntyre at Medtronic for his perspective on similar problems. Thanks to Brandon Liechty and Kym Crandell for their meticulous review of this document. Thanks to Mark Michael, Larry Kay, Chuck Carrel and other FWM colleagues for giving me a sounding board against which to develop logical thought and research direction.

I am especially indebted to my wife for her love, support, sample preparation, document review, and perhaps most of all her patience as she cared for her student husband and our precious little man Austin.

It is with sincere gratitude that I thank Scott Glaze, Mark Michael, Bob Myers and the staff of Fort Wayne Metals for funding this entire project and for providing so many resources, without which this work would not have been completed. Most importantly, I thank The Lord Jesus Christ for His many blessings and for granting me every need and the patience to see this through.

TABLE OF CONTENTS

LIST OF TABLES

LIST OF FIGURES

Figure Page

NOMENCLATURE

α	life exponent
$\Delta\tau$	applied shear stress range
ΔK	applied stress intensity range
Δ_{ϵ_p}	applied plastic strain range
ϵ_f'	fatigue ductility coefficient
$\frac{da}{dN}$	incremental crack growth rate
λ	universal constant
μ	metallic matrix shear modulus
μ'	constituent particle shear modulus
ν	Poisson's ratio
σ_{ys}	0.20% offset yield strength
σ_e	fatigue limit
σ_y'	cyclic yield stress
ξ	inclusion size
d_0	reference dislocation barrier spacing
D_0	reference grain size
K_Q	provisional stress intensity per ASTM E399
L_C	RBT chuck-to-bushing center distance
n^1	stage I crack growth exponent
n^2	stage II crack growth exponent
N_b	number of cycles to breakthrough
N_f	number of cycles to failure
N_i	number of cycles comprising initiation life
R_{mod}	modified, applied stress ratio
S_{max}	maximum applied stress

S_{min}	minimum applied stress
S_{R_0}	maximum residual surface stress
S_{uts}	ultimate tensile strength
S_a	alternating stress amplitude
S_e	endurance stress at $> 100M$ cycles
W_s	specific slipband fracture energy
AFM	Atomic Force Microscopy
b	fatigue ductility exponent
c	crack half length
CDF	Cumulative Distribution Function
CNIF	Crack Nucleation Intensity Function
d	grain size
D	grain size
E	Young's elastic modulus
ESEM	Environmental Scannign Electron Microscope
F	stress intensity geometry factor
FASTRAN	Fatigue crack growth STRuctural Analysis computer program
FEA	Finite Element Analysis
FE-SEM	Field Emmission SEM
FIB	Focused Ion Beam
GS	Grain Size
H	strain hardening coefficient
h	slipband width
HCF	High Cycle Fatigue (megacycle regime)
IHF	Initiation Hierarchy Function
k	friction stress of dislocation motion
LCF	Low Cycle Fatigue
LEFM	Linear Elastic Fracture Mechanics
M	Taylor factor

N	number of cycles
psb	persistent slip band
q	notch sensitivity factor
R	applied stress ratio $\frac{S_{min}}{S_{max}}$
RBT	Rotary Bend fatigue Testing
S	remotely applied stress
s	dislocation cell size
SENT	Single Edge Notch Tension
TEM	Transmission Electron Microscopy
UHCF	Ultra High Cycle Fatigue (gigacycle regime)
VAR	Vacuum Arc Remelt
VIM	Vacuum Induction Melt

ABSTRACT

Schaffer, Jeremy E., MSME, Purdue University, August, 2007. A Hierarchical Initiation Mechanism Approach to Modeling Fatigue Life Variability in 35Co-35Ni-20Cr-10Mo Alloy Medical Grade Fine Wire. Major Professors: Dr. Eric Stach, School of Materials Engineering and Dr. Benjamin Hillberry, School of Mechanical Engineering.

Many cardiac stimulation lead systems use wires comprising alloy MP35N™[1] or a clean melt version known as 35N LT®[2]. At an average human heart rate of sixty beats per minute, these wire systems experience greater than thirty million stress cycles each year. A critical factor in the design of such systems is the understanding of total fatigue life and life variability.

Previous studies have shown that failures in the MP35N alloy system used in these applications tend to fail at constituent particle sites and extrinsic surface defect structures. Further work has shown that under certain low cycle fatigue loading conditions, the lifetime variability can be partially explained by variability in the size of these defects. This study was conducted to further examine causes of lifetime variability and provide a framework for a probabilistic lifetime prediction model. An additional goal was to elucidate hierarchical, microstructural size scale dependent, crack initiation mechanisms.

Rotary beam fatigue testing was performed to failure on a total of 440 MP35N and 35N LT specimens representing three different average grain sizes, four states of previous strain hardening and several test stress levels. Samples were examined using high resolution scanning electron microscopy to determine crack initiation mechanisms, dislocation cell spacing, crack nucleating particle sizes, dislocation barrier spacing, and to infer initiation life from striation measurements. Fatigue crack initiation life

---

[1] MP35N™ is a trademark of SPS Technologies, Jenkintown, PA, USA

[2] 35N LT® is a registered trademark of Fort Wayne Metals Research Products Corporation, Fort Wayne, IN, USA

in 177 μm fine wire was found to comprise less than 10% of total life beyond 10^6 cycles .

Stochastic defect state variables were fit to statistical fitting functions and randomly selected using Monte Carlo methods as input together with deterministic data to an initiation life model. The results were then sorted for maximum crack nucleation potential, and output as a total fatigue life and life variability prediction model. The model generally yielded conservative total life estimates at low failure probability and good variability prediction.

1. INTRODUCTION

1.1 Fatigue in the Medical Device Industry

Reasonable fatigue lifetime prediction is critical in the design of nearly all engineering structures that will withstand variable load conditions. Lifetime prediction becomes even more important where human life is dependent upon the structure's survival. Most implantable medical devices are designed to reside in the human body for extended periods of time, and are often subjected to fluctuating mechanical load conditions. In order to make robust material selection decisions, a medical device design engineer should possess a thorough understanding of fatigue failure mechanisms and lifetime variability. Ideally, this designer should also have access to a model capable of predicting probability of failure for given design criterion.

The design of an implantable cardiac rhythm management (CRM) device is a rigorous process and must include conservative estimates for anticipated product lifetime. A CRM system comprises three primary components: the hermetically sealed control unit including battery and generator, the charge delivery system or conductor lead, and the distal electrodes for direct stimulation of the target site within the heart [1]. These components are used in implantable cardioverter-defibrillators (ICD) for the primary treatment of ventricular tachycardia, in pacemakers for the treatment of bradycardia, and in pulse generators to deliver cardiac resynchronization therapy (CRT) [2].

Failure of various CRM system components is anticipated through patient checkup. This practice is evidenced by manufacturer-recommended quarterly device inspection follow-up visits [2]. The components most susceptible to premature failure include the conductor lead and the battery, each with a typical lifetime of approximately three to eleven years. A salient difficulty in today's devices is that the longevity of the lead cannot be predicted and it does not typically give simple indicators that it is nearing the end of its life [2].

Most conductor leads that are in use today consist of a multilumen silicone or polyurethane passage that contains relatively low impedance, wire based, micro-cable or helical coils [3]. The primary structural component of the conductor itself comprises high strength MP35N, 35N LT or a silver cored composite wire of MP35N or 35N LT [4–6]; failure of this component will result in high circuit impedance and compromised device performance. The individual coil or cables typically receive a conformal fluoropolymer coating in addition to the multilumen jacketing. An example of this construction technique as well as pictures of some of today's state-of-the-art leads are shown in Figures 1.1 through 1.3.

Various studies [3, 7–11] have incited polymer insulation degradation as the dominant mode of lead failure, while only a few directly discuss mechanical fracture of the conductor [3, 11, 12]. There are known predictors of insulation failure, such as a reduction in the global lead impedance over time [9]. There are not, however, any known, robust, material-related predictors of imminent mechanical failure in these types of fine wire lead systems.

1.2 Research Objectives

The overall goal of this research was to characterize the microstructural parameters that are important in determining total fatigue life and life variability in fine medical wire for high fatigue applications. The implantable alloy system chosen for this investigation was selected for its widespread use in the field of CRM technology with the expressed intent of bettering the design capability for such lifesaving devices.

There are two general methodologies that are used when trying to describe total fatigue life and life variability in metallic materials. One approach is to build large repositories of fatigue life data sets. This information is then fit to various empirical relationships and used to calculate life at a given set of loading conditions. Methods corresponding to this type of analysis include the common stress-life, and strain-life models as well as the more recent fracture mechanics approaches for crack containing materials [13]. While these tactics provide a useful guide for total life determination, they do little to shed light on the influence of microstructural parameters such as inclusion and grain size on total fatigue life, particularly in the high cycle regime most applicable to medical device implants.

Recent work [13–17] has looked at both structural aluminum and medium and high strength steel alloy fatigue life variability from an initial discontinuity state perspective. These studies have shown good life correlation to the statistical size distribution of constituent inclusion particles. The foundation of such efforts was that fatigue cracks began from the first stress cycle and continued to failure, thus allowing life prediction entirely on the basis of crack propagation. In a similar study [18], this stochastic modeling technique was applied to the MP35N alloy system in the low cycle regime with good success. Further examination of lifetime data under high cycle conditions has shown that total life and variability in fine medical wire are driven by mechanisms other than crack propagation. The dearth of information in the area of microstructural fatigue factors and modeling techniques for high strength fine wire materials has been recognized by other authors [19] and was the impetus for the present study.

The specific objectives were to:

- Analyze fatigue initiation mechanisms under various material and load conditions and provide evidence as to what the primary life-influencing factors are.
- Develop a hierarchical model that describes the dominant initiation mechanism based on microstructural, material, and loading input conditions and provide estimates of total lifetime and lifetime variability.
- Verify the model results by comparison to historical and current wire fatigue data.

- Provide a statistical comparison of total inclusion populations to the crack-nucleating inclusions.

1.3 Organization

This thesis covers a broad spectrum of information and is divided into seven chapters. The next chapter provides the historicity for this endeavor in the form of a literature review including some background on the origin and current use of the alloy under investigation. The goal of Chapter 3 is to present the model framework and is divided into sections on probabilistic and deterministic variables, hierarchy of initiation mechanisms, and finally the hierarchy of life determination. The experimental design and procedure including mechanical testing and x-ray residual stress determination are detailed in Chapter 4. Support for the research objectives comprising results and a discussion of the results is contained in Chapter 5. The final primary chapter (chapter 6) provides concluding thoughts and ideas for further study. Chapter 7 finishes with insight into some incomplete, nonetheless interesting, experimental procedures.

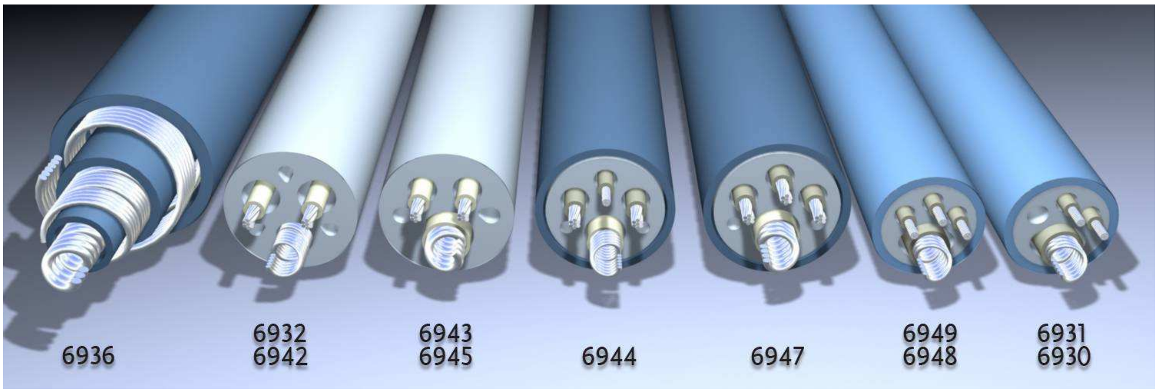

Figure 1.1. Multilumen lead design progression, incorporating MP35N coil and cable elements, Courtesy Medtronic, Inc.

Figure 1.2. Steroid-eluting, quadrupolar Linox SD active fixation lead, Courtesy Biotronik, gmbH.

Figure 1.3. Steroid-eluting, quadrupolar Linox SD active fixation lead tip and shock coil, Courtesy Biotronik, gmbH.

2. BACKGROUND

2.1 Failure in Cardiac Rhythm Management Leads

Failure of a CRM device can occur when any of the subsystems required for proper therapy breakdown. The three primary components comprise the hermetically sealed control unit including battery and generator, the polymer insulated conductor lead, and the distal shock, sensing, or pacing electrodes for stimulation of the target site within the heart. Components such as the charging capacitors tend to fail with some predictability. Technicians are able to read duty cycle information from the ICD memory and diagnose when circuit components should be replaced. Voltage levels can be tested to determine the state of the batteries [2]. Studies have shown that, in some cases, lead insulation failure is precluded by a decrease in global lead impedance [9].

Lead wire substrate prognostics are more difficult. Periodic impedance testing of the leads indicates whether they are intact but does not generally yield good information on their susceptibility to imminent fracture [7]. Despite significant advances in technology, several studies [8, 20, 21] have demonstrated the present day threat of unexplained lead malfunction. A chest x-ray of an *in vivo* multiple lead fracture is depicted in Figure 2.1. In part, such occurrence is due to the unknown nature and unexplained variability of fatigue failure. Lead longevity is largely dependent upon stochastic material structure-property relations; greater knowledge at the material level will improve design decisions and increase the probability of survival. Better modeling techniques could potentially reduce new product cycle times, increase safety margins, and promote the development of fatigue resistant, next generation lead systems.

2.2 Superalloys in Industry

The first superalloy was created and patented by Paul Merica in 1926 when he added a small amount of aluminum to a nickel chromium alloy [22]. Further variants of this were created for elevated temperature service using elements such as cobalt, nickel and iron with small additions of rare earth metals to promote high temperature strength phases. Most superalloys possess a highly complex microstructure that is further confounded by the presence of many secondary phase and particle dispersions. This complexity is largely responsible for the material characteristics, such as high temperature resistance to dislocation motion and accompanying plastic deformation, that provide value to industry [23].

2.2.1 Aerospace

The MP35N alloy system was first derived in 1965 by SPS Technologies for use as a high strength, fatigue resistant fastener and was the first to achieve a tensile strength in excess of 1800 MPa while maintaining good corrosion resistance and a relatively high service temperature of 400C. Soon after development, MP35N was used in the U.S. space program as a tie rod bolt material in development of the first shuttle spacecraft [23]. Today MP35N is used as a fastener in many aerospace applications including most public and private jet aircraft.

2.2.2 Sour Gas Wells

The National Association of Corrosion Engineers (NACE) recommends materials for use in various environmentally aggressive environments. MP35N is well known in the petrochemical industry and possesses the greatest strength of the recommended alloys listed in NACE specification MR0175 on sulfide stress cracking resistant materials for oil equipment. MP35N is most commonly used for the conduit piping in wells containing significant concentrations of gaseous hydrogen sulfide.

2.2.3 Medical Devices

In the late 1950's, Fort Wayne Metals (FWM) founder and researcher Ardelle Glaze discovered a high strength and electrically conductive wire system could be constructed using a brazed combination of stainless steel and phosphor bronze. This composite material, patented in 1964 is known as drawn brazed strand (DBS) and was originally conceived to solve a fatigue issue in the paper making industry. The excellent fatigue life, strength, and electrical conductivity of DBS also rendered it a prime candidate for the emerging bioconductor market. DBS was used as an implantable lead wire by GE beginning in the mid 1960's through the mid 1970's for all of its pacemakers. Further improvements in bioconductors were made possible by the introduction of MP35N-based, drawn filled tube (DFT®[1]) composite wire in 1985 [24]. DFT wire, possessing a high strength MP35N superalloy jacket and a conductive silver core, became an important component in high energy defibrillation leads by the early 1980's in the first-ever ICD systems.

2.2.4 The ASTM F562 Designation

The ASTM F562 alloy system was originally engineered for use as a high strength and fatigue resistant macroscopic fastener alloy, not as a material to serve the medical industry [23]. As a large scale fastener, the presence of 5 to 20 micron nonmetallic inclusions in the alloy is not necessarily deleterious to performance. In the past two decades, the system has been designed into medical devices typically as a 12.5 to 500 micron diameter fine wire. Many of these devices are intended for permanent or semi-permanent human implantation, thus increasing the need for microcleanliness control. A new variant of the F562 system, known as 35N LT, was commercially introduced in 2003 directly in response to this need. The 35N LT system is processed using carefully controlled melt techniques that eliminate TiN particle forming elements and effect a significant downward shift in the inclusion size distribution [4, 18]. The

---

[1] DFT® is a registered trademark of Fort Wayne Metals Research, Fort Wayne, IN, USA.

nominal chemistry of standard MP35N and improved 35N LT are shown in Table 2.1. 35N LT has recently been approved for use in devices ranging from implantable pacemakers to neurological sensing and stimulation devices.

Recent technological advances have dramatically improved the fatigue life of today's devices. Modern components, however, still share many common characteristics with early prototypes. The first transistorized, external, battery powered pacemaker was developed by Earl Bakken in 1957 [25]. These first generation devices used 300 series stainless steel leads and were highly susceptible to fatigue and corrosion assisted fatigue failure [1]. In 1970, it was difficult if not impossible to predict when a lead would fail. In 2007, we have this statement [2] from one of today's preeminent lead manufacturers:

> ...a lead's longevity cannot be predicted nor are there simple indicators that a lead is approaching the end of its service life.

In order to improve upon this statement, we need to continue to develop a better understanding of how and why fatigue cracks in lead wires initiate, grow and ultimately result in mechanical failure.

2.3 Evolution of Fatigue Theory

In 1860, the first systematic investigations of fatigue life were carried out by Sir William Airbairn and August Woehler on railroad axle materials [26]. One of the first tools to be used in designing against fatigue failure was derived by Woehler from these early studies, the stress-cycle life or S-N curve. It is interesting today that, despite many advances in our fundamental understanding of fatigue, perhaps the most valuable results of our work are the large repositories of this type of data.

Modern rationale on the origin of fatigue cracks in metal was signficantly advanced by the discovery of the crystalline nature of such materials by Ewing and Rosenhain in 1899 [27]. Professor J.A. Ewing later surmised that the fatigue cracks occurred along broadened slip-bands and coalesced with neighboring cracks [28]. Though misjudged to some degree in ascribing crack formation to boundary attrition, Ewing's literary and micrographic depiction of what we know today to be slip band surface protrusions was well ahead of its time and remains at the forefront of modern research. In 1923, researchers H.J. Gough and D. Hanson [29], in reference to slip activation, stated that failure in static tension and repeated stresses was preceded by the exact same process and proceeded to set forth what they believed to be a single unifying theory of fatigue. Despite their claim nearly a century ago, an all encompassing fatigue failure theory is yet to be realized.

In 1921 A.A. Griffith [30] introduced the energy based concept of strength reduction in brittle material due to the presence of sharp material inhomogeneities or cracks. Griffith's milestone document, *The phenomena of Rupture and Flow in Solids*, would define the field of fracture mechanics later to be refined by G.R. Irwin through introduction of the stress intensity factor, K, and the critical stress intensity factor, K_C, as a material property. Resulting from the concept of a stress intensity driven crack front, a significant step forward in fatigue life prediction was proposed by Paris, Gomez and Anderson in 1961 [26]. In this treatise, the crack growth rate was proposed to follow a relatively simple power law equation given by:

$$\frac{da}{dN} = C\Delta K^m \tag{2.1}$$

where $\frac{da}{dN}$ is the crack growth rate, K is the stress intensity range and C and m are experimentally derived constants. Most crack growth data today are presented as prescribed by Paris according to a similar, perhaps modified, power law relationship. The simple Paris curve fit does not provide stress ratio, crack closure, or geometric size-scale influence, and does not allow for mean stress effects or a lower stress intensity threshold. The Paris relation provides incomplete similarity and has been shown [31] to be dependent upon relative crack length scale and the loading asymmetry or stress intensity ratio, R. The Paris relationship oversimplifies the tortuous and complex behavior of a propagating crack front, nonetheless, it certainly reduces experimental burden by allowing crack propagation data to be normalized for a given set of conditions and, with discretion, applied to other cases.

The treatment of fatigue crack nucleation life, or the life before a detectable crack emerges, was discussed greater than 100 years ago, but not treated in a quantitative manner until the latter half of the 20th century [26]. This was largely due to emerging microanalysis techniques including scanning electron microscopy (SEM), atomic force microscopy (AFM), transmission electron microscopy (TEM), and more recently focused ion beam (FIB) and high resolution field emission SEM. These techniques have lead to many recent studies on fatigue crack propagation rates [13–17], crack initiation features [32–40], fatigue crack arrest behavior [41], and many other aspects that were only postulated in the minds of the early researchers. SEM became a prevalent analytical tool primarily in the years following WWII when research was largely focused on the subject of national defense [26]. For several decades following the war, the primary focus was applied to aircraft structural metals including aluminum and magnesium alloys, high strength steels, and later to superalloy systems that were used for turbines and aerospace fasteners.

Fatigue modeling involves a high degree of unpredictability; statistics is able to deal quantitatively with these uncertainties. The statistical nature of fatigue failure was hinted at by Gough [29] in the 1920's, and later by A.M. Freudentahl [42] in 1946. Analytical models such as the deterministic crack growth program developed by Newman [43], known as FASTRAN, benefits from probabilistic input parameters in the prediction of lifetime scatter. Statistical models range from the simplistic phenomenological representation of lifetime scatter using various distribution fitting functions (e.g. Weibull, log-normal, etc.) to complex multivariate schemes utilizing both variable and deterministic microstructural input parameters [33, 35].

2.3.1 Fatigue Initiation Life Models

Up until approximately 1980, there existed two basic principles used to predict fatigue initiation: (*i*) stress-life and (*ii*) strain-life equations such as the well known Coffin-Manson relation:

$$\frac{\Delta\epsilon_p}{2} = \epsilon_f' N_f^b \tag{2.2}$$

where $\Delta\epsilon_p$ is the plastic strain range, ϵ_f' is the fatigue ductility coefficient and b the fatigue ductility exponent. These relationships are extremely useful in relating lifetime data to given load conditions for a specific material type, geometry, microstructure, and environment. These are, however, entirely phenomenological expressions, and do not elucidate the effect of variable microstructural parameters on expected life.

In the last twenty years researchers have begun to quantify fundamental microstructural parameters that activate and impede the fatigue failure process. In 1981 Tanaka and Mura [44], set forth a dislocation based fatigue crack initiation model for the treatment of microstructural-impingement-based nucleation sites. The dislocation-dipole model was given by:

$$(\Delta\tau - 2k)N_i^{1/2} = \left[\frac{8\mu W_s}{\pi d}\right]^{1/2} \tag{2.3}$$

where N_i is the crack initiation life (cycles), $\Delta\tau$ is the shear stress range (MPa), k is the friction stress of dislocation (MPa), μ is the shear modulus (MPa), d is the grain size (μm) and W_S is the specific fracture energy per unit area along the slipband. A similar version of this model was given in 2003 by K.S. Chan [35] for inclusion based impingement using:

$$(\Delta\sigma - 2Mk)N_i^{\alpha} = \left[\frac{8(\mu - \mu')}{\lambda\mu'}\right]^{1/2} \left[\frac{M\mu h^2}{d(h+d)}\right] \left[\frac{c}{\xi}\right]^{1/2} \tag{2.4}$$

where $\Delta\sigma$ is the applied stress range (MPa), M is the Taylor factor, α is the life exponent, μ' is the shear modulus of the inclusions (MPa), λ is the universal constant, h is the slipband width (μm), d is the grain size (μm), c is the crack half-length or crack depth at intiation (μm), and ξ is the inclusion size (μm). Continuing from these efforts, Enright and Chan [45] extended the model to include quantitative information about the crack size at initiation and ultimately introduced the model expression:

$$(\Delta\sigma - 2\sigma_e)N_i^{\alpha} = \left[\frac{8M^2\mu^2}{\lambda\pi(1-\nu)}\right]^{1/2}\left(\frac{h}{D}\right)\left(\frac{c}{D}\right)^{1/2} \tag{2.5}$$

where σ_e is the fatigue limit (MPa), ν is the Poisson's ratio, and D is the grain size (μm).

2.3.2 Fatigue Crack Growth Based Models

The distinction in fatigue between crack initiation and crack growth has been the subject of debate in numerous publications on fatigue mechanics [17, 18, 35, 39, 43, 44]. One of the first quantitative fatigue life relationships was the power law equation devised by Paris in the early 1960's [26], still in use today to fit crack tip stress intensity to fatigue crack growth (FCG) data. FCG data are of particular importance to researchers involved in damage tolerant design for military aircraft who are generally interested in studying remaining life at measurable macroscale crack lengths [46].

Through the mid 1970's, nearly all FCG data were related to what we now know to be the microstructurally and physically long crack regime. In 1975, Pearson [47] observed that very short cracks grew faster at lower stress intensity levels than corresponding long cracks. Beginning from Pearson's discovery through today, researchers [35, 48–52] have significantly advanced our understanding of small crack phenomenon. Newman [43] proposed a unified approach to fatigue life prediction that assigns the entire lifetime to the propagation regime through short to long crack length and finally to breakthrough. The deterministic, crack growth-based life prediction code written by Newman, FAtigue Crack Growth STRuctural ANalysis or FASTRAN, has been successfully employed by numerous researchers [13–18] using a variety of materials ranging from 2024-T3 Aluminum to high strength 35Co-35Ni-20Cr-10Mo superalloy.

Existing FCG life models have been shown to work well for predicting, what is defined here as low cycle fatigue (LCF), but have shown only limited applicability to the high cycle fatigue (HCF) through ultra high cycle fatigue (UHCF) regimes. The reason for this is tied to the underlying assumption of a limiting stress intensity threshold range below which cracks will not propagate. Without the incorporation of other failure mechanisms, or modes of low stress damage accumulation, this technique results in a perfectly horizontal fatigue limit below which the model will always yield infinite life.

2.3.3 Total Fatigue Life Models

A greater *ab initio* understanding of fatigue damage accumulation, namely that of dislocation pileup at barrier structures and the formation of persistent slip bands (PSB's), has resulted in several models within the last decade that take into account initiation and propagation within a single model framework. One such model was conceived by Mura [44] to deal with initiation, extended by Chan [35], and later coupled with a FCG model in a probabilistic framework by Enright and Chan [45] to account for total initiation and propagation life variability. In this model, both initiation and propagation life are treated on the basis of microstructural parameters, where initiation life is given by Equation (2.5) and propagation life is given by an inverted, integrated form of:

$$\frac{da}{dN} = \frac{2s\xi^{n_2/2}}{[E(2s)^{1/2}]^{n_2}} \left[\Delta K_T^{n_1-n_2} \Delta K^{-n_1} + \Delta K^{-n_2} - [(1-R)K_C]^{-n_2}\right]^{-1} \tag{2.6}$$

where

$$\Delta K_T = \sigma_y \frac{\Delta K_{th}}{\sigma_e} \tag{2.7}$$

$$\Delta K_{th} = \sigma_e [12\pi d]^{1/2} \tag{2.8}$$

$$\xi = \frac{Es}{4\sigma'_y \epsilon'_f d} \tag{2.9}$$

$$d = d_0 \left(\frac{D}{D_0} \right)^{1/3} \tag{2.10}$$

and $\frac{da}{dN}$ is the crack growth rate (m/cycle), s is the dislocation cell size (μm), n_1 is the stage I crack growth exponent, n_2 is the stage II crack growth exponent, ΔK is the stress intensity range ($MPa\sqrt{m}$), ΔK_{th} is the stress intensity fatigue threshold ($MPa\sqrt{m}$), ΔK_T is the stress intensity range at stage I to stage II transition ($MPa\sqrt{m}$), R is the stress ratio, K_C is the fracture toughness ($MPa\sqrt{m}$), σ'_y is the cyclic yield stress (MPa), σ_e is the fatigue limit (MPa), d is the dislocation barrier spacing (μm), E is the Young's modulus, ϵ'_f is the fatigue ductility coefficient, D is the crack-incipient grain size, and d_0 and D_0 are the reference dislocation barrier spacing and grain size, respectively [45].

These total life models have significantly increased the researcher's ability to deal with fatigue behavior using quantitative microstructural information such as grain size and strength information such as the fatigue ductility coefficient. In its present form, the model is unable to deal with initiation mechanism hierarchy in materials where there is not a single incipient failure mode. One such material is the ASTM F562 alloy system in the form of fine wire for medical device applications. For a given material state and set of loading conditions, fracture may occur due to stress concentration at inclusion particles, persistent slip bands, or at process related surface anomalies [4,18]. Understanding of failure mode hierarchy in fine medical wire should significantly improve our ability to predict material performance and variability and reduce the probability of product failure due to fatigue.

2.4 Fatigue Crack Nucleation Sites

Early authors [28, 29, 53] observed that the process of fatigue damage was activated by microscale plasticity at stress levels below the macroscale yield strength. The microscale plasticity involved may be primarily slip, as in most face-centered cubic (fcc) metals such as silver or copper, or a combination of slip and twinning as in some hexagonal close-packed (hcp) metals such as cobalt or multiphase alloy MP35N [54, 55]. Sites from which the cracks nucleate tend to be a function of various microstructural variables including: grain size, inclusion particle size and texture as well as non-microstructural variables including: surface macroscale texture, surface defects such as chevrons, and the environmental corrosion state of the surface [4, 13–18, 35, 43, 44, 49]. These incipient failure states can be divided into two general categories *(i)* those that are materially intrinsic and *(ii)* those that are extrinsic and often related to finish processing.

2.4.1 Intrinsic Nucleation Sites

In this treatise, intrinsic features are defined as those which belong to a material by nature in its service form and are not amenable to dissolution through finishing methods such as thermomechanical processing. Herein, the following defect states are considered materially intrinsic:

- Internal porosity (example in Figure 2.5)
- Microstructural inclusions (generally nonmetallic, example in Figures 2.2, 2.3)
- Grain boundaries
- Grains and associated texture distribution
- Mechanical and annealing twins
- Other microstructural inhomogeneity

- Dislocation based surface structures (slip or Lüders bands, example in Figure 2.3(b))
- Surface tearing associated with underlying inclusion structure

Of these structures, those which have been shown in previous studies [4,18,55–59] to present as probable sites for fatigue failure in MP35N include microstructural inclusions and dislocation based surface structures. An elucidation of lifetime and lifetime scatter with respect to these variables is the intended result.

2.4.2 Extrinsic Nucleation Sites

Extrinsic features are herein defined as those which belong to a material as a result of finish process methods and are subject to modification through thermomechanical processing involved in wire drawing and medical device production. The following defect states are considered materially extrinsic:

- Surface tearing from causes other than microstructural inclusions (example in Figure 2.6(a))
- Tool related surface damage (example in Figure 2.6(b))
- Thermomechanical related residual stresses at surface inhomogeneities
- General surface roughness (e.g. lines related to drawing die wear)

Numerous studies [5, 15, 43, 46, 60, 61] have demonstrated the importance of understanding the impact of natural, extrinsic damage states that evolve during normal processing conditions and their effect on structural resistance to fatigue damage. The highly polished state and low surface roughness (RMS$<$0.10 μm [4]) of the material under study here have been shown to result in a low occurrence rate of failures related to extrinsic defects. Importantly, however, the impact of such structure must be understood because of its negative impact on lifetime.

2.5 Size Effects

Connolley *et al.* [19] observed that there are significant gaps in our understanding as we progress from macroscale specimens to microscale devices. In their publication, they stated that:

> Conventional macroscopic test data can be used, but these are obtained using specimens whose size is much larger than the devices themselves. There is a risk that performance predictions will be inaccurate, due to the existence of size effects.

Most fatigue behavior data for materials used in the medical device industry are derived from test standards developed for macroscale test coupons. ASTM E399, for example, gives protocol for evaluating the plane strain fracture toughness of metallic materials. The specification calls for geometries not approaching the plastic zone size given by:

$$2.5\left(\frac{K_Q}{\sigma_{YS}}\right)^2 \tag{2.11}$$

where K_Q is the provisional stress intensity (MPa$\sqrt{m}$) and σ_{YS} is the 0.2 % offset yield strength in tension according to ASTM E8. Inserting assumed values of $K_Q = 100MPa\sqrt{m}$ (nominal value from ref [57]) and $\sigma_{YS} = 250MPa$ into Equation (2.11) gives a critical zone size which must be smaller than sample dimensions of 8.4 mm. From this, it is clear that we expect plane-stress behavior throughout the FCG process in the 0.177 mm fine wire samples studied herein. Further, we cannot rely upon mechanical and fatigue data gathered from significantly larger samples and must develop new data sets applicable to the current application.

2.5.1 Small Crack Behavior

Pearson [47] observed that small cracks in aluminum alloys grew at lower stress intensities and at faster rates than corresponding large cracks. In the decades following Pearson's discovery, further characterization of this phenomenon has been the subject of many research efforts [43, 48–50, 52]. Small cracks in ductile materials are generally defined as those measuring 10 μm to 1 mm in length [50]. Small cracks, loaded below the ΔK threshold of large crack theory, proceed at a relatively high rate until other effects are fully developed. A depiction of this phenomenon is qualitatively represented in Figure 2.8. Plasticity effects, metallurgical effects, and crack closure have all been used to explain the small crack fatigue regime and are still being debated today [50].

Materials, such as 35N LT, with inclusions and grain sizes much smaller than 10 μm still fail in fatigue at structural inhomogeneities, including 1-3 μm particles such as the failure shown in Figure 2.7. The associated stress intensity ($<$3 $MPa\sqrt{m}$) in this case was below the FCG threshold expected for this material given its reported high level of toughness [57]. At cracks that are as small or smaller than the primary microstructural features (grain size, inclusion size), growth does not proceed as it does when distributed over many grains. This results in breakdown of the averaging rule, known as metallurgical similitude [50]. In this case, the crack front is more subject to changes from intersecting twin boundaries, alternate phase boundaries, small particles, grain boundaries and other stress-altering features. Further microscopic examination of small crack phenomenon in medical wire is needed to understand these effects.

2.5.2 Small Specimen

The processing of medical wire involves microstructural refinement through significant cold reduction and progressively shorter dwell recrystallization anneals that yield increasingly fine grain distributions. As wire diameters tend towards finer sizes, the average number of grains through a transverse section is reduced. Using nominal production data, the average wire diameter to grain size ratio has been plotted for the MP35N/35N LT process stream, and is shown in Figure 2.9. From this plot, it is evident that below a wire diameter of 0.30 mm, less than 10 grains, on average, form the wire thickness and less than 5 grains below 0.10 mm. Authors [19, 50] have made qualitative statements regarding the point at which property relations related to microstructural similitude may begin to break down, however, no quantitative relation was found for fine wire specimens.

2.5.3 Plane Stress vs. Plane Strain

It is well known that under plane stress conditions, a given load will produce a larger process zone than when plane strain conditions dominate [62]. Most fatigue cracks in metallic wire specimens begin at surface features [4,5,18], thus, it is expected that plane stress conditions are dominant at crack nucleation. It is only during crack propagation that surrounding material may constrain the propagating front. The fatigue crack propagation life model set forth by Enright and Chan [45], given by Equation (2.6), includes the fracture toughness, K_C. In this model, however; the fracture toughness is set to a large deterministic value and is not studied for its effect on life variability. From the results of Equation (2.11) from ASTM E399, clearly it is impossible to obtain plane strain fracture toughness values for fine wire under 1 mm in diameter. Studies on fracture toughness in fine diameter wire were not found at the time of this research.

2.6 Residual Stresses

The importance of residual stresses in fatigue crack initiation and propagation is evidenced by its discussion in many recent publications [18, 19, 37, 46, 63–68]. Researchers are generally careful to eliminate residual stresses induced during sample preparation through careful machining, progressively lighter grinding, and often through the use of chemical or electrochemical final polishing methods [13, 15–17, 57]. Medical CRM lead wires are not constructed with laboratory-grade specimens, instead, cold drawn wires are further upset through coil and cable production before being polymer coated and assembled into a final product. Determination of resultant residual stress profiles using X-ray diffractometry or other suitable methods is necessary to adequately model these effects [18]. An example of a residual stress profile for cold-drawn MP35N and 35N LT wire is shown in Figure 2.10.

The stress ratio, R, in a fatigue test is defined simply as:

$$R = \frac{S_{min}}{S_{max}} \tag{2.12}$$

where S_{min} is the minimum stress and S_{max} is the maximum remote stress near the crack tip. In a rotary beam fatigue test, it is typically assumed that $R = -1$. In a residual stress free, annealed wire, $R = -1$ is an appropriate and likely accurate statement. From Figure 5.26, it is clear this is no longer a valid assumption at the wire surface where fatigue cracks begin. In this case the stress ratio becomes:

$$R_{mod} = \frac{S_{min} + S_{R_0}}{S_{max} + S_{R_0}} \tag{2.13}$$

where R_{mod} is the modified stress ratio, and S_{R_0} is the maximum residual tensile surface stress. Based on results from other studies [15, 43, 46, 50], the expected result of an increased stress ratio is greater crack operation for a given applied external stress and a reduced effective crack growth threshold stress intensity range.

2.7 Tables and Figures

Table 2.1 Typical chemistry similarity in ASTM F562 alloys systems, note reduced titanium content in 35N LT [18].

Element	MP35N	35N LT
Carbon	0.010	0.010
Manganese	0.020	0.060
Silicon	0.040	0.030
Phosphorus	0.002	0.002
Sulfur	0.001	0.001
Chromium	20.45	20.58
Nickel	34.79	34.82
Molybdenum	9.52	9.51
Iron	0.44	0.52
Titanium	*0.70*	*0.01*
Boron	0.009	0.010
Cobalt	Balance	Balance

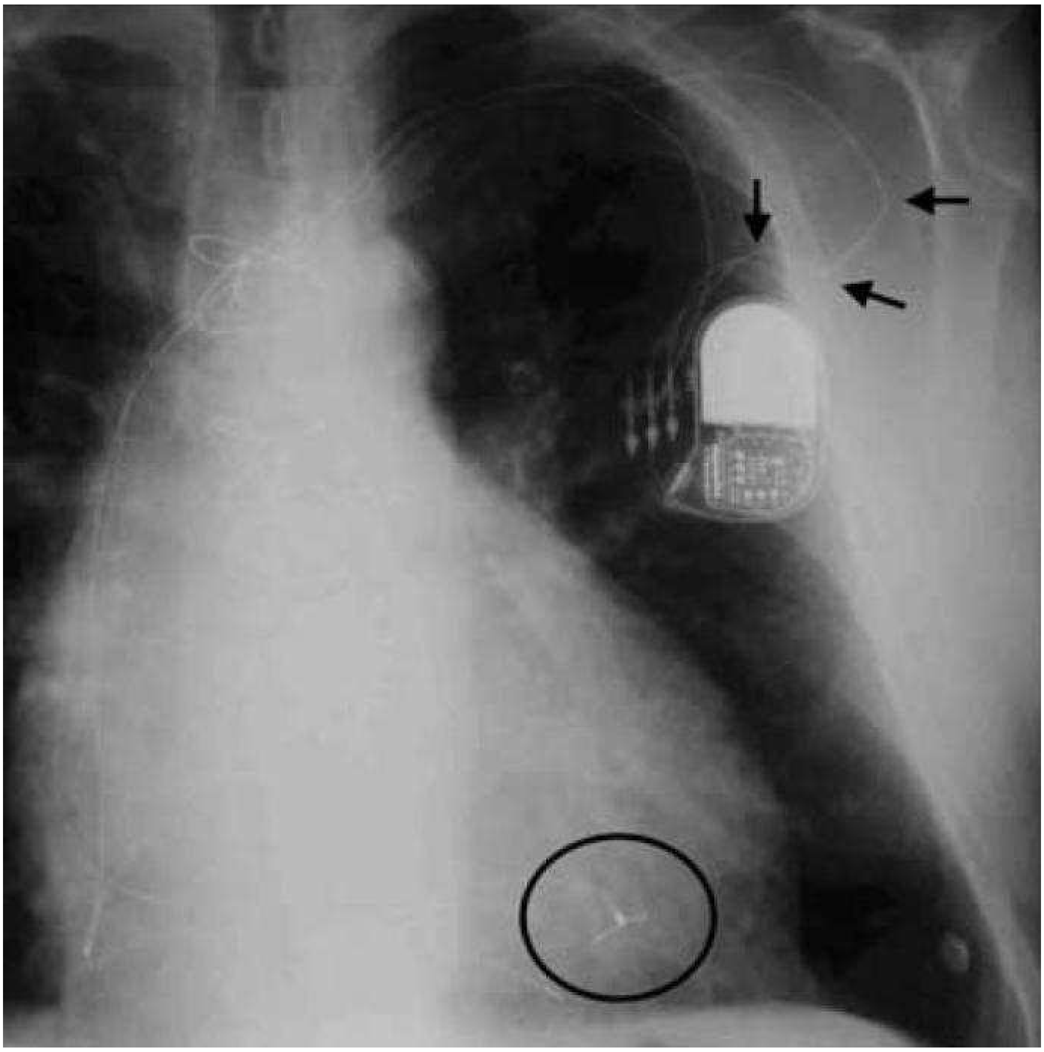

Figure 2.1. Chest X-ray of a lead wire possessing multiple fracture sites indicated by arrows near kink points. Adapted from [20], with permission.

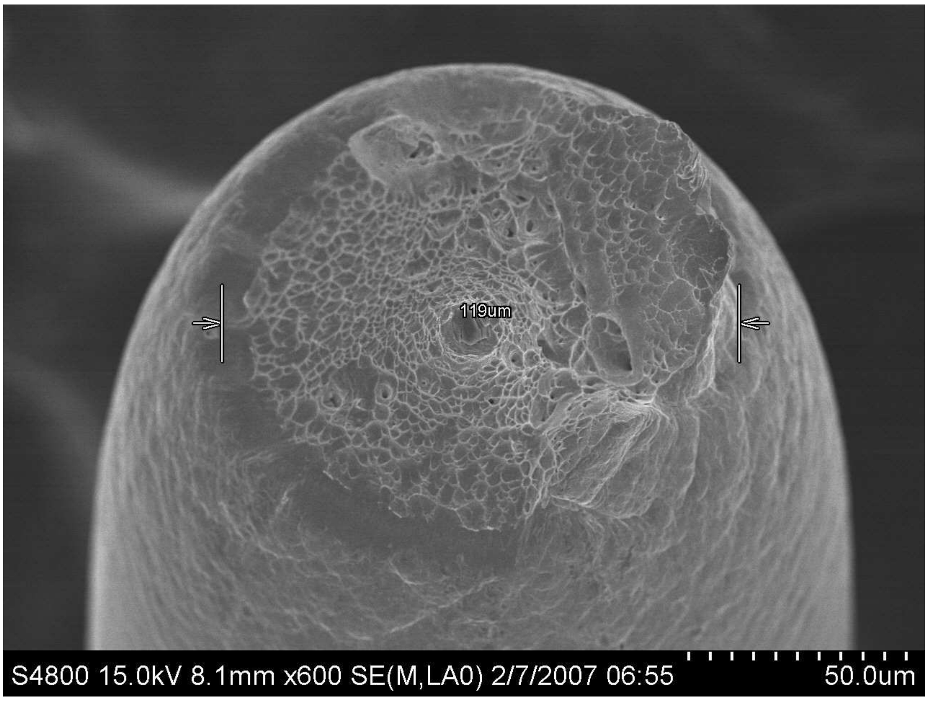

(a) Overall section after monotonic tensile overload.

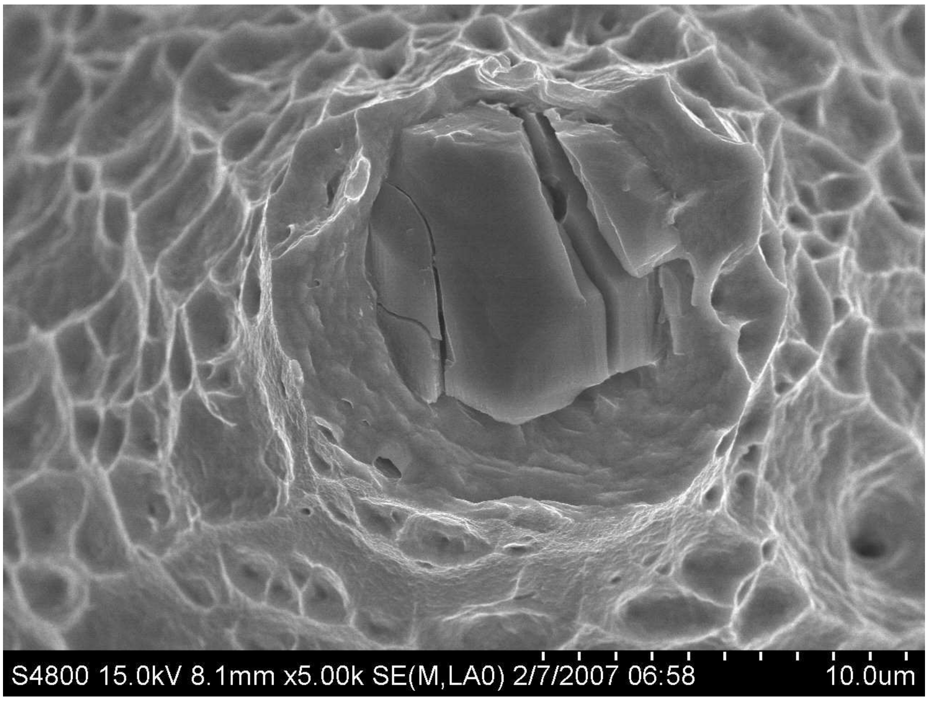

(b) Cracked 8.5 μm TiN inclusion.

Figure 2.2. Large TiN particle at interior of 177 μm MP35N wire.

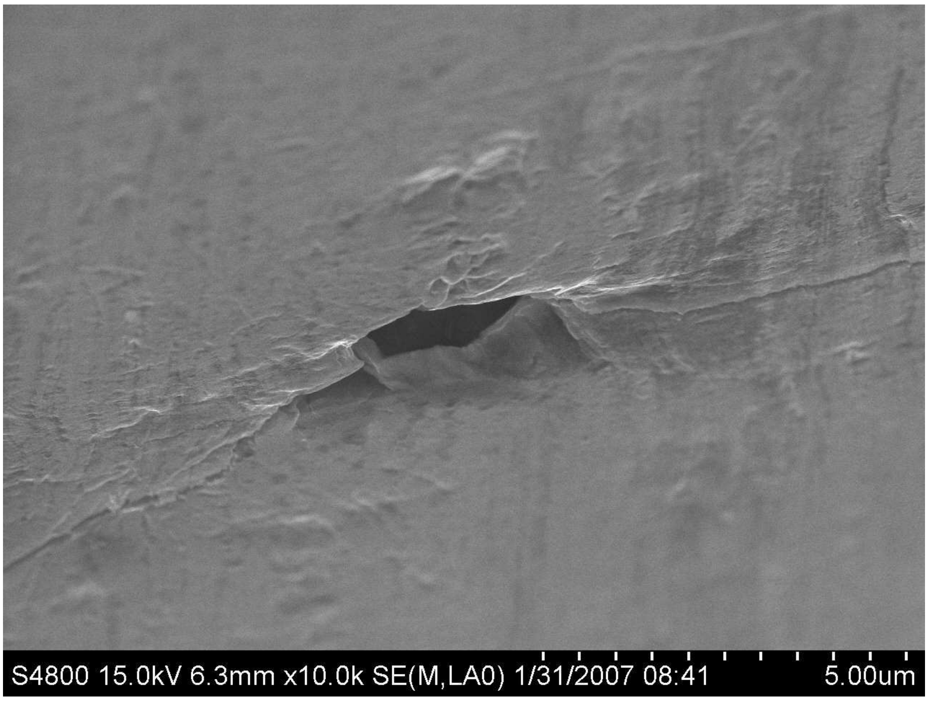

(a) Incipient TiN particle feature in 1930 MPa MP35N after 64,100 cycles at $S_a = 930MPa$, $R = -1$.

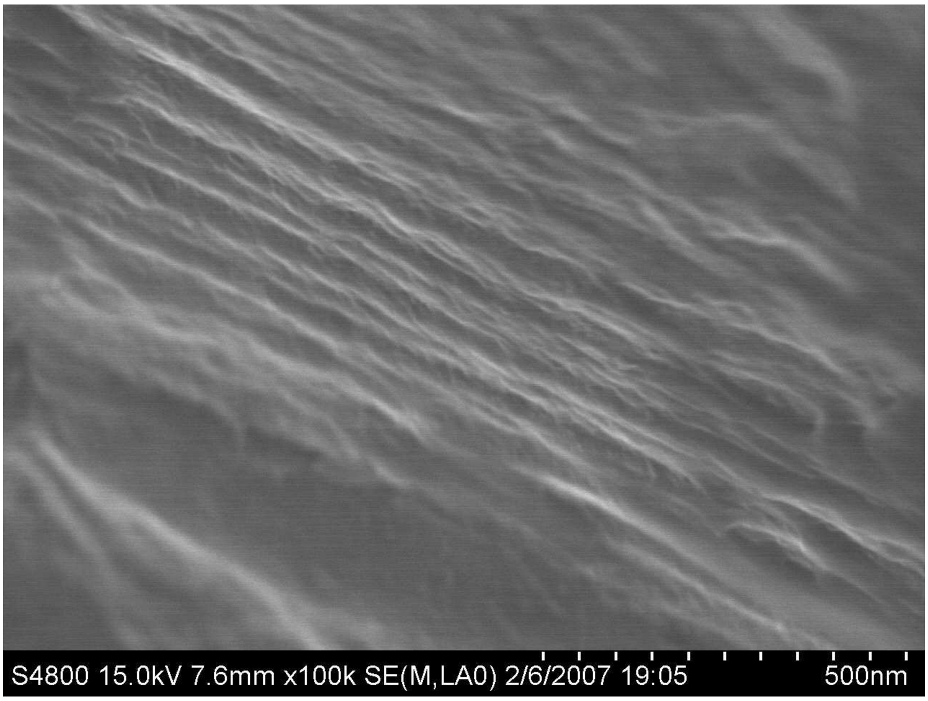

(b) Polyslip surface features and 200 nm PSB protrusion near crack front in 1930 MPa MP35N after 205,000 cycles at $S_a = 690$ MPa, $R = -1$.

Figure 2.3. Intrinsic structural defects in MP35N.

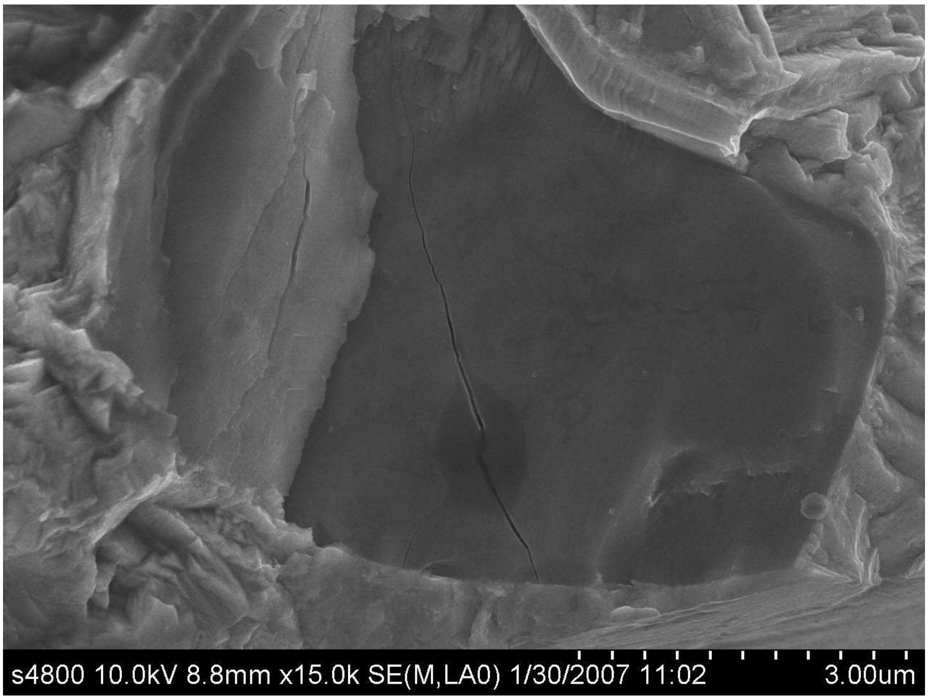

(a) Near-initiation, cracked TiN particle, specimen failed at 71,900 cycles.

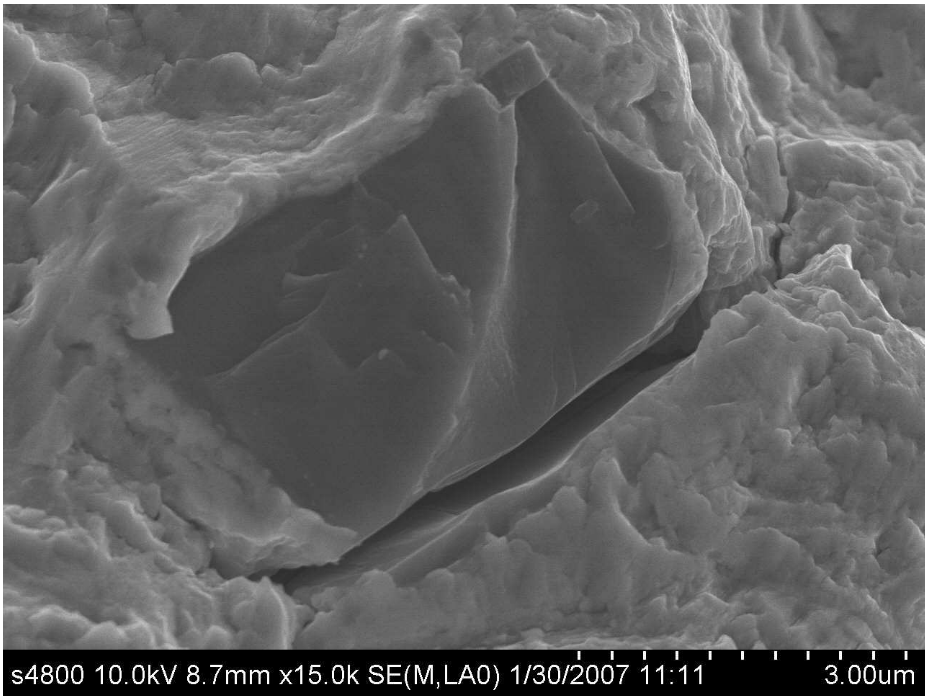

(b) Debonded central TiN particle, specimen failed at 72,100 cycles.

Figure 2.4. TiN particles in 177 μm, 1930 MPa MP35N tested at $S_a = 930$ MPa, $R = -1$.

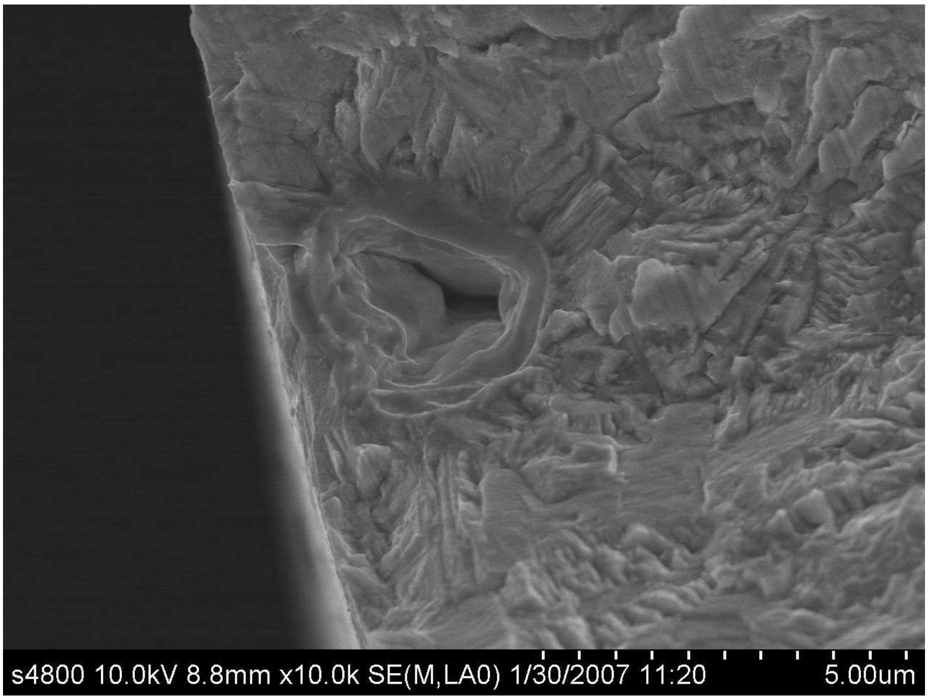

(a) Vacant particle near-initiation site, specimen failed at 72,100 cycles.

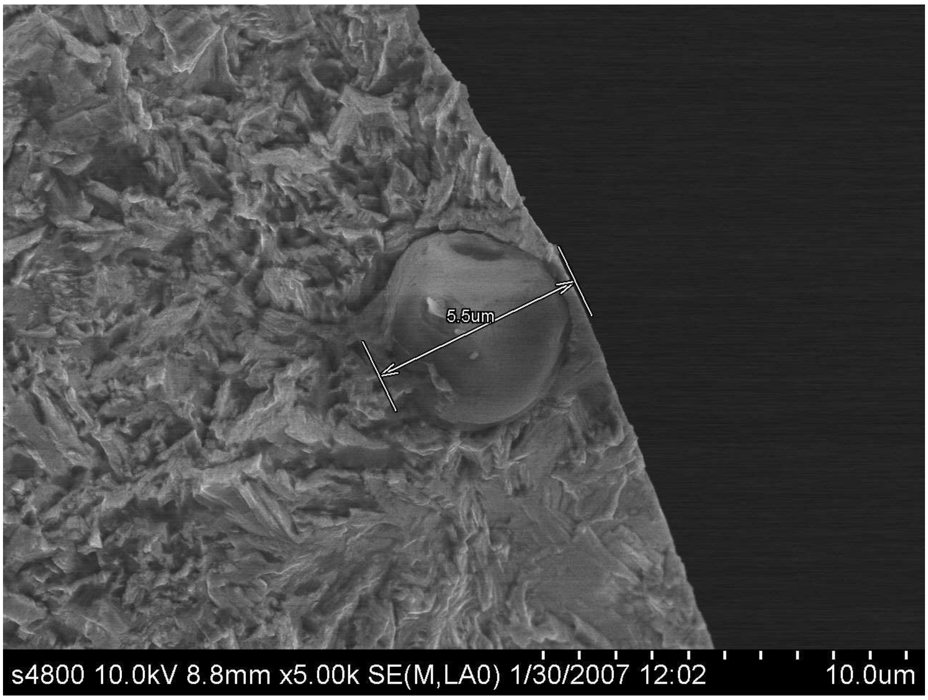

(b) Near-initiation Al_2O_3 particle, specimen failed at 72,500 cycles.

Figure 2.5. Other intrinsic structural defects in 177 μm, 1930 MPa MP35N tested at $S_a = 930$ MPa, $R = -1$.

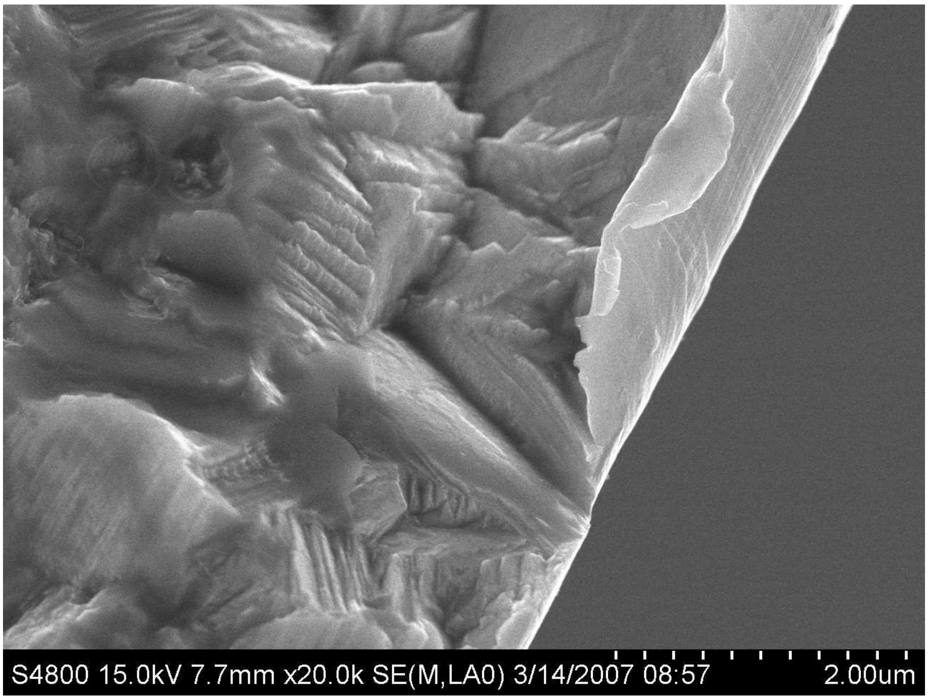

(a) Chevron crack-initiating feature in 177 μm, 1930 MPa 35N LT tested at $S_a = 827$ MPa, $R = -1$, specimen failed in $9.2x10^5$ cycles.

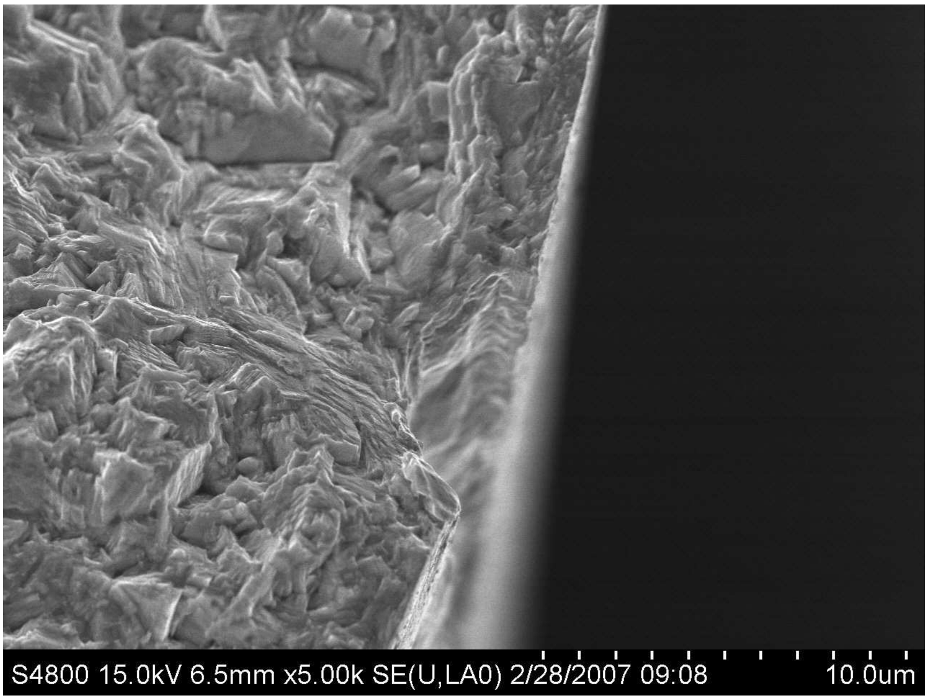

(b) Tool mark crack-initiating feature.

Figure 2.6. Extrinsic structural defects in 35N LT.

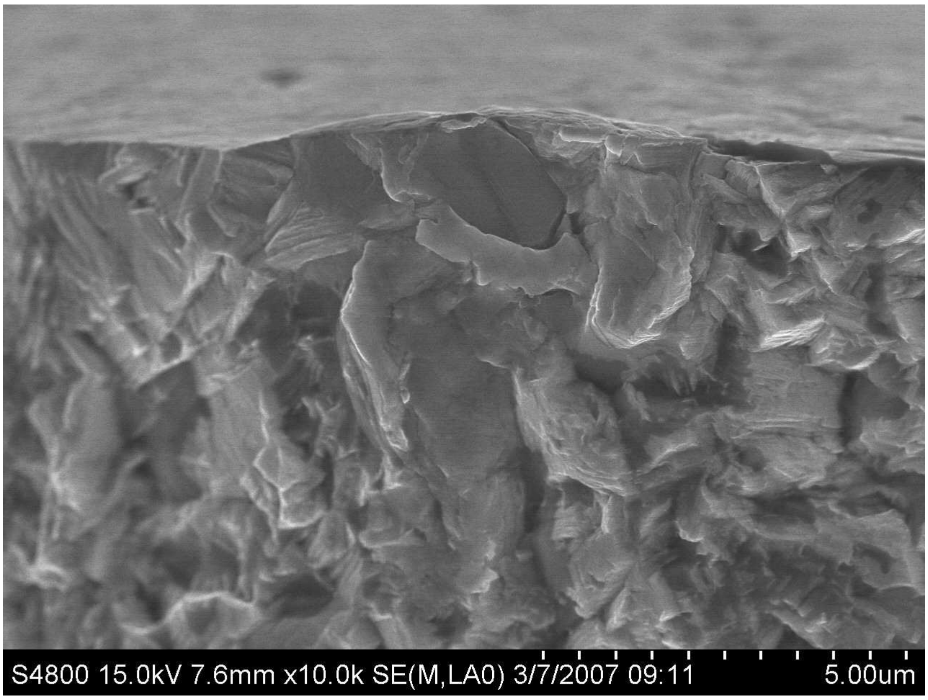

(a) 2 μm Al_2O_3 crack-initiating particle. Stress intensity range at initiation, 3.8 $MPa\sqrt{m}$, 1930 MPa 35N LT tested at $S_a = 827$ MPa, $R = -1$, specimen failed in $3.51x10^5$ cycles.

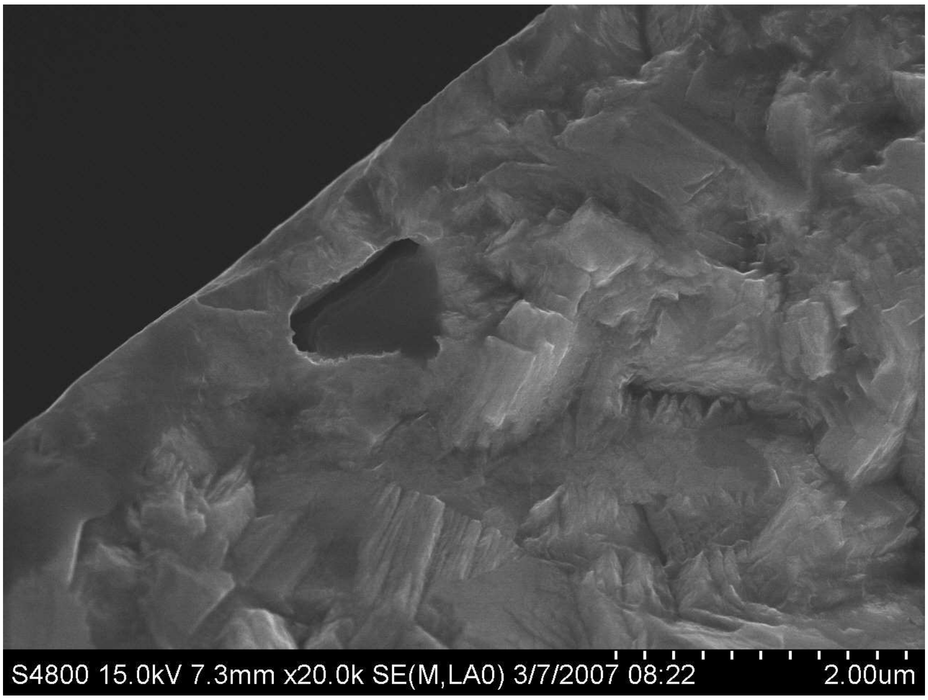

(b) 1 $\mu m Al_2O_3$ crack-initiating particle. Stress intensity range at initiation, 2.9 $MPa\sqrt{m}$, 1930 MPa 35N LT tested at $S_a = 827$ MPa, $R = -1$, specimen failed in $1.75x10^7$ cycles.

Figure 2.7. Low stress intensity range crack-initiating features in 35N LT.

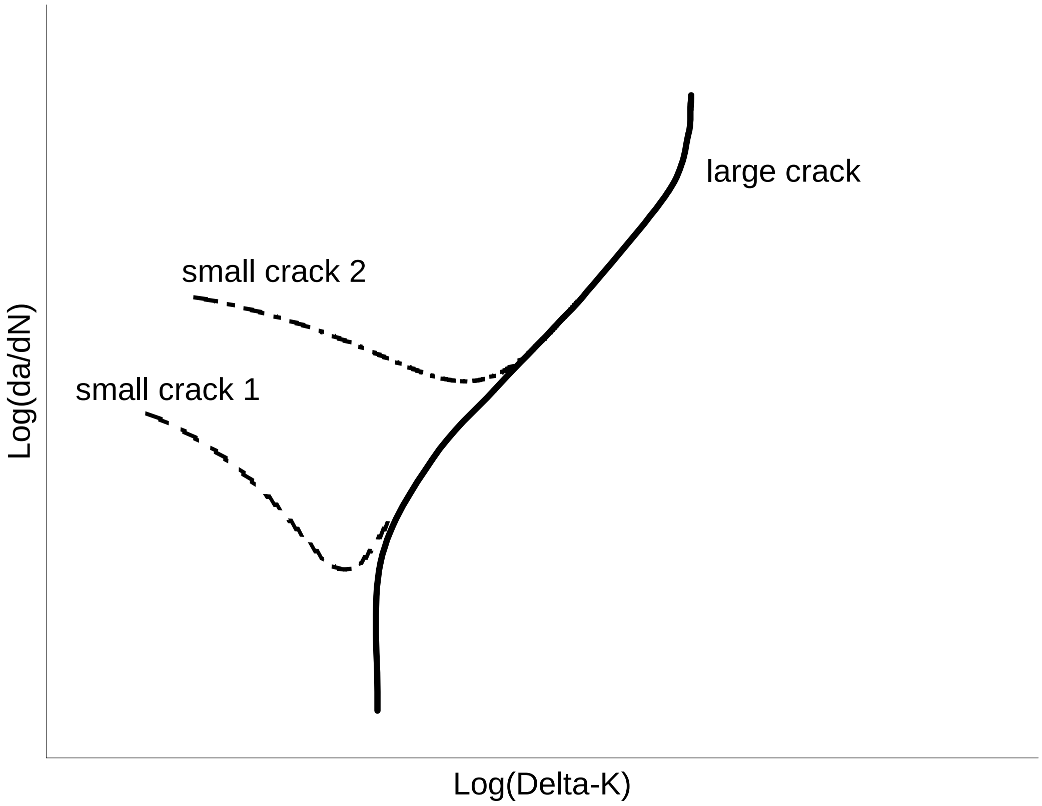

Figure 2.8. Schematic diagram of $\frac{da}{dN}$ vs. ΔK. Adapted from [50].

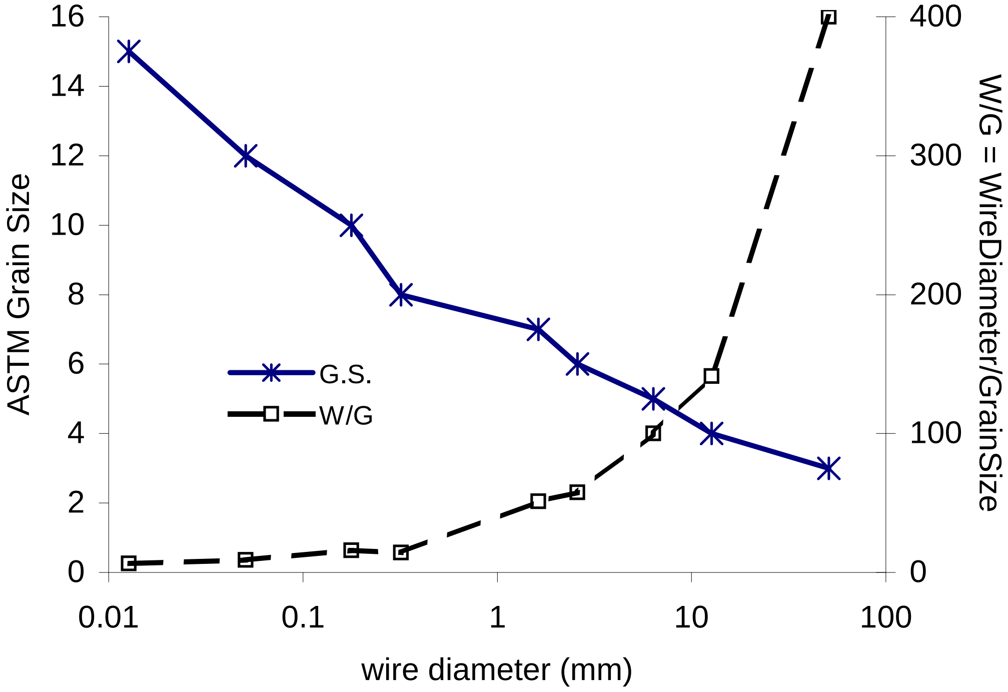

Figure 2.9. Typical MP35N Grain size as a function of wire diameter and wire diameter to average grain size ratio.

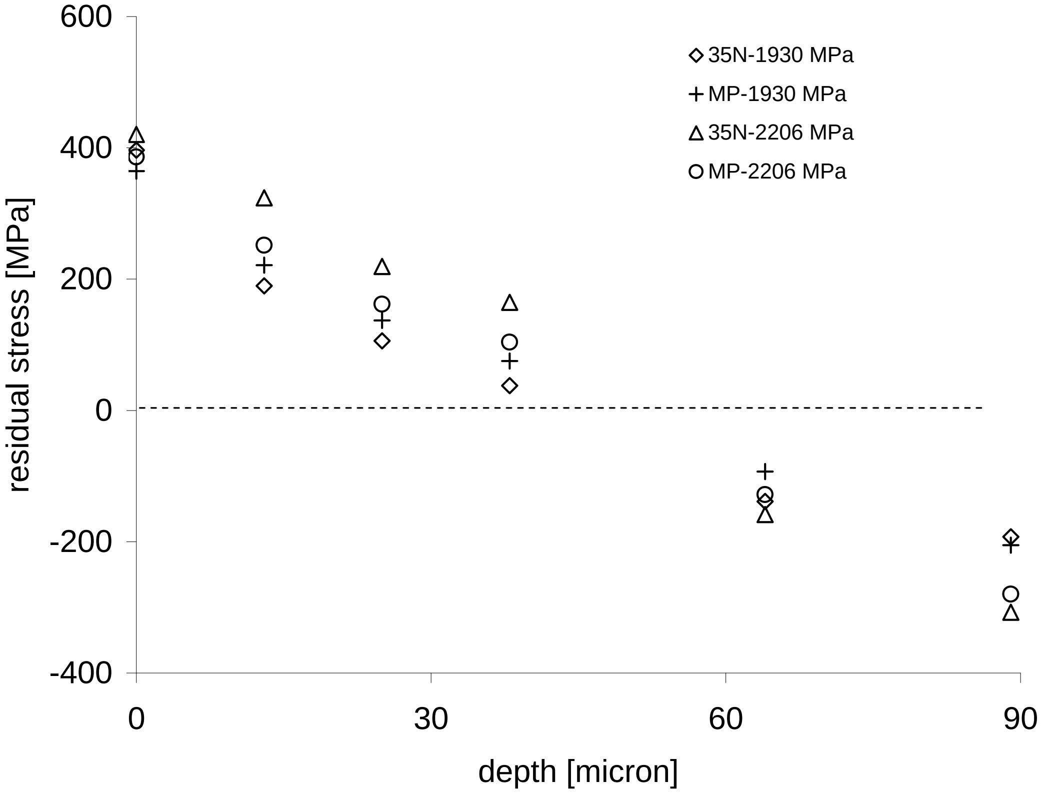

Figure 2.10. Example of a residual stress profile in cold-drawn 177 μm MP35N and 35N LT wire with typical surface residual tensile stress. Adapted from [18].

3. MODEL DESCRIPTION

3.1 Overview

The model for fatigue analysis of fine medical wire invokes stochastic as well as deterministic input from a variety of material related sources. The first set of data to be composed was the statistical distribution of the initial defect space. This included surface grain size, inclusion size, and other inhomogeneous defect states. In the present model, deterministic treatment was applied to parameters including the shear modulus, Poisson's ratio, fatigue limit and others according to Equations (2.4) and (2.5) for initiation at inclusions and persistent slip band features respectively.

An important feature of the model was its selection criteria for creating a crack-nucleating defect distribution from the overall defect space. In this algorithm, N_d defects were selected at random using appropriate statistical distribution parameters with Monte Carlo methods. A crack-nucleating intensity factor (CNIF) was assigned to each defect site to represent a given quantity of possible initiation states within a region of critical load stress. For each group of N_d defects, the state possessing the maximum CNIF was chosen as the crack-incipient feature and used in life calculation. Initial Monte Carlo simulated data tables were generated in Microsoft EXCEL®[1] and read into Mathematica®[2] 4.0 computational software for CNIF evaluation, maximum CNIF selection, life computation, and finally exported back to EXCEL for CDF generation and graphical display. Also proposed is an initiation hierarchy function (IHF) for determination of dominant fatigue crack nucleating features in fine medical wire.

---

[1] EXCEL® is a registered trademark of Microsoft Corporation, Redmond, WA, USA.

[2] Mathematica® is a registered trademark of Wolfram Research, Champaign, IL, USA.

3.2 Assumptions

The three key assumptions made throughout this work were:

- Fatigue cracks nucleate at sites of dislocation pileup due to slip obstacles such as grain boundaries, inclusions, or other microstructural features, thus validating the use of Tanaka and Mura's [44] dislocation dipole initiation life model.
- Constituent particle survey analysis conducted at larger diameters provides valid statistical input to the life model at much finer diameters.
- In the life range beyond 10^6 cycles, in fine medical wire, fatigue crack propagation life is negligible compared to fatigue crack initiation life.

Past studies [4,18,69] have shown that wrought MP35N tends to fail at melt-intrinsic constituent particles. It is known that slip activation occurs (1) in preferentially oriented crystals (in a polycrystalline metal) [54] and (2) in regions of stress concentration, such as at sharp fatigue crack tips or at relatively hard phases in the material. In the past century, many studies [26] have shown that the primary mechanism of material degradation in cyclic loading is that associated with irreversible slip movement of dislocations. The assumption of a dislocation pileup mechanism of cumulative fatigue initiation damage in the MP35N or 35N LT alloy system was considered a logical choice.

Schaffer [18] presented evidence that the TiN and Al_2O_3 inclusion particles in the ASTM F562 alloy system do not migrate radially or change their size distribution significantly during cold drawing to fine diameter sizes. Validity of this assumption implies that wire producers can complete metallographic surveys of larger raw stock to predict fatigue performance after significant processing to smaller sizes. Ultimately, these tools could be used to screen incoming raw wire stock and create new standards of microcleanliness based on necessary design life in finished medical devices. The potential processing cost savings are significant. Alternatively, stock could be diverted to less critical or larger components immediately upon receipt of the defect statistics.

In the early stages of this research, cracks were found to grow at lower than expected ranges of stress intensity (i.e. from smaller inclusions at lower stress levels). This fact, in combination with striation measurements which predicted initiation lives on the order of tens of thousands of cycles across a 177 μm filament cemented the final assumption of negligible FCG life in high cycle, fine wire applications. At the nanoscale, this assumption does not imply that some FCG does not occur prior to initiation. The life of a crack when it is less than a micron in length is not presently well understood. Crack growth and arrest on the order of the unit cell dimensions for the fcc matrix, may contribute significantly to total fatigue life. The stated assumption here implies that these phenomenon are bundled into what we consider in this treatise as initiation life. In the future, studies to better understand near-initiation FCG should be conducted.

3.3 Probabilistic Variables

The prediction of variability in fatigue life was one of the primary goals of this research. Based on empirical evidence, two material constraints were known to give rise to life variability; these comprised constituent particle size and the spatial relationship of the particle relative to the surface or depth. Dependent on the expected nucleation mechanism, grain size was also treated as a variable input in some determination schemes.

3.3.1 Constituent Particle Size

The inclusion particle sizes were chosen from a lognormal distribution that was fit to experimental data. Inclusion survey analysis was conducted using 2.5 mm diameter stock and then confirmed for consistency at the 177 μm wire diameter. Determination of the inclusion content in relatively large materials, such as the 2.5 mm wire examined in this study, is a relatively simple task. In this case, 160 images were collected at 1000X magnification from random MP35N wire sections using backscattered electron imaging (BEI) in a SEM for a total examined area of 1.73 mm^2 of transverse wire area. This was repeated for three material lots. A total of 4103 inclusions were measured in this analysis. The image data were then analyzed using digital processing to yield information for inclusion length, breadth, area, aspect ratio, and radial position. Similar analysis of three lots of 2.5 mm 35N LT yielded a total of 722 particle sites. The resultant geometric parameters were empirically fit to CDFs using a lognormal distribution as described by:

$$f(x; \mu, \sigma) = \frac{1}{x\sigma\sqrt{2\pi}} exp \left[\frac{-(\ln x - \mu)^2}{2\sigma^2} \right] \tag{3.1}$$

$$E(x) = e^{\mu + \sigma^2/2} \tag{3.2}$$

where μ and σ are the scale and shape parameters or the geometric mean and standard deviation respectively of the variable's logarithm. The results of statistical analysis of inclusion size data are shown in Figures 3.1, 3.3 and 3.3(b) [18].

3.3.2 Constituent Particle Depth

As represented in Figure 3.3(a), the distribution of the inclusions with respect to volume was found to be uniform in both sizes and material systems examined. The finding of volumetric uniformity was somewhat surprising considering the amount of cold deformation and increase in surface area imparted to the wire during the drawing operation. Such operations have been theorized to yield a relative drift in the radial position of hard inclusion particles. In the case of a uniform volumetric dispersion of inclusion particles, the probability of finding an inclusion within some radial band should increase proportionate to area, or R^2, where R represents a given radial position in the wire transverse section. It follows from these assumptions that the CDF of radial position for both the 177 μm and 2.5 mm wire should conform to:

$$F(R; R_W) = \left(\frac{R}{R_W}\right)^2 \tag{3.3}$$

where R_W represents the wire radius. The CDF shown in Figure 3.3(b) confirms the finding that the constituent particles adhere to volumetric uniformity associated with the homogenizing VIM / VAR melt practice which has survived processing all the way to fine diameter wire. The finding of volumetric uniformity is important; this fact, in combination with the lack of significant particle size change during processing, allowed the use of intrinsic constituent particle data collected at 2.5 mm to predict fatigue performance of finished 177 μm diameter wire.

The depth from the wire surface was chosen using Monte Carlo methods by pulling directly from the square root of a uniform, $U[0, 1]$, distribution and was randomly assigned to each inclusion to locate and calculate the stress acting on potential crack nucleating sites.

3.3.3 Grain Size

Grain boundaries exist due to crystal misorientations that occur in most crystalline solids [70]. Many authors [35,36,40,70,71] have demonstrated the formation of persistent slip bands (psb) at surface grains possessing a preferred orientation and/or size relative to the applied fatigue loading axis. While the detailed mechanisms of the grain-size-effect are still debated [72], it is generally accepted that slip occurs more readily in larger grains. Further, it has been shown that the stress field acting at the tip of a psb, behaves similar to that at a crack tip [40,70,71]. A schematic of incipient plastic behavior in a single, preferentially oriented grain is depicted in Figure 3.4.

The grain size (GS) of each material was measured at the surface and at internal transverse and longitudinal orientations. During fatigue crack propagation, the crack front moves from an initiating surface feature through internal microstructural features. If life were dependent primarily upon FCG, then it would have been useful to consider the internal grain size distribution. In this study, however, initiation at surface features was the dominant factor influencing life. Therefore, the grain size information used in modeling was taken from surface data. Most materials analyzed were found to have a finer surface grain structure than at the specimen interior. An example of fine surface texture in 177 μm 35N LT wire is shown in Figure 3.5. Differentiation of the surface grain size from interior grain size data is represented by the dotplot for 35N LT in Figure 3.6.

3.3.4 Crack Nucleation Intensity Factor (CNIF)

For materials expected to fail at intrinsic microstructural features other than constituent particles, a crack nucleation intensity factor (CNIF) is proposed which is scaled as a stress intensity load factor for randomly selected surface grains using the relation:

$$CNIF_{grain} = S\sqrt{(}d) \tag{3.4}$$

where S is the local applied stress (MPa) and d is the local grain size (μm). In this case, since psb length was expected to scale with grain size, the grain size was used to calculate local stress intensity. Additionally, because of the small grain size in this study, there were always many grains within the critically stressed region. The orientation of each grain relative to the loading axis partially determines its ability to deform by plastic slip. The important factor in determining the response of a single crystal to an applied stress is the local Schmid factor [54]. In the 10 mm critically stressed zone, at a GS of 3 μm, it is estimated there were greater than 0.5x10^6 surface grains. Practically, this means that the model may adequately account for probability of initiation by considering grain size without regard to grain orientation. This assumption would not be expected to hold for smaller diameter wire where there are fewer grains in a critical region. Further, the current model could likely be improved by inclusion of detailed texture data from a combination of electron backscattered diffraction (EBSD) and x-ray diffraction (XRD) analysis techniques.

Based on LEFM theory, and in accordance with studies on near threshold fatigue behavior, one would expect that a good indicator of the probability of nucleation from an inclusion would be the local stress intensity factor (SIF) for that inclusion. This simplified view on the probability of nucleation ignores factors such as grain orientation, dislocation barriers and other factors influencing dislocation movement. An alternative simple relationship for CNIF at inclusions is proposed here as:

$$CNIF_{inclusion} = S\left(\frac{\xi}{D_i}\right) \tag{3.5}$$

where ξ is the inclusion size (μm) and D_i is the inclusion depth normal to the nearest wire surface (μms). In modeling these values, an inclusion depth that approaches zero (e.g. an inclusion very near to the surface), will result in a very high CNIF and will likely be selected as the crack nucleating (CN) feature within a given set of defects. A potential flaw in using only the SIF to predict the CN feature would be the weak effect of particle depth on selection, which is later shown to be important in determining the CN distribution.

3.4 Deterministic Parameters

Dependent upon the dominant initiation mechanism, a number of parameters were treated as deterministic input to the life prediction model. These parameters included:

- Material Elastic Properties
- Grain Size
- Initiating Crack Size
- Taylor Factor

- Fatigue Limit
- Slipband Width
- Fatigue Life Exponent
- Universal Constant

and are presented with example values for 1930 MPa, MP35N used here in Table 3.1. The roles of variable and deterministic inputs to the model could easily be swapped to yield statistical distributions for any of the parameters considered in this study. In [45], for example, an incipient crack length probability density function (PDF) is presented for varying levels of initiation life.

3.4.1 Material Elastic Properties

The shear modulus (μ) and Poisson's ratio (ν) of the base material (MP35N or 35N LT) as well as the shear modulus (μ') of the inclusion particles are used in the inclusion based life model given by Equation (2.5). Variability in these parameters was considered negligible in this study.

3.4.2 Grain Size, (d)

In the life model for materials in which the grain size was equal to or larger than the overall inclusion distribution, particularly in the (ductile) annealed materials, the grain size was treated as a life-variability-driving stochastic variable as already described. However, in the strain-hardened materials, or those possessing inclusions that were larger than the average grain size, the GS was held constant and taken as the median of the distribution.

3.4.3 Initiating Crack Size, (c)

Enright and Chan [45] considered the initiating crack size as the dimension at which the fatigue damage process exited the initiation stage and entered the FCG regime. In this study, the initiating life in fine wire was found to comprise greater than 95% of the total life for anything beyond one million cycles. Here, the initiating crack size is treated as a deterministic input held at a value of 5 μm based on estimated initiation region sizes in this alloy from micrographic interpretation.

3.4.4 Taylor Factor, (M)

The Taylor factor takes into account crystalline constraint in polycrystalline materials [54]. This arises largely due to property anisotropy with respect to crystal orientation. The factor can be loosely defined as the ratio of the yield stress of a polycrystal to the critical resolved shear stress required to operate slip on a single, preferentially oriented system within an unconstrained single crystal. For most metallic, face-centered-cubic (FCC), polycrystalline materials, the Taylor factor tends to be around 3 [54]. During cold deformation following a recrystallizing anneal, researchers have measured an increase in the amount of crystalline constraint due to developing textures in the initially random structure. The choice to treat the Taylor factor herein as a deterministic parameter is a direct result of the absence of texture statistics for these fine wire materials. In this model, equiaxed, annealed structure is assigned a value of 2.5, while strain hardened samples are assigned a Taylor factor of 3.

3.4.5 Fatigue Limit, (σ_e)

The fatigue limit was derived from experimentally determined stress life data for each material configuration considered. The limit was defined as the stress yielding a 5% probability of failure at a lifetime of 100 million cycles.

3.4.6 Fatigue Life Exponent, (α)

The fatigue life exponent was calculated from experimental data for each material configuration considered. Median stress life data were plotted and fit to an exponential fitting function.

3.5 Initiation Mechanism Hierarchy

Several authors [13,17,50,71–74] have examined fatigue crack initiation and small crack growth phenomenon at both constituent particles and in the vicinity of grain boundaries. In these studies, the fatigue initiation mechanism was considered constant for a given material and loading scheme. In the 35N LT alloy system, it is possible to process the material such that the dominant microstructural and inclusion size scales are very similar. In this case, fatigue cracks were observed to start at inclusions in some samples and at other intrinsic microstructural features in others, a phenomenon denoted: mixed-mode initiation. This initiation mechanism hierarchy is important in the development of a holistic model that takes into account the various fatigue damage evolution processes that may take place in fine medical wire systems.

3.5.1 Constituent Particles

The two material systems MP35N and 35N LT are primarily differentiated not by chemical or macroscale mechanical attributes, but rather by the relative size distributions of their melt-intrinsic constituent particles. An upward shift in the particle size distribution, or in the numbers of inclusions present, would be expected to result in a reduced fatigue lifetime and an increase in the number initiation sites directly related to stress concentration at such inclusions.

3.5.2 Persistent Slip Band Surface Protrusions

Fewer inclusion-initiated fatigue crack sites would be expected in materials, such as 35N LT, possessing inclusions that are generally smaller than other microstructural features such as grain size and psb extrusion or intrusion lengths.

3.5.3 Extrinsic Defects

Extrinsic defects, and notably sharp notches associated with weld corners or surface gouges, were the primary cause of failure in early locomotive axles [26]. In fine medical wire, the material is carefully prepared and deep drawn successively through very smooth natural diamond dies specifically in order to promote a smooth and extrinsic-defect-free surface. Of more than 400 fatigue fractures examined under SEM in this study, only two were attributed to these types of defects. At a prevalence rate of less than 0.5%, these types of fractures were hereafter ignored in modeling efforts.

3.5.4 Preferentially Sized Crystals

With a few exceptions [75], most studies show an increase in fatigue life as the grain size is reduced. While there are numerous explanations for this phenomenon, it is generally agreed that, in the absence of other defect states, cracks will form at or near the largest crystal within the critically stressed zone.

3.5.5 Initiation Hierarchy Function

The presence of multiple initiation mechanisms for a single set of load and material parameters presents the need for an initiation sorting algorithm prior to model input for life determination. The use of non-dimensional parameters in such a relation should make it universal and scalable for other situations. There are several parameters that, based on present theory and qualitative evidence, could be justified for use in such an algorithm. The empirical model proposed here is of the form:

$$\chi = 1 - \eta(\ln \epsilon_f) \left(\frac{d}{\xi}\right)^{1/2} \left(\frac{\mu}{\mu'}\right) \left(\frac{\sigma}{\sigma_e}\right) \tag{3.6}$$

where η is a curve fit value, χ is the initiation hierarchy function valued from 0 to 1 and represents the fraction of the number of non-inclusion initiation sites to inclusion-based initiation sites, ϵ_f is the monotonic elongation to rupture, d is the grain size (μm), ξ is the inclusion size (μm), μ is the shear modulus (GPa), μ' is the shear modulus of the inclusions, σ is the loading stress (MPa), and σ_e is the fatigue limit (MPa).

The first factor in Equation (3.6) is related to material ductility. The interpretation is that we expect less impact from inclusion particles in a high ductility, equiaxed grain material due to crack tip blunting associated with greater plasticity and work hardening induced stability. The greater the ductility, the less sensitive the material will be to sharp notches. The grain to inclusion size ratio implies that when inclusion particles become large relative to the microstructural size scale, they impact material properties to a greater extent. The ratio of matrix to inclusion moduli indicates that harder inclusions should be less compatible with the surrounding, relatively soft material matrix. Finally, defects may not impact fatigue life in the low cycle regime due to rapid material degradation associated with general slip irreversibilities, thus, the greater the test stress relative to the endurance limit, the less the impact of particles on life variability. The final term is certainly limited in interpretive value because we also know that in a brittle material, a large enough defect at high loads will cause catastrophic brittle fracture. All terms are expected to be applicable only to generally ductile systems.

3.5.5.1. Ductility

Increased ductility in the direction of the applied load should promote crack tip blunting and a reduced tendency to initiate FCG near inclusion sites. The tendency of crack tip blunting to retard and/or arrest incipient FCG has been discussed in several recent studies [17, 50, 76, 77].

3.5.5.2. Relative Microstructural Size

In MP35N, most of the initiation sites were found to contain inclusions on the order of 2 to 10 μm in size. 35N LT initiation sites comprised mixed mode initiation with competition between 0.5 to 2 μm particles and similar sized preferentially oriented grains. This limited data infer that an increased grain diameter to inclusion size ratio should promote initiation at features other than constituent particles.

3.5.5.3. Relative Elastic Stiffness of Dissimilar Phases

The dislocation dipole model for fatigue initiation at inclusions predicts reduced life for increasing particle stiffness (μ'). This is a result of decreased phase boundary compliance and an associated increase in the rate of stress accumulation during dislocation pile-up [40]. In addition to the boundary compliance effect, high stiffness phases such as TiN ($\mu' = 240$ GPa) should possess lower fracture toughness than the MgO ($\mu' = 155$ GPa) particles present in 35N LT, resulting in increased propensity for particle fracture and crack growth in the surrounding matrix. The limiting case would include a situation where the coherently bonded phase particle is of a similar stiffness to the surrounding matrix. Particles in this case would qualitatively not be expected to participate in the fatigue fracture initiation process as much as stiffer ones.

3.5.5.4. Relative Test Stress Level

The present data, as well as previous studies on the fatigue of fine wire specimens [4, 5, 18], have demonstrated reduced variability in fatigue life at relatively high stress, low cycle conditions. In these cases, while fatigue cracks may initiate at inclusions, the total life is not significantly affected by their initial size. It is expected that as the stress level is reduced towards the fatigue limit, variability associated with the size distribution of defects will increase. Of importance is the idea that in HCF conditions, inclusion particles play a role of increasing importance.

3.6 Tables and Figures

Table 3.1 Deterministic Parameters for MP35N wire.

Parameter	Value	Units
μ	89.63	GPa
μ'	240	GPa
d	2.5	μm
c	5	μm
M	3	unitless
σ_e	572	MPa
h	0.064	μm
α	0.22	unitless
λ	0.175	unitless

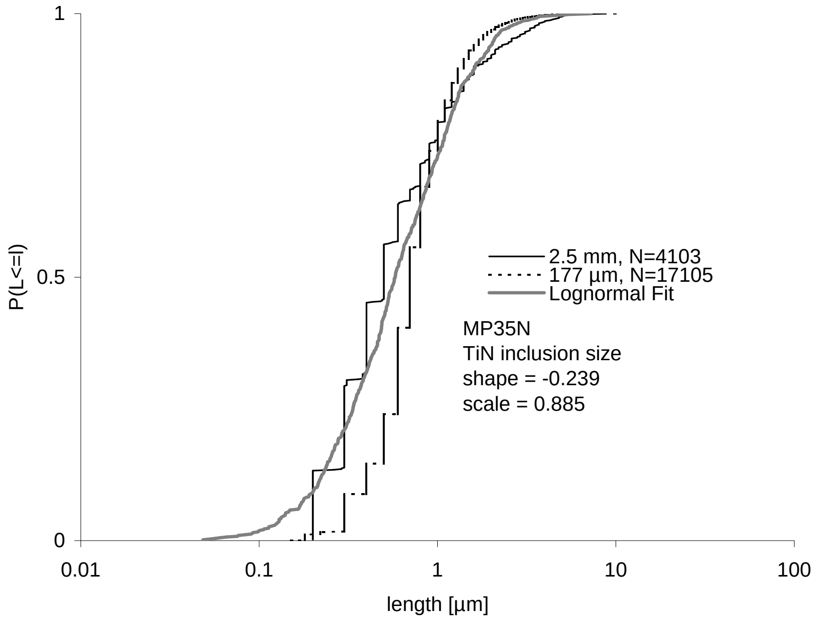

(a) MP35N

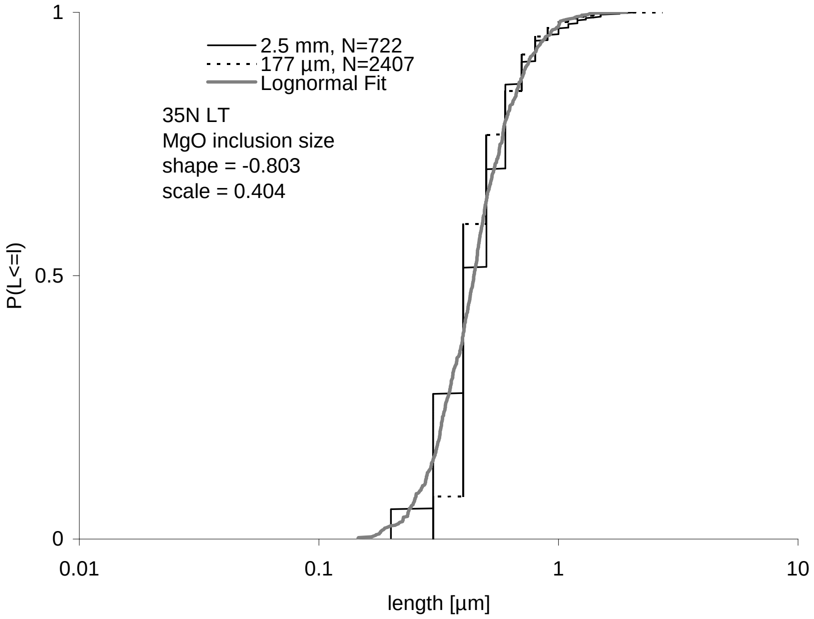

(b) 35N LT

Figure 3.1. Inclusion particle length CDF for 177 μm and 2.5 mm wire, adapted from [18].

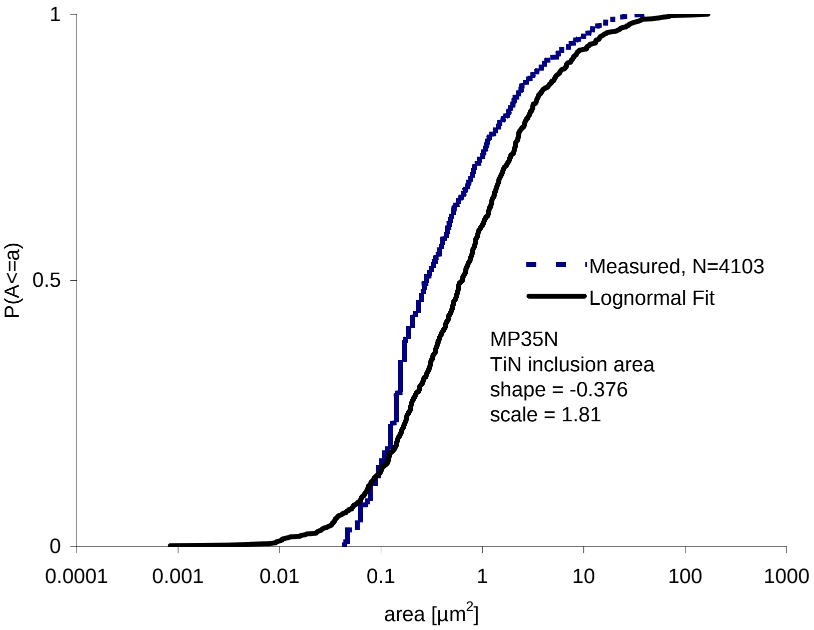

(a) MP35N

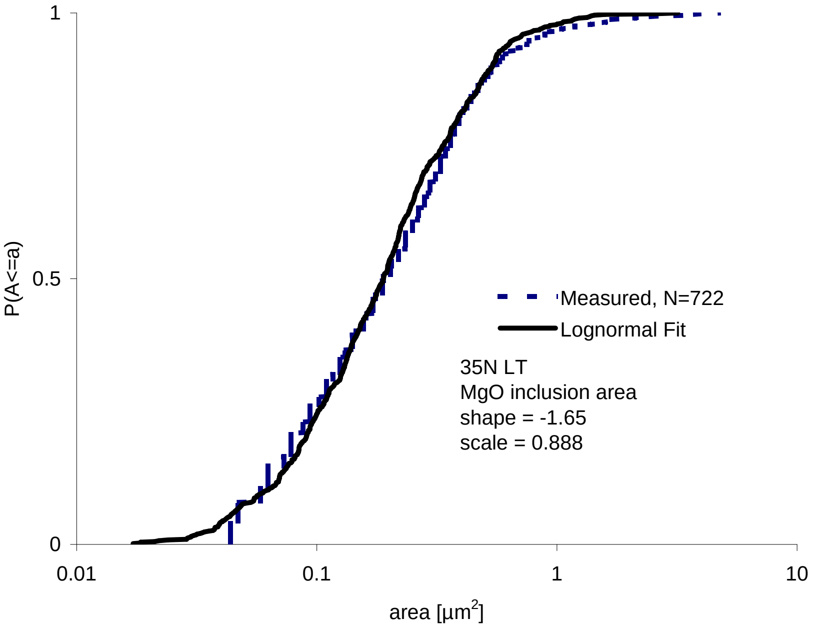

(b) 35N LT

Figure 3.2. Inclusion particle area CDF for 2.5 mm MP35N and 35N LT wire, adapted from [18].

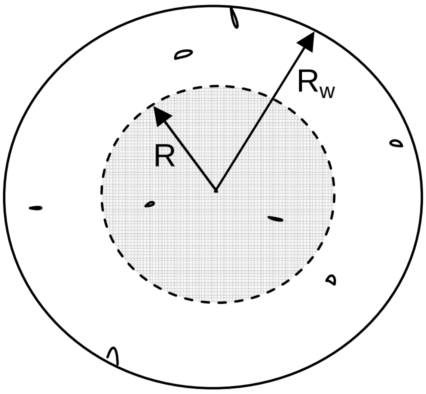

(a) Volumetric inclusion uniformity schematic.

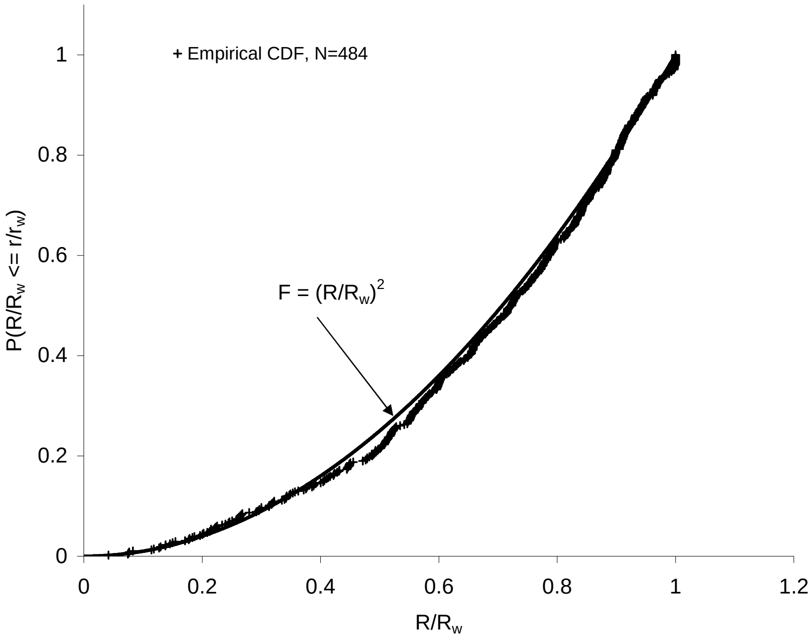

(b) Inclusion depth CDF.

Figure 3.3. Sketch of volumetric uniformity of inclusion distribution and inclusion depth CDF in MP35N and 35N LT wire adapted from [18].

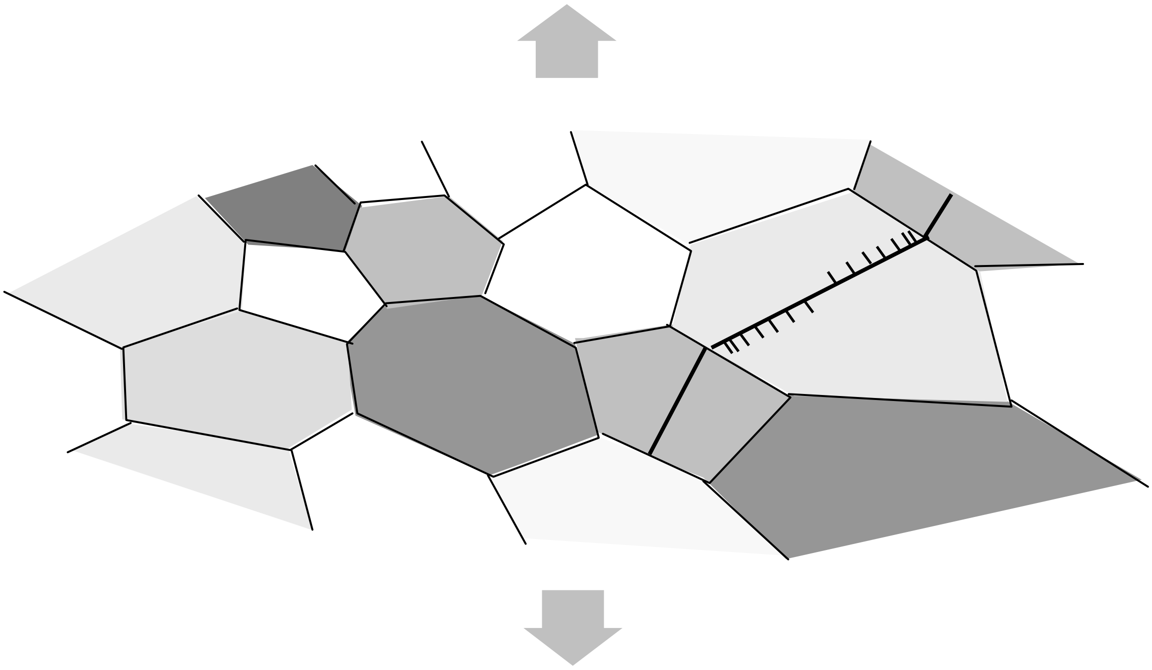

Figure 3.4. Schematic of incipient plasticity in a single, preferentially oriented, grain and the subsequent dislocation pile-up mediated slip activation in adjacent grains.

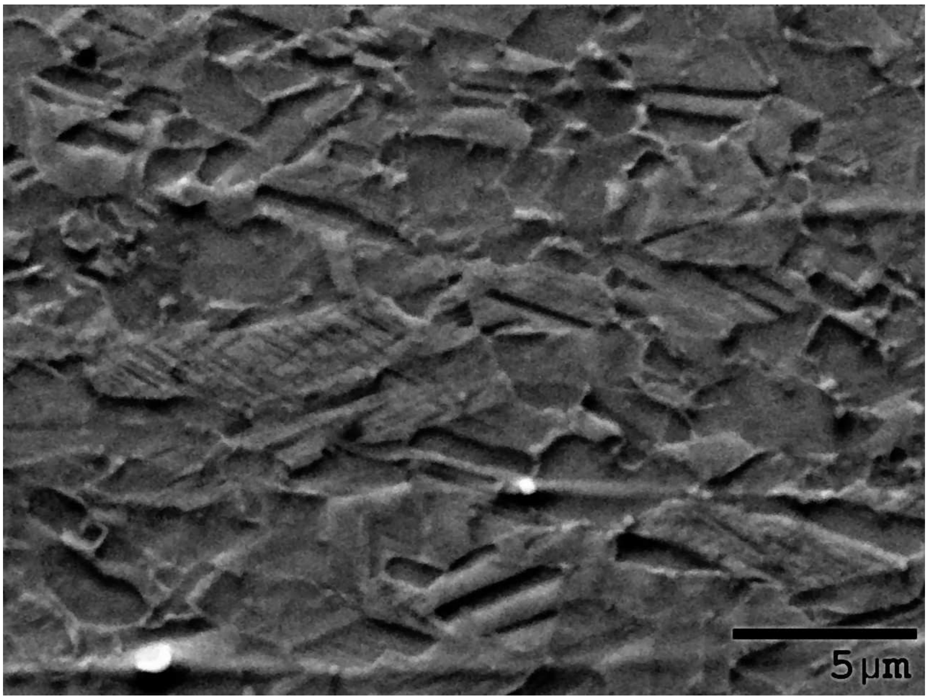

(a) Longitudinal interior micrograph of grain structure in 177 μm 35N LT.

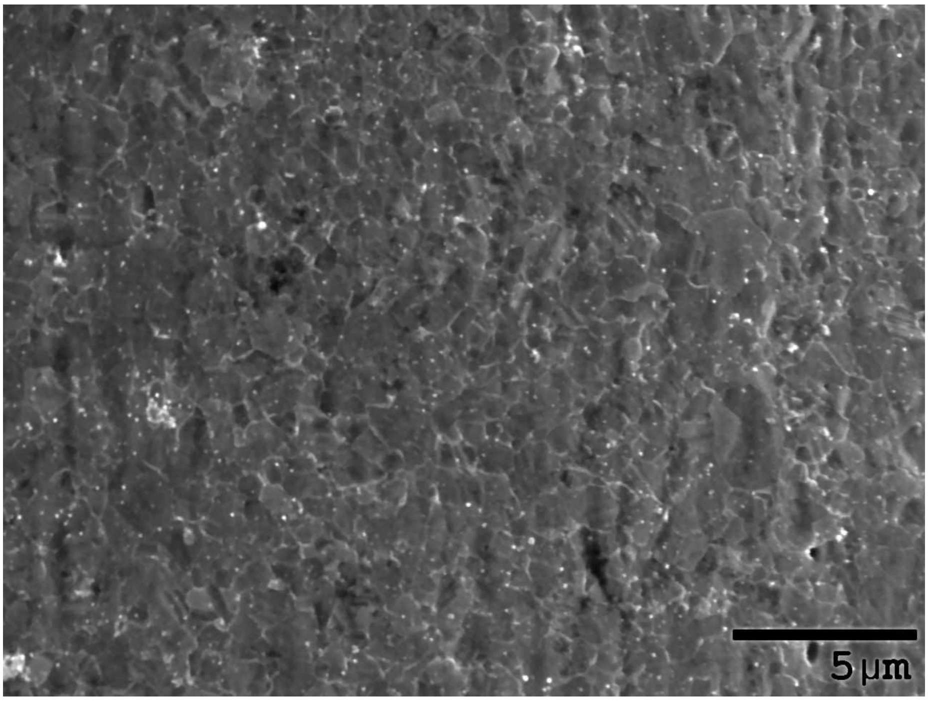

(b) Longitudinal surface micrograph of grain structure in 177 μm 35N LT.

Figure 3.5. Example of relatively fine surface grain size in 177 μm 35N LT wire.

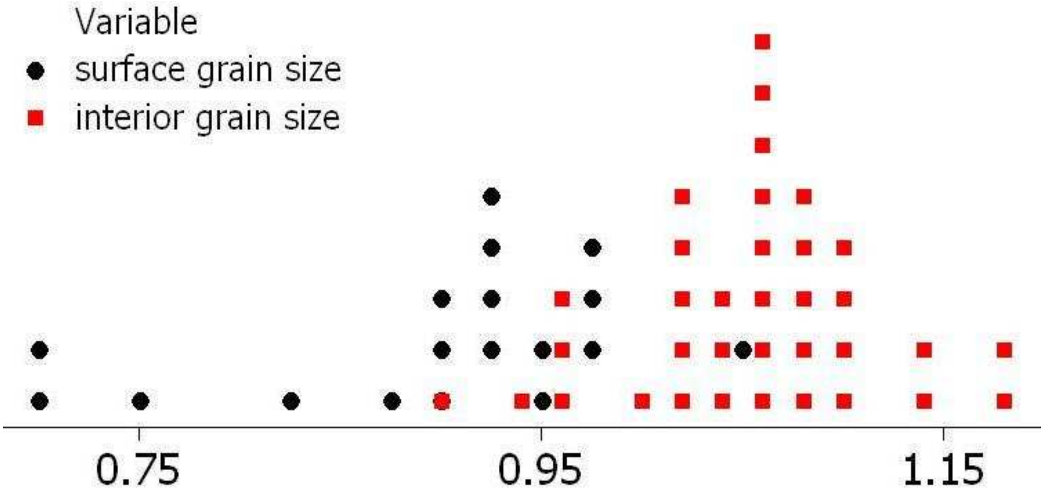

Figure 3.6. Finer normalized grain size in surface vs. the interior of 35N LT wire.

4. EXPERIMENTAL DESIGN AND PROCEDURE

4.1 Specimen Design

Both materials used for this investigation were initially cast into 1360 kg [3000 lb] vacuum induction melt (VIM) electrodes which were vacuum arc remelted (VAR) into 432 mm [17 in.] diameter ingots. After a homogenization treatment, the VAR ingots were reduced on a rotary forge (GFM) machine to produce 100 mm [4 in.] diameter billet which was subsequently hot rolled on a continuous rolling mill to 5.6 mm [0.219 in.] diameter coil. The coil was annealed, shaved to 5.5 mm [0.216 in.] and pickled in preparation for drawing. Intermediate reduction from 5.5 mm to 1.6 mm [0.064 in.] was accomplished using carbide drawing dies and powder lubricants. Additional processing to the final diameter of 177 +/- 5 μm [0.0070 +/- .0002 in.] was completed using diamond dies and mineral oil lubricants. A qualitative comparison between the surface characteristics of each material was performed using SEM. Generally, the 35N LT was found to possess a more uniform surface due to fewer and smaller intrinsic surface defects. These findings were consistent with results reported in earlier studies [4, 18].

4.2 Specimen Preparation

The first objective of this research was to elucidate important microstructural factors driving life and life variability in fine medical grade wire. Fine medical wire is not generally modified beyond its drawn form for use in medical coils and cables. In order to derive results consistent with product used in the field, specimen preparation for rotary beam fatigue testing was minimized. Cold drawn wires typically possess a plasticity induced radius of curvature known in the wire industry as cast. This feature arises primarily due to slight intentional misalignment as the wire exits the final drawing die and serves to stabilize the material as it wraps on a spool. This curvature was mechanically corrected prior to rotary beam evaluation by gently reverse bending each sample before loading them in the chuck fixture. This procedure reduces wobble in the fixture and has been shown over extensive data sets using many materials to reduce geometric instability and unnecessary test variability [78].

The rotary beam fatigue testers used are equipped with a sensor to detect wire fracture. As soon as a sample break occurred, the ends were suspended in a plastic tube to prevent mechanical damage. The fatigue fracture ends were cleaned in an ultrasonic bath for 45-60 seconds in high purity acetone before being serially mounted to an aluminum mounting block.

Sample sections for SEM metallographic evaluation for grain size and internal structure data were first mounted in a hot press using a thermoset mounting material. These samples were mechanically polished through progressively finer stages of silicon carbide paper and finished with 1 μm diamond and 0.05 μm Alumina slurry prior to a brief superalloy etch. Surface grain size analysis samples were not polished beyond the natural diamond drawn state with the exception of a brief etch to reveal structural detail.

4.3 Material Condition Selection

Three nominal strength levels and two grain sizes were targeted for evaluation: a 1310 MPa [190 ksi] ultimate tensile strength (UTS) annealed specimen possessing an equiaxed, nominally 2.5 μm grain structure, an annealed specimen possessing an equiaxed, nominally 1.5 μm grain structure, material strain hardened to 1930 MPa [280 ksi] UTS, and a final sample at 2206 MPa [320 ksi] UTS. The latter two strain hardened samples were selected for their applicability to current use within the medical device field, particularly for use in implantable lead design. The equiaxed structures were selected in order to study the expected growth and arrest of short fatigue cracks at grain boundaries. Cold drawing ASTM F562 wire results in a multiphase reaction comprising a strain-induced crystallographic transformation from annealed parent face-centered-cubic (FCC) to FCC with dispersed thin platelets of another phase. Some studies have suggested this phase is a hexagonal-close-packed (HCP) structure [55], while others [79] debate its true nature. It is known that this transformation in combination with significant strain induced twinning in this low stacking fault energy (SFE) material makes discernment of original grain boundaries difficult.

4.4 Mechanical Testing

The tensile properties including:

- 0.2% offset yield load
- Maximum load before rupture (break load)
- 0.2% offset yield strength
- Ultimate tensile strength
- Total strain before rupture (elongation)
- Young's modulus of elasticity

were measured at the finish drawn diameter on an Instron®[1] model 4469 load frame using a 1 kN load cell at a constant strain rate of 0.0083 s^-1.

4.4.1 Elastic Modulus

Accurate measurement of the modulus of elasticity using a tension test in fine wire requires accurate strain and load measurement. While load measurement cells tend to be very accurate, inconsistencies often arise due to difficulty in accurately measuring strain within the critically stressed center region of the test gage (away

---

[1] Instron® is a registered trademark of Instron Corporation, Norwood, MA, USA

from the grips). In large diameter material, this is accomplished using a contact or optics-based extensiometer system. To date, these systems are not commercially available for wire diameters less than several hundred microns. Other methods of modulus measurement have been attempted including nanoindentation [80], torsional pendulum, experimental tension methods [81], and by resonance methods [82]. In lieu of the current variability in testing results as well as test methodology, the measured modulus of elasticity was not used in stress calculation. Rather a published value of 233 GPa [4] in conjunction with a Poisson's ratio of 0.300 was used as deterministic input to all aspects of modeling and stress determination during fatigue testing.

4.5 Residual Stress Determination

Samples of all materials used in this study were sent to Lambda Technologies for X-ray residual stress determination. The test procedure utilized provides a residual stress to depth profile in micron level increments beginning at the surface and progressively moving toward the center of the wire. In this test, a raft of wires is created by aligning approximately 50 wires on the same plane side by side to yield a raft width of 6-10 mm. The ends of the raft are epoxy mounted to prevent reorientation of the material once the test has begun. An initial X-ray diffraction scan is recorded at the surface. The material is then electrochemically milled to remove several microns of material and re-scanned. Lambda uses their own finite-element-based stress relaxation algorithm to correct for changes in the stress profile as constraining layers are sequentially removed [83]. The final output is a corrected stress-depth profile taken to be the average of the original residual stress content in the raft of material and as the longitudinal stress in the individual drawn wire.

4.6 Constituent Particle Survey

Constituent particle surveys were completed in the MP35N and 35N LT alloys systems using SEM and energy dispersive spectroscopy (EDS) techniques. Particle size and location were determined using digital analysis software, while inclusion composition was determined using EDS. Two types of inclusion populations were determined: the overall distribution of particles intrinsic to the alloy itself, and the distribution of particles that were responsible for incipient fatigue fracture.

4.6.1 Overall Intrinsic Particle Distribution

Constituent particles were measured using SEM techniques with BEI imaging to increase contrast between the non-metallic inclusions and the base alloy matrix. The inclusion analysis used for modeling the overall particle distribution was carried out on polished, transverse cross-sections of both 2.5 mm and finished 0.177 mm diameter wire. These analyses were carried out at Materials Evaluation & Engineering (MEE) using an automated field acquisition system. The automation allowed examination of many high magnification fields at once; this was necessary to gather sufficient data for good statistical computation. The analysis method pulled data from a total of 1.73 mm^2 of area per lot of material. The transverse area of a 2.5 mm wire is 4.91 mm^2; in this material, the image fields were gathered from several sections of material over 10 different material vintages.

At the fatigue test diameter of 0.177 mm, the necessary evaluation area required analysis of hundreds of wire sections. To facilitate the area requirement, the fine wire material was bundled into 19 filament, concentrically wound cables, mounted in the transverse orientation and examined at a rate of several magnification fields per filament. The results of this analysis were used to elucidate differences in particle size and spatial distribution after significant deep-draw processing.

4.6.2 Crack-Nucleating Particle Distribution (CNPD)

Each fatigue failure was examined using SEM techniques to determine the near-initiation morphology and likely cause of failure. At each particle-based initiation site, the particle's radial and circumferential length were measured, as well as the approximate area, and depth location. An example of analysis for initiation at a delaminated particle site is shown in Figure 4.1. The crack-nucleating particle distribution was fit to a statistical distribution and compared to the overall distribution as well as to model output.

4.7 Grain Size Measurement

For each sample, wires were metallographically prepared in the interior-longitudinal, surface-longitudinal and transverse orientations. The samples were etched with a solution consisting of 14 ml HCl, 4 ml HNO_3, and 0.5 g $CuCl_2$. SEM was used to image the resulting microstructures.

4.7.1 Internal Grain Size

For each of the equiaxed-grain, annealed samples, wires were metallographically prepared in the interior-longitudinal and transverse orientations. The samples were etched with a solution consisting of 14 ml HCl, 4 ml HNO_3, and 0.5 g $CuCl_2$. SEM techniques were used to image the resulting microstructures.

Six photomicrographs of representative microstructures were taken for each sample in each direction. The grain sizes were then determined using the Abrams three circle interrupt procedure described in ASTM E112 on the SEM photomicrographs. The average grain size and standard deviation were calculated from the six measurements.

4.7.2 Surface Grain Size

The sample surface grain size was found using a similar procedure. Unprepared, short sections of each wire were etched by immersion into a solution containing 14 ml HCl, 4 ml HNO_3, and 0.5 g $CuCl_2$. The wire surfaces were then examined using SEM techniques. Similarly, six photomicrographs of representative microstructures were taken for each wire sample. The grain sizes were determined using the Abrams three circle interrupt procedure described in ASTM E112 on the SEM photomicrographs. No corrections were made to account for the convex surface that was represented in the images. The average grain size and standard deviation were calculated from the six measurements.

4.8 Rotating Beam Fatigue Test Protocol

Rotating beam fatigue testing (RBT) was carried out using a Valley Instruments model 10.040 test machine (reference Figure 4.2). This equipment uses a 3600 rpm synchronous direct-drive motor to spin a custom fine-wire collet. The angular displacement from the direct drive is transmitted along an elastic, fine-wire member in a fixed-curvature wire path. The minimum curvature of the path determines the maximum alternating strain and is fully determined in an initially straight and elastic round wire by the the center distance (L_C) from the drive-proximal chuck to the distal free bushing, and the sample test length.

Machine set-up involves calculating the desired sample length and center distance using the assumed modulus of elasticity of the material and equations developed by Valley Instruments Company in ref [84]. Stress calibration in the manual is based on the assumption of a central neutral bending axis and a linear strain distribution that is proportional to the radial distance from the wire's center line. Samples are loaded by inserting one end into the fine wire collet shown in Figures 4.3(a) and 4.3(b) in the static and energized conditions respectively. The free end is placed directly in a low-friction phenolic bushing in which it is free to rotate (reference Figure 4.4).

Model 10.040 RBT devices are equipped with a synchronous motor that is directly clocked by a timer running an LCD display resolving time to one hundredths of a second; the theoretical cycle resolution is thus 36 revolutions. The accuracy of the machine is not discussed in the manual, however; the expected accuracy of the device is very good due to its ac-based synchronous drive circuitry and the inherent frequency consistency and corrections applied to the general power grid to maintain proper industrial systems and time clock synchronization [85].

4.9 Methods of Fractography

In this investigation, three methods of analysis were used to gather information related to: cause of failure, general fracture morphology, crack-initiating particle size, particle composition, grain size and persistent slip band spacing. The methods included SEM, FIB and SEM with EDS.

4.9.1 Hitachi S4800 FE-SEM

A Hitachi S-4800 cold field emission SEM was used to gather both low magnification images as well as high resolution ($< 3nm$) fatigue striation information. The S-4800 instrument uses a hairpin tungsten emitter and achieves a maximum resolution of 1.0 nm at an accelerating voltage of 15 kV. The PC-controlled 5 axis motor driven stage allows excellent sample manipulation for imaging difficult or low emission coefficient fracture surface features. The semi-in-lens detector allows gathering of pure secondary electron (SE) signal for maximum resolution and signal-to-noise as well as a mixed SE/BE signal for creating compositional contrast, for example in imaging non-metallic inclusion initiation sites. The S-4800 FE-SEM used in this work is shown in Figure 4.5(a).

4.9.2 FEI Nova200 FIB

The Nova 200 FIB incorporates a dual beam system with high resolution FE-SEM capability, as well as, focused ion beam milling for real-time microstructural preparation and iterative analysis [86]. This instrument was used in this work primarily to achieve grain orientation contrast by means of secondary ion imaging techniques. The goal was to utilize this information to further elucidate the role of microstructural features such as twin boundaries in crack initiation and propagation and to gather qualitative information on local grain orientation in the vicinity of the fatigue crack front. The Nova 200 SEM/FIB equipment used in this work is shown in Figure 4.5(b).

4.10 Fatigue Crack Growth Rate Determination

Early on in this research, it was hypothesized that fatigue crack growth may contribute significantly to total life in fine wire, even in the megacycle life range. Measurements of the crack growth rate were made using high resolution SEM (HR-SEM) to confirm the validity of this idea. Other methods of crack growth rate measurement, including live growth observation, were intended for these modeling efforts in order to study crack-arrest-related lifetime contributions. Unfortunately, time constraints did not allow completion of the live crack growth experiment and crack arrest life was necessarily estimated from SEM fractography of crack front striations.

4.10.1 HR-SEM Striation Determination

HR-SEM techniques were used to determine the spacing between fatigue striations near initiation and throughout the fatigue fracture zone. These measurements were taken as an average over a given sample length at magnifications ranging from 100KX to 600KX. Averaged striation width data were associated with a corresponding stress intensity level for given stress and crack-size conditions and plotted on the ordinate of a crack growth rate curve for MP35N. This data were also used to estimate the total FCG life in fine wire 35N LT and MP35N specimens.

4.11 Tables and Figures

Table 4.1 Average mechanical properties of 177 μm MP35N and 35N LT, adapted from [18].

Sample ID	S_Y (MPa)	S_{UTS} (MPa)	Strain at rupture
MP35N-1310	876	1262	35.0 %
35N LT-1310	924	1289	35.0 %
MP35N-1930	1600	1889	4.00 %
35N LT-1930	1710	1889	3.60 %
MP35N-2206	1696	2158	2.80 %
35N LT-2206	1813	2158	2.80 %

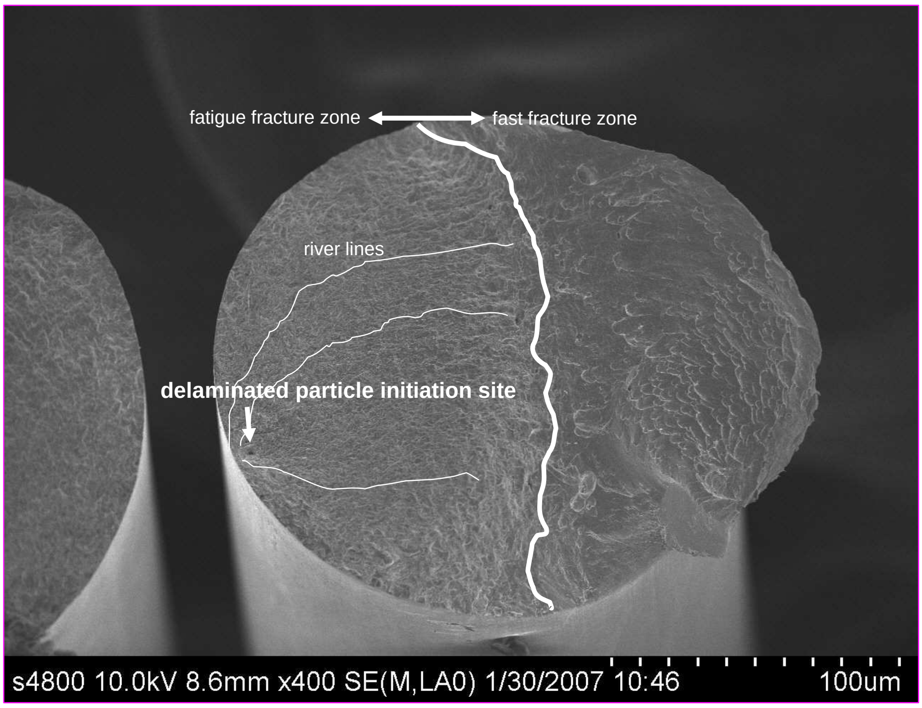

(a) Crack-initiating, delaminated particle site in 1930 MPa, 35N LT tested at $S_a = 930MPa$, $R = -1$, specimen failed in $7.41x10^4$ cycles.

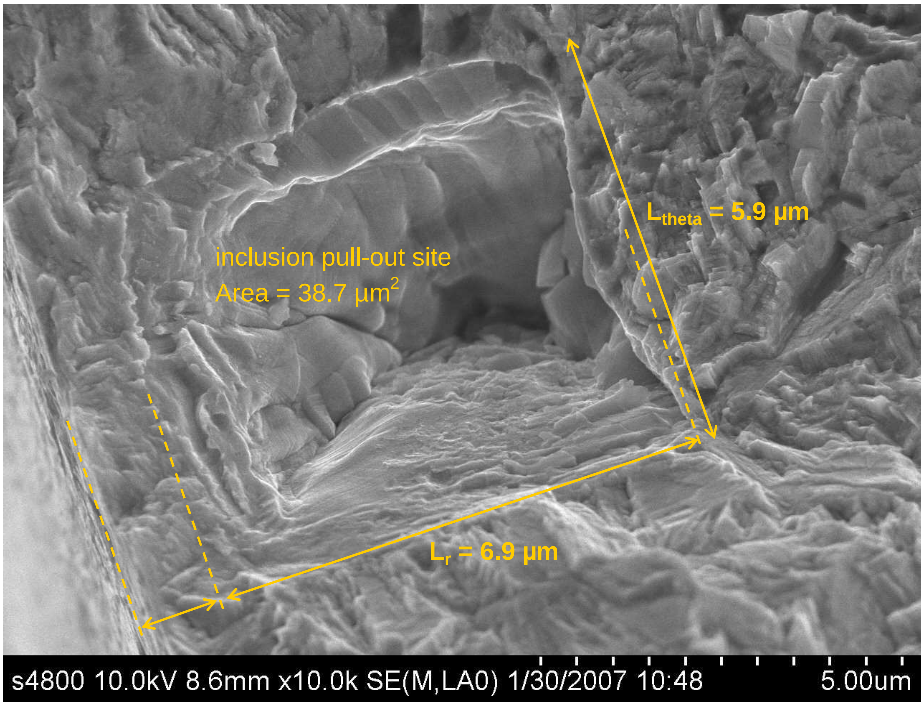

(b) Closeup of initiating region in 4.3.

Figure 4.1. Analysis of initiation region in MP35N wire using SEM methods.

Figure 4.2. Valley Instruments (currently a division of Positool, Inc.) model 10.040 rotating beam fatigue tester.

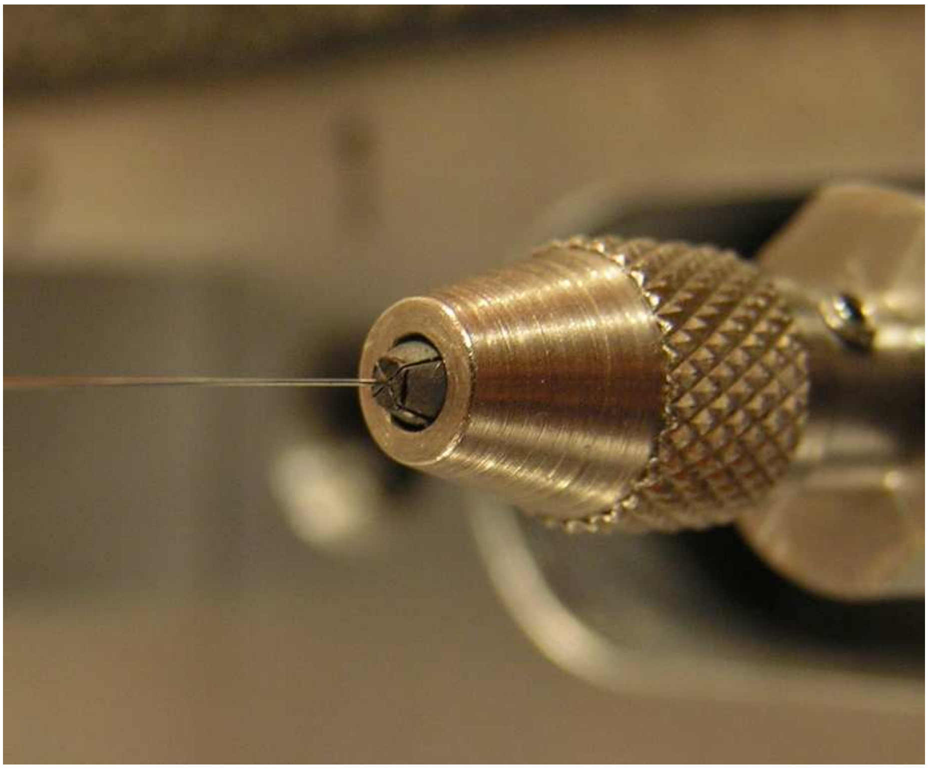

(a) Static chuck.

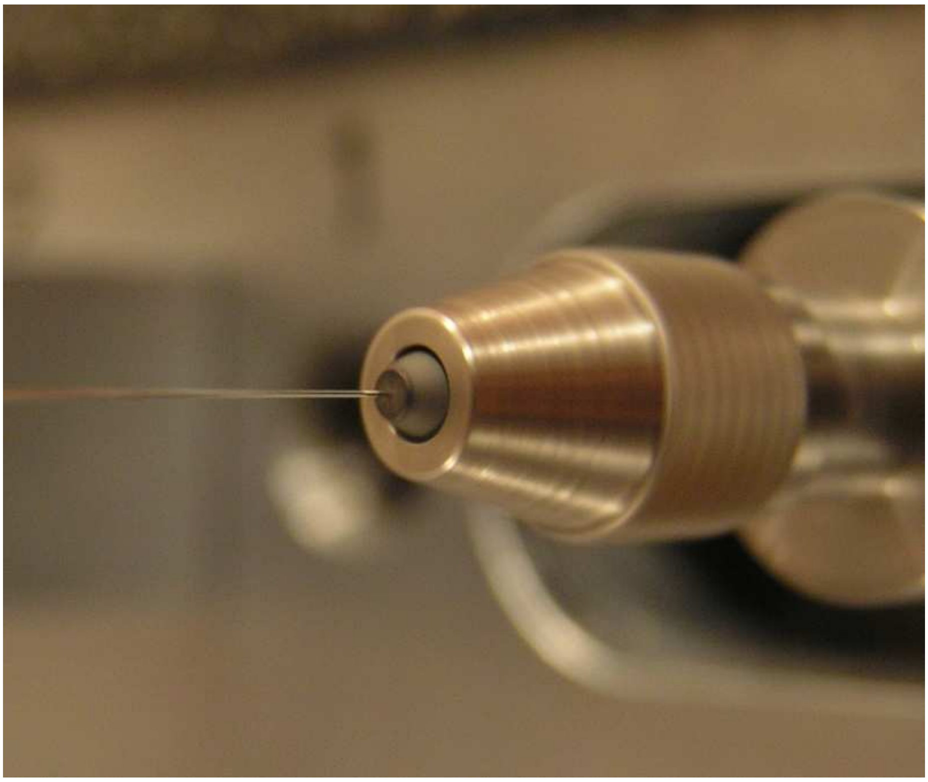

(b) Dynamic chuck, energized and rotating at 60 Hz.

Figure 4.3. Rotating beam tester model 10.040 fine wire collet and chuck (wire shown is 177 μm 35N LT).

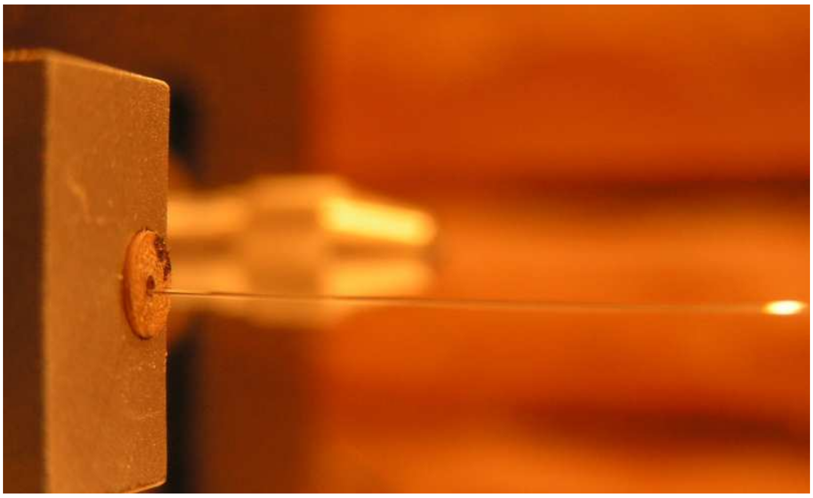

Figure 4.4. Fine wire, free bushing support on model 10.040 rotating beam fatigue tester (wire shown is 177 μm 35N LT).

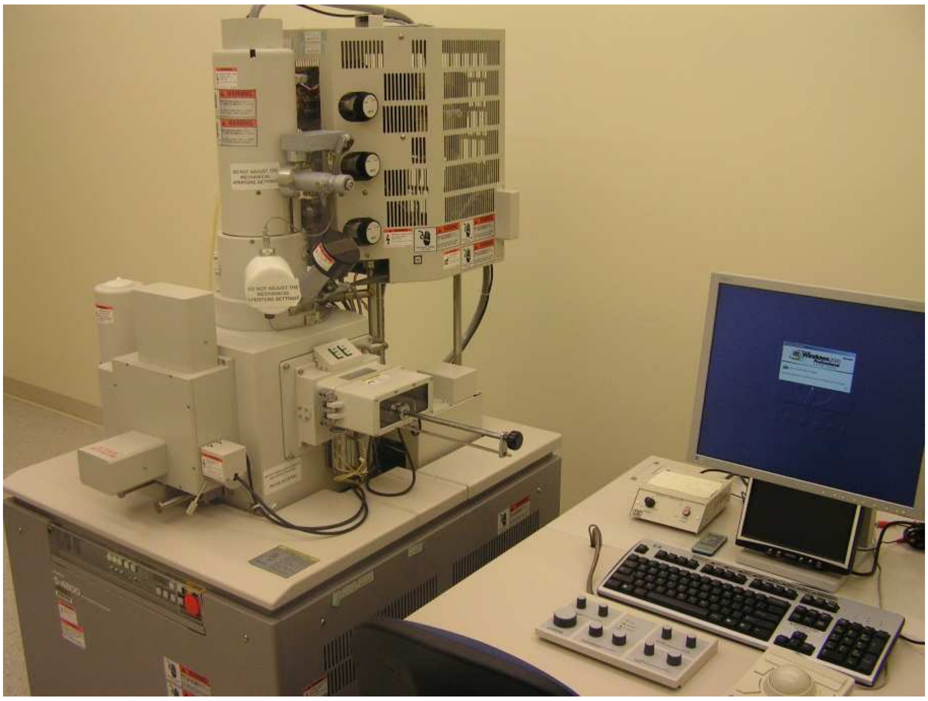

(a) Hitachi S-4800 FE-SEM.

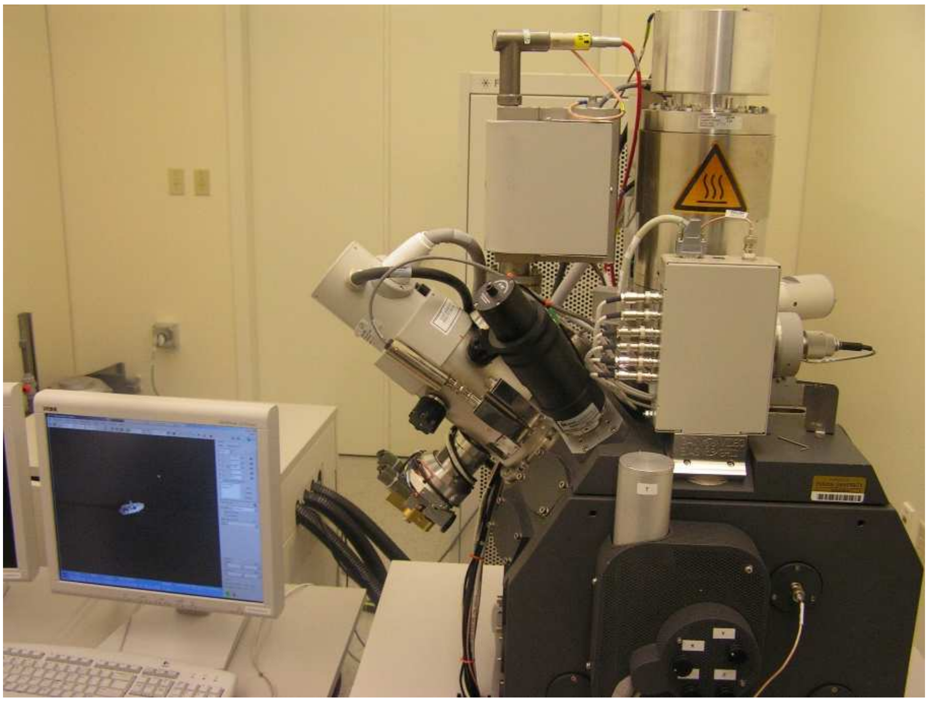

(b) FEI Nova 200 dual beam SEM/FIB.

Figure 4.5. Equipment used in fractography analysis of MP35N and 35N LT failure specimens.

5. RESULTS AND DISCUSSION

5.1 Monotonic Tensile Properties

Anisotropy in the MP35N alloy system has been demonstrated in the literature [56]. There exists intrinsic anisotropy associated with the random orientation of individual grains as well as strain induced anisotropy associated with the non-random tendency to produce fiber orientation during cold drawing [54]. Since fatigue failure in these types of fine wire often involves crack nucleation within a single grain, bulk variation in strength (as measured in a standard tensile test) that may be associated with other macroscopic influences was not considered appropriate input to the model. In this case, the strength properties were treated as deterministic input parameters to all aspects of the model and in stress calculation for fatigue testing. In the future, controlled nanoindentation techniques to monitor relative intragranular and intergranular mechanical property variation may be a way to more realistically account for strength variation at the fatigue initiation size scale. The measured bulk tensile properties were found to be comparable for both alloys and are shown in Table 4.1.

5.2 Residual Stresses

The stress ratio in a fatigue test was defined by Equation (2.12) as the minimum stress divided by the maximum stress. In a rotary beam fatigue test, the stress is assumed to alternate about a zero mean stress and move from a maximum tensile stress to an equivalent magnitude compressive stress. The result is a stress ratio of $R = -1$ that is assumed to hold throughout the specimen. In the case of a residual-stress-free material, this is a valid assumption. Cold drawn wire rarely meets the stress-free criterion and often resides in a state of residual tensile stress at the free surface where fatigue cracks typically initiate. This means that the stress ratio on a microscale is not $R = -1$, or any other constant value as the residual stress present will change based on the local grain constraint conditions.

A determination of the average longitudinal residual stresses was made using X-ray diffraction techniques and is presented in Figure 5.26. From this plot, the effective stress ratio was applied to yield the actual stress cycle as a function of depth from the wire surface in Figure 5.25(a). The stress ratio at depth is represented in Figure 5.25(b). The consensus in the literature [46, 51, 87–89] is generally that an increasing stress ratio leads to a reduced fatigue stress intensity threshold due to greater crack operation and less crack closure. There is a dearth of information, however, with respect to the theoretical relationship between the mean stress and initiation life. While the present data may be used to explain observed below-threshold FCG, the current model for initiation life does not explicitly take into account stress ratio variability.

5.3 Constituent Particle Distributions

The results of statistical analysis of the overall inclusion size distribution were adapted from [18] and are shown in Figures 3.1, 3.3 and 3.3(b). Using the CNIF methods described earlier, these data were filtered in order to find the distribution of particles likely to cause failure.

5.3.1 Crack Nucleation Intensity Factor

The CNIF methodology was used in the model to sort the important defect structures from the non-critical background noise of overall defect distributions. Equations (3.4) and (3.5) were used for crystal and inclusion features respectively. The results of CNIF analysis were used to predict crack-nucleating particle size, depth, life and were ultimately compared to experimental data for several material states and test levels.

5.3.2 Crack-Nucleating Particle Size

CNIF analysis coupled with the hierarchical model structure resulted in good agreement with experimentally observed crack-nucleating particle sizes. The initial particle size CDF was transformed to the crack-nucleating CDF given in Figure 5.27. The tendency of cracks to form at larger particles within the critically stressed region is evidenced by the rightward shift of the original CDF.

The measured crack-nucleating particle distribution was also compared to the model output. This data are presented as a frequency dot-plot with respect to inclusion size in Figure 5.28. A similar trend was observed for both the MP35N and 35N LT alloy systems. The results of the experimentally measured crack size CDF are compared to the model output crack size CDF in Figure 5.29. In this form, it is evident at first glance that the SIF-based CNIF for inclusion size yielded better agreement with experimentally observed data. It must be noted, however, that the life variability was found to be much more sensitive to inclusion depth than inclusion size. This fact made the relationship given by Equation (3.5) a better sorting mechanism in the complete model. Finally, both CNIF methodologies agreed well with experimental data at the fifth and ninety-fifth percentiles.

5.3.3 Crack-Nucleating Particle Depth

The crack-nucleating particle depth was well predicted by use of Equation (3.5). The agreement between the predicted and observed data set is represented statistically as a CDF in Figure 5.30. The ability to predict critical inclusion depth was an important discovery in this research because of the strong empirical relationship found between inclusion depth (from the free surface of the wire) and total fatigue life. Results of SEM depth measurement at crack-nucleating particle sites were plotted against total fatigue life in Figures 5.31 and 5.32 for the MP35N and 35N LT alloy systems respectively. These results were obtained for 1930 MPa strain hardened material at alternating stress test levels of 620 and 827 MPa for MP35N and 35N LT.

The depth-life trends were found to be similar for both alloy systems, though the scatter was greater in the 35N LT. The increased scatter was expected because of the small size scale of initiating particles compared to other microstructural features such as the grain size. For example, incipient crack formation at a 2 μm preferentially oriented grain was arrested several times at grain boundaries in Figure 5.33. In each case life increased as critical particles initiated further toward the low stress interior of the wire. The model was further validated by comparing life prediction data and associated nucleating particle depth to experimental data for 177 μm MP35N, strain hardened wire. These data are presented in Figure 5.35.

5.3.4 CNIF-based Life Prediction

The CNIF for particle based fatigue crack initiation was chosen to reflect increased propensity of near-surface inclusions to cause more rapid damage than those located at the wire interior. An example of life prediction using both CNIF's is shown for MP35N in Figure 5.34. While both methods yielded good correlation to the tenth percentile of failure probability, the chosen model more accurately depicts experimental variability. It also yielded more conservative prediction compared to the SIF-based selection model at higher failure probabilities. This result is attributed to the stronger affect of depth within this relationship, which was found to be consistent with actual measurements.

5.4 Results of Fatigue Testing

The average fatigue testing results generally matched well with median life predictions for all examined cases. Perhaps more importantly than a nominal life prediction, the model also well predicted variability and factors influencing variability in a variety of conditions tested. The validity of the initiation life model is important. It gives researchers a framework to examine effects of not only nominal or maximum defect size, but also the effects of statistical defect distribution on life variability. Further-more, based on fatigue testing results and ensuing SEM investigation, the proposed CNIF algorithm has been shown to give a valid transformation from a general defect distribution to a crack-nucleating distribution.

5.4.1 Annealed Material

The 1310 MPa materials used in this study possessed an average grain size of 2.5 to 3.0 μm. In addition, these materials possessed significant ductility ($>$ 30% total strain to rupture) that should have promoted crack tip blunting in the presence of sharp inclusions. Both the MP35N and 35N LT in the 1310 MPa strength state were expected to fracture primarily at microstructural defects such as surface psb's over inclusion particles. The SEM collage in Figure 5.38 shows one such initiation where an inclusion at the incipient crack site was not visible.

Additional evidence of the material's indifference to inclusion size in this condition is presented in CDF form in Figure 5.3. At a 2.5 μm GS, the materials behaved similarly in terms of median life as well as life variability. As the grain size was reduced, the inclusions began to generate premature fracture in the MP35N and the CDF became distinctly shifted. In the future, it is hoped the IHF will lend some predictability to this phenomenon.

The lifetime variability was generally well predicted for the annealed samples in the 1310 MPa strength condition (2.5 μm GS) at both the ends of the CDF for all stress levels as shown in Figures 5.4(a) and 5.5(a). Similar results for a single test level were obtained at the 1 μm GS as shown in Figures 5.8(a) and 5.9(a). At the fifth percentile for failure, the model results were generally conservative compared to experimental data. From a design perspective, this is a valuable observation as failure is not acceptable for these material systems. A typical stress-life representation of the annealed data is presented in Figures 5.4(b) and 5.5(b) for the 2.5 μm GS material. A limited amount of data were also collected for an annealed GS of 1 μm and is presented in Figures 5.9(b) and 5.8(b). Here, more data are needed to understand how well the model will work to predict other test levels.

5.4.2 Cold Drawn Material

Some deterministic values in the model, such as the universal constant and endurance limit, were fit to experimental data. This does not imply that the model fit is synthesized, rather it shows the model contains useful quantitative microstructural information and sufficient flexibility to model uncertainties that are not yet well understood. Evidence of model robustness lies in the fact that most parameters derived for the cold drawn, 1930 MPa MP35N wire were carried over for the 35N LT, with the exception of inclusion data. The values that were modified for the 35N LT included: a reduced inclusion modulus of rigidity (Al_2O_3 softer than TiN), appropriately modified Monte Carlo simulated inclusion size input, and an increased endurance limit.

The median life and lifetime variability for both cold drawn materials were well predicted by the initiation model. CDF format model data exhibited good fit to experimentally derived information as shown in Figures 5.6(a) and 5.7(a). Similar to the annealed wires, at low failure probability, the model results were generally conservative compared to experimental data. Typical stress-life representation of the cold drawn data is presented in Figures 5.6(b) and 5.7(b). Here it is interesting to notice the two modes associated with initiation in the 35N LT system. This is also seen in Figure 5.6(a) as a kink in the experimental CDF at the 827 MPa test level. This result was found to be primarily related to the occurrence of extended lifetimes in samples that did not fracture at near surface particles. This result was predicted *a posteriori* by the empirically derived IHF relationship.

5.4.3 Comparison to Historical Data

In 1998, Altman *et al.* [5] presented one of the few extensive studies on the fatigue life of medical grade wire used in cardiac lead systems. In the decade to follow, with the exception of several internal studies [4, 18], little additional work has been published for fine, medical-implant-grade, wire. The material used in ref [5] comprised MP35N and MP35N-DFT composite wire specimens that were primarily tested in the hard drawn condition. Material was tested both in wire and medical multi-filar coil form using a rotary beam test arrangement.

The Altman data set was adapted and compared to the present model output for MP35N in the strain-hardened, 1930 MPa strength state in Figure 5.10. With the exception of some premature failures in the Altman set at low stress levels, the data median generally matched current predictions. The factors contributing to the low failures in the Altman data are unknown. The lack of such failures in current data sets may be related to processing improvements. These could include better melting techniques resulting in smaller, more consistent inclusion distributions and better finishing practices resulting in improved surface consistency. Other variables that may have influenced their results could be related to surface damage and stress state variability associated with coil forming.

5.4.4 Failure Location in RBT Gage

Material variability in fatigue shows up not only in total life to failure but also in the location of fracture in a RBT trial. As shown in Figure 5.1, the apex in rotary bend testing is the position of maximum stress operation over the sample length and is the location of most fractures. For a total of 374 fracture events, greater than 90% were found to fail within 5.3 mm of the apex and at greater than 98% of the maximum test stress level. These results are visually reconcilable in Figure 5.2. The consistency of fracture location throughout testing is an indication of robust material preparation and RBT set-up practices as well as evidence of material surface consistency.

5.5 Initiation Hierarchy Function (IHF)

Equation (3.6) presents an empirically derived relationship that was calibrated to experimental data to yield a value between 0 and 1. The idea is that at $IHF = 0$, we do not expect inclusion based fractures, while at $IHF = 1$, we expect nearly all fatigue fractures to initiate at inclusions. The relationship does not take into account extrinsic defect structures such as tool marks or other processing related *scars*. If such features were present, it is not expected the relationship would have been of any intrinsic value. As it is given, the IHF was plotted against experimental data, that being the ratio of *other* to *inclusion-based* fractures, with good correlation and is shown in Figure 5.37.

5.5.1 Total Life Variability

Total fatigue life scatter was attributed primarily to inclusion location and size variability for hard drawn wire and to a combination of inclusion and grain size variability in annealed, high ductility samples. The results of the IHF are promising in that they may be useable in future modeling algorithms to provide refined model input that takes into account the proportion of initiation occurring at inclusion particles versus that which occurs at, for example, psb's.

Under similar HCF conditions, the 35NLT exhibited significantly more lifetime scatter as evidenced by the apparently bimodal CDF in Figure 5.4(a) at the 620 MPa test level. This increase in variability was due to multiple modes of initiation in this alloy as predicted by the intermediate IHF value and evidenced by the finding of inclusion based and other initiation modes. It should also be noted that the results for similar life in 35N LT were typically obtained at higher stress levels than in the MP35N alloy system.

5.6 Initiation vs. FCG Life in Fine Medical Wire

The striation width at various points near crack initiation and along the path of propagation were measured using SEM techniques as an estimate of the local FCG rate. Corresponding stress intensity based on estimated crack size and stress conditions at the point of measurement were also taken. The results of this data collection for a variety of material conditions is presented in Table 5.1 and represented micrographically in Figures 5.11(a) through 5.24(b).

With the assumption of minimal significant crack arrest life, the total maximum FCG life was calculated by taking the wire diameter divided by the minimum observed striation width. Naturally, the wire fails by shear overload in a RBT specimen long before initiation scale FCG occurs across the entire specimen. This lifetime is, therefore, assumed to represent a maximum life expected in the absence of a statistically significant arrest lifetime. At a minimum striation measurement of 2 nm anywhere across all specimens observed, the maximum lifetime under these assumptions was calculated to be 88500 cycles. This indicates that FCG, at the most, makes up approximately 10% of the total life in the high cycle regime beyond 10^6 cycles.

5.7 Tables and Figures

Table 5.1: Striation image data for various materials and conditions.

Image ID	Material	Strength (MPa)	Alternating Stress (MPa)	Initiation Life	est. Δ_K ($MPa\sqrt{m}$)	Average Striation Spacing (nm)
str8	35N LT	1310	621	2.44E+06	22	230
str9	35N LT	1310	621	2.44E+06	13	9.25
str10	35N LT	1310	621	2.44E+06	8.8	18

continued on next page

Table 5.1: *continued*

Image ID	Material	Strength (MPa)	Alternating Stress (MPa)	Initiation Life	est. Δ_K $(MPa\sqrt{m})$	Average Striation Spacing (nm)
str11	35N LT	1310	621	2.44E+06	7.9	21.3
str12	35N LT	1310	621	2.44E+06	2.5	8
str13	MP35N	1931	931	8.61E+04	4.8	21.25
str14	MP35N	1931	931	8.61E+04	4.8	21.25
str15	35N LT	1931	931	1.77E+05	2.9	25
str16	MP35N	1931	621	4.28E+05	3.1	10
str17	MP35N	1931	621	4.28E+05	3.1	10
str18	MP35N	1931	621	4.28E+05	3.1	10
str21	MP35N	1931	621	3.77E+05	21	50
str22	MP35N	1931	621	3.77E+05	11.1	17.5
str23	MP35N	1931	621	3.77E+05	19.7	28
str24	MP35N	1931	621	3.77E+05	23.1	500
str25	MP35N	1931	621	6.39E+05	2.26	8.5
str26	MP35N	1931	621	6.39E+05	2.26	8.5
str27	MP35N	1931	621	8.29E+05	3.92	14.25
str28	35N LT	1931	896	2.83E+05	3.27	8
str29	35N LT	1931	896	2.83E+05	3.27	8
str30	35N LT	1931	827	6.57E+05	2.53	13
str31	35N LT	1931	827	6.57E+05	2.53	13
str32	35N LT	1931	827	3.64E+05	2.43	7
str33	35N LT	1931	827	9.17E+05	2	5
str34	35N LT	1931	827	8.03E+06	3.7	12

continued on next page

Table 5.1: *continued*

Image ID	Material	Strength (MPa)	Alternating Stress (MPa)	Initiation Life	est. Δ_K $(MPa\sqrt{m})$	Average Striation Spacing (nm)
str35	35N LT	1931	827	8.03E+06	3.7	12
str36	35N LT	1931	827	1.01E+07	3.38	9
str37	35N LT	1931	827	1.01E+07	3.38	9

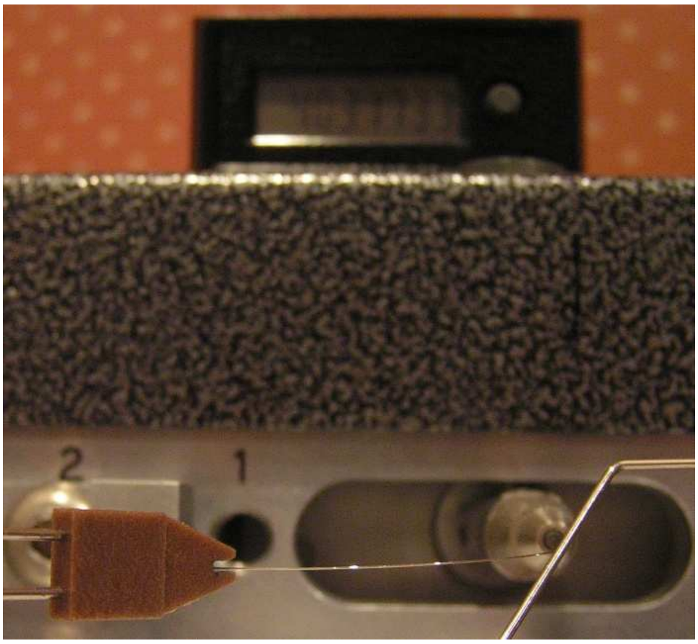

(a) Picture of the RBT gage apex during the run of a 177 μm 35N LT wire specimen.

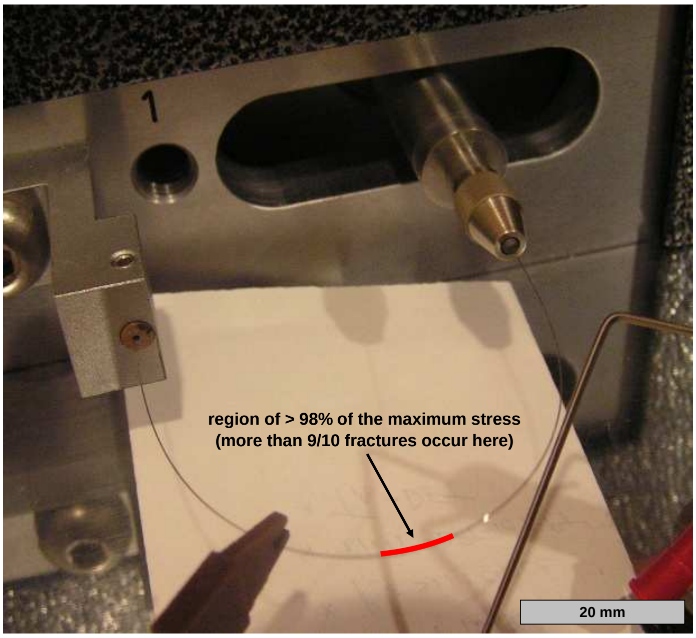

(b) Indication of the critically stressed region in an RBT gage taken during the run of a 177 μm 35N LT wire specimen.

Figure 5.1. The critically stressed apex region in an RBT test.

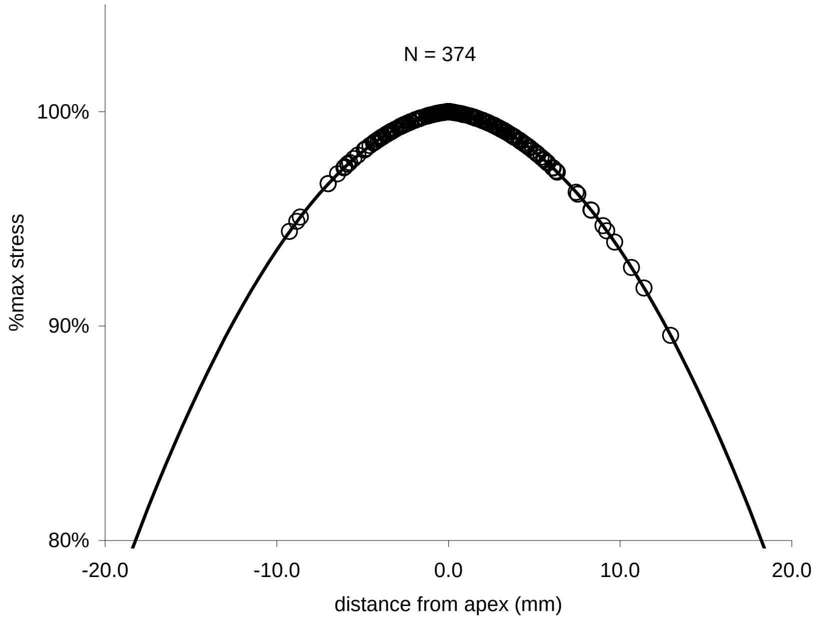

(a) Plot of the distance from the apex at which 374 RBT samples terminated with the fraction of max stress at the indicated fracture location.

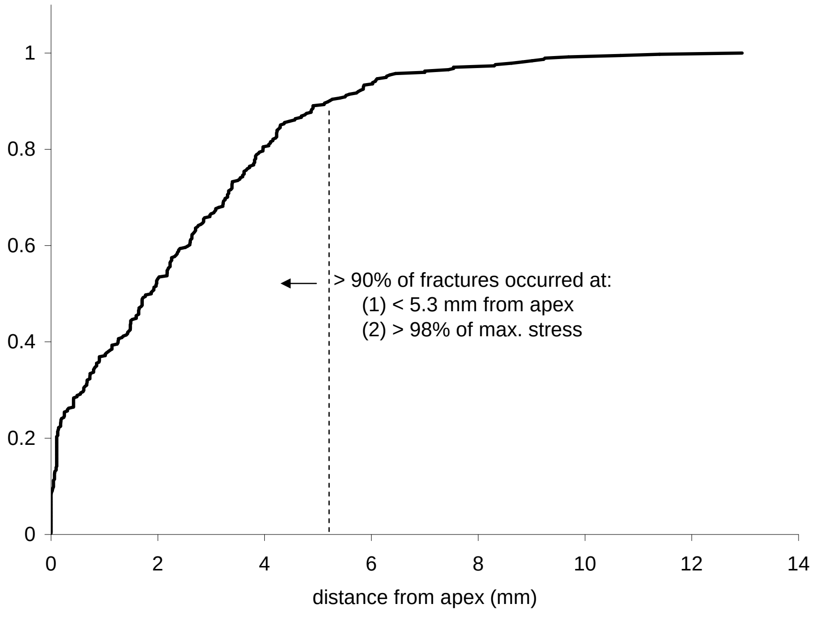

(b) CDF of the distance from the apex at which all RBT fractures occurred.

Figure 5.2. Location distribution of RBT fractures relative to the critically stressed apex region.

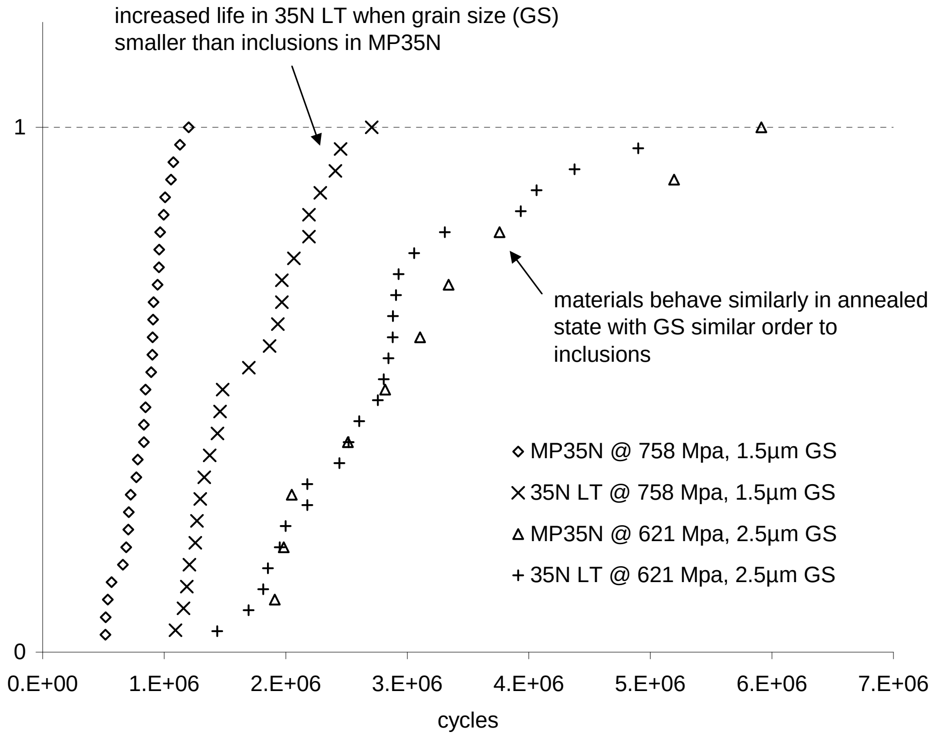

Figure 5.3. CDF for different GS materials showing the similar behavior in larger grained material with a significant downward shift for MP35N as the GS drops below the inclusion size distribution.

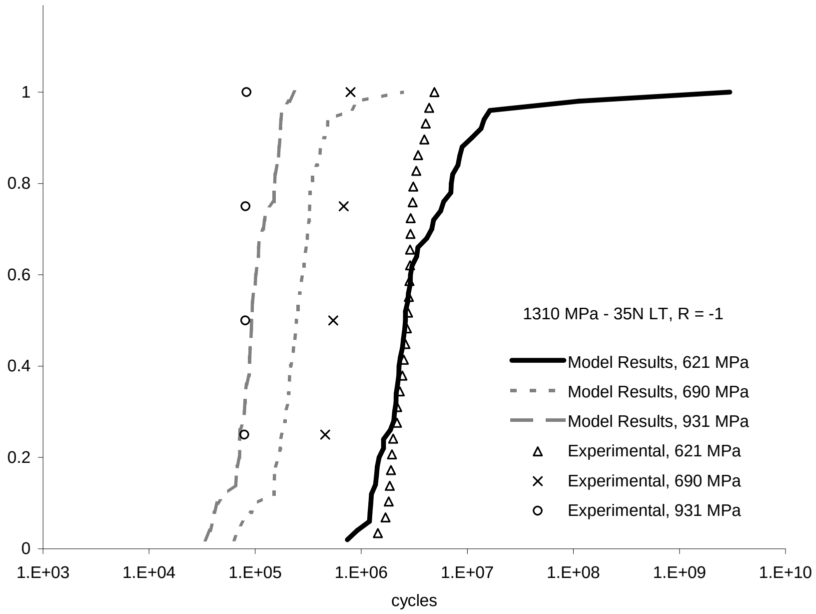

(a) CDF of experimental fatigue life data and model predictions for 1310 MPa, 35N LT.

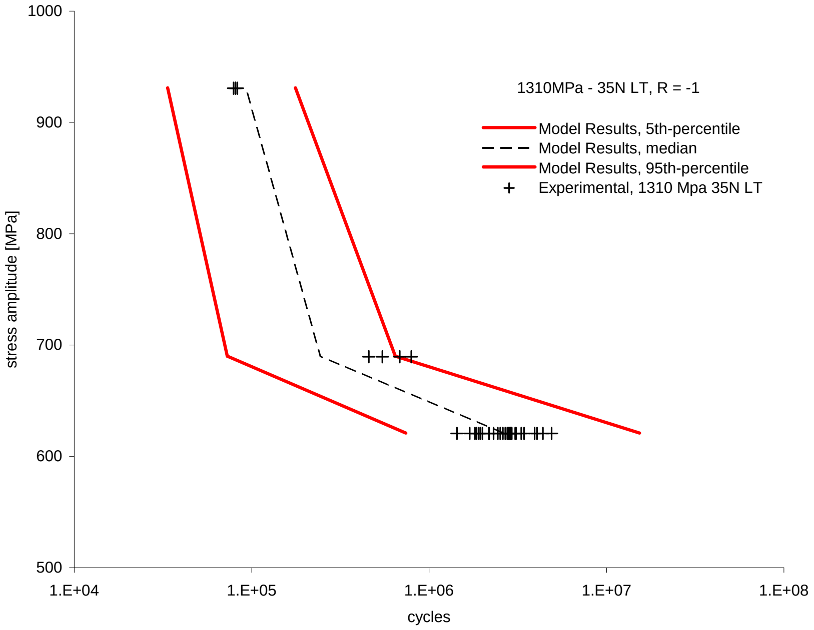

(b) S-N curve of experimental fatigue life data and model predictions for 1310 MPa, 35N LT.

Figure 5.4. Experimental and modeling results for fatigue life in 1310 MPa, 177 μm 35N LT medical wire.

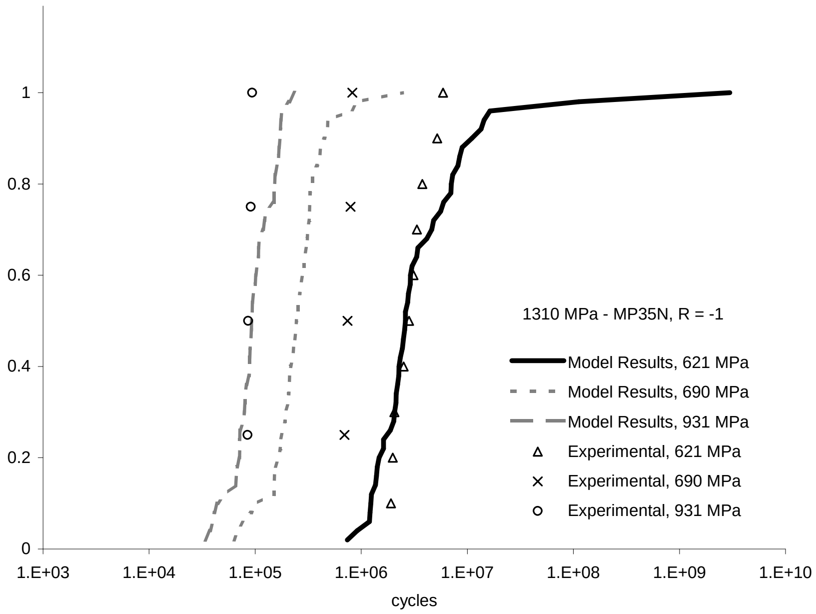

(a) CDF of experimental fatigue life data and model predictions for 1310 MPa, MP35N.

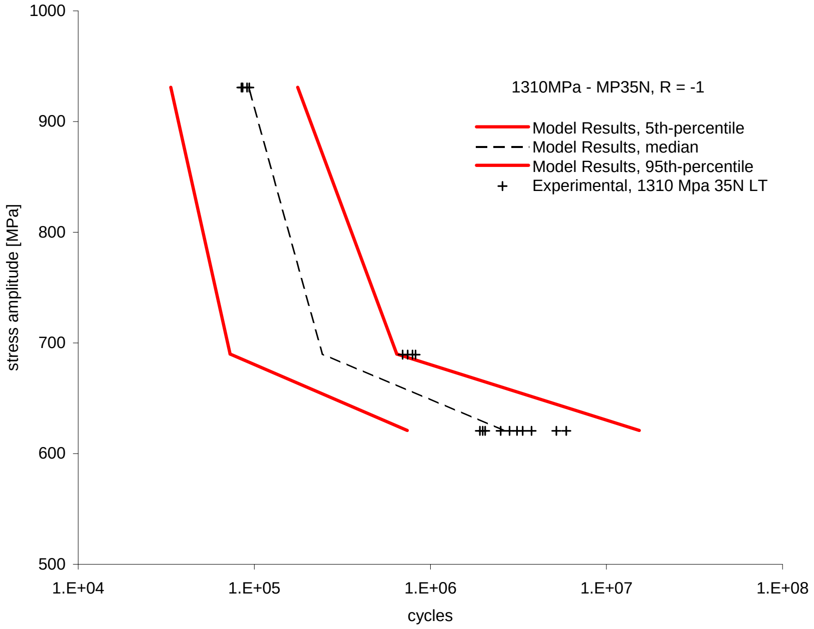

(b) S-N curve of experimental fatigue life data and model predictions for 1310 MPa, MP35N.

Figure 5.5. Experimental and modeling results for fatigue life in 1310 MPa, 177 μm MP35N medical wire.

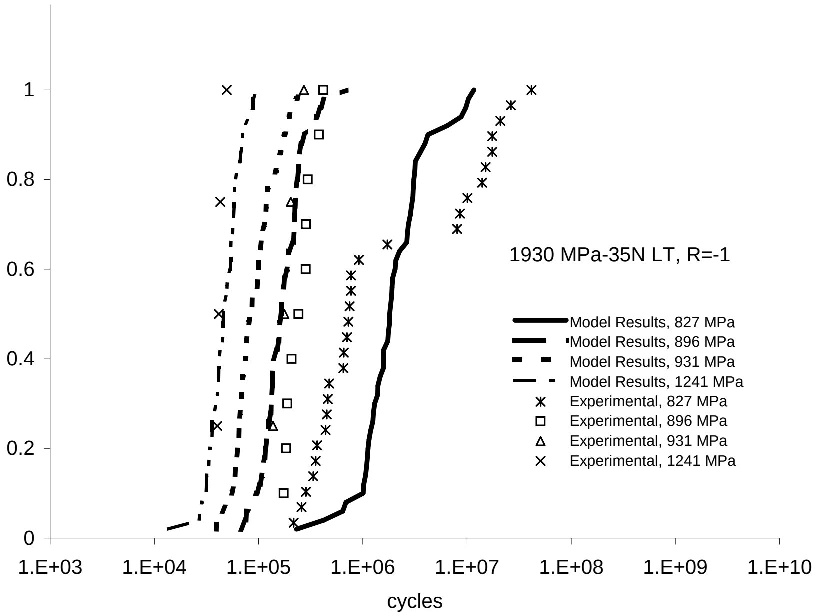

(a) CDF of experimental fatigue life data and model predictions for 1930 MPa, 35N LT.

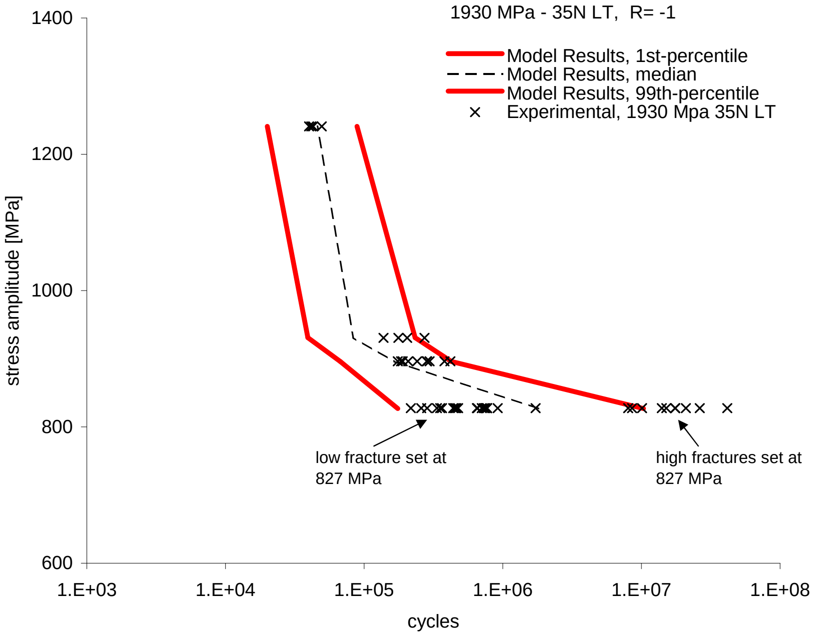

(b) S-N curve of experimental fatigue life data and model predictions for 1930 MPa, 35N LT.

Figure 5.6. Experimental and modeling results for fatigue life in 1930 MPa, 177 μm 35N LT medical wire.

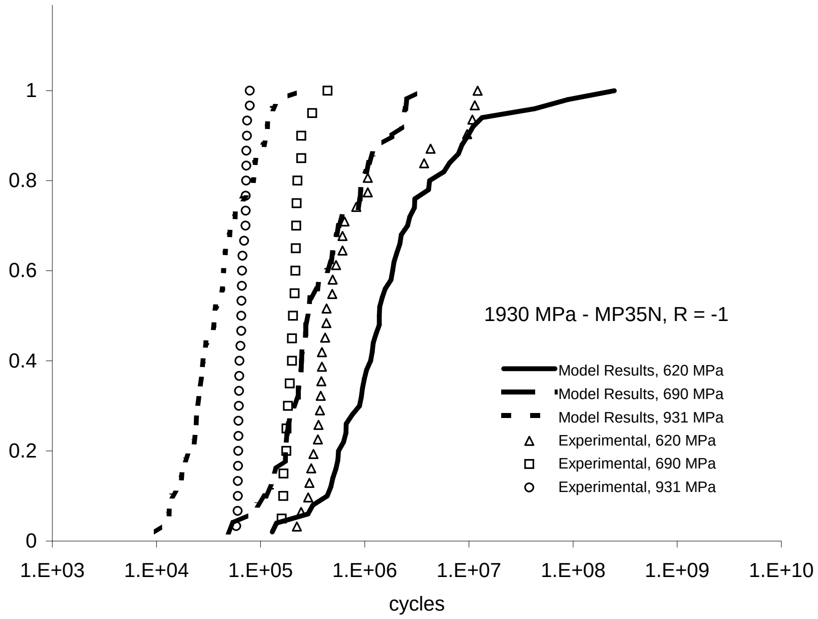

(a) CDF of experimental fatigue life data and model predictions for 1930 MPa, MP35N.

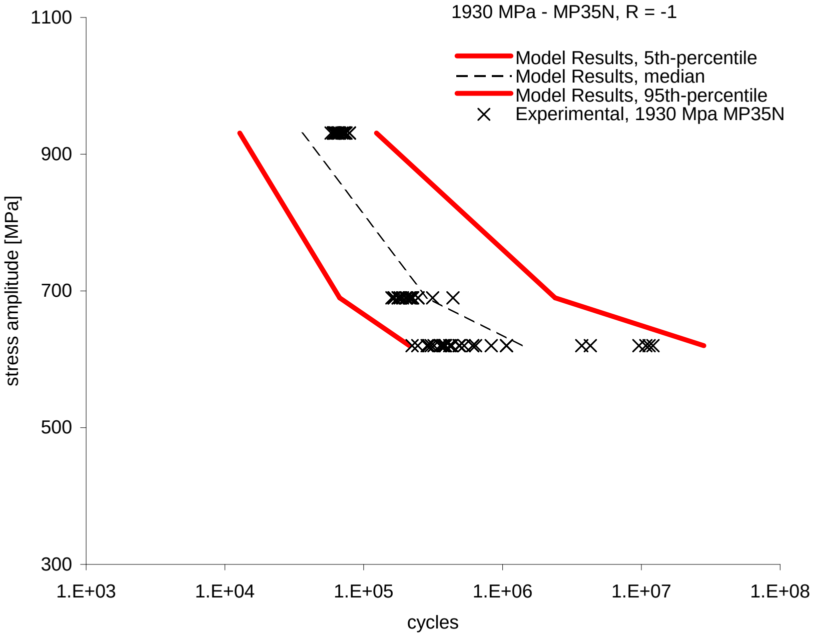

(b) S-N curve of experimental fatigue life data and model predictions for 1930 MPa, MP35N.

Figure 5.7. Experimental and modeling results for fatigue life in 1930 MPa, 177 μm MP35N medical wire.

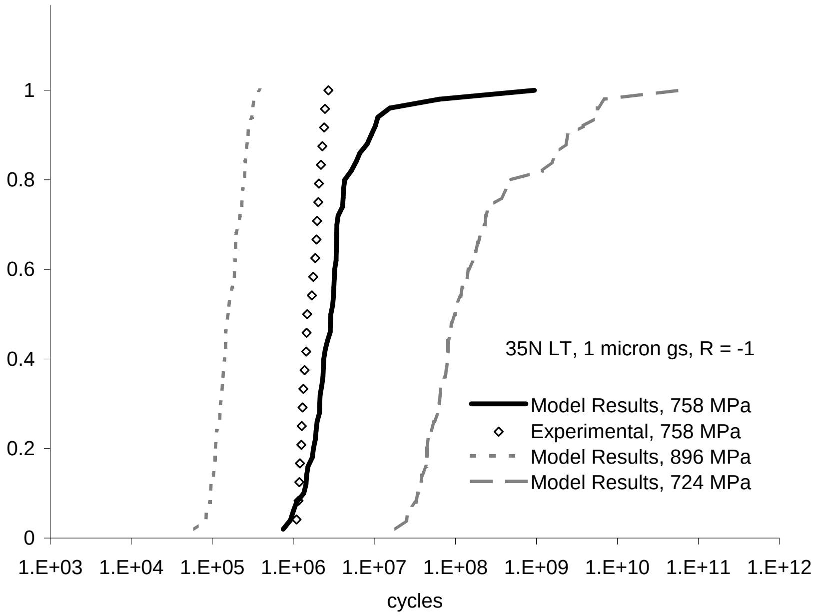

(a) CDF of experimental fatigue life data and model predictions for 1 μm GS, 35N LT.

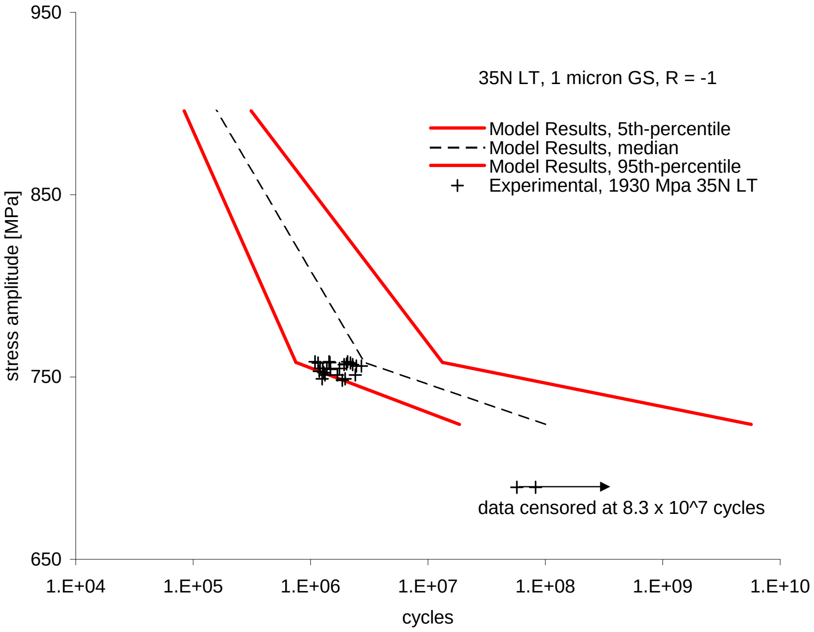

(b) S-N curve of experimental fatigue life data and model predictions for 1 μm GS, 35N LT.

Figure 5.8. Experimental and modeling results for fatigue life in 1 μm GS, 177 μm 35N LT medical wire.

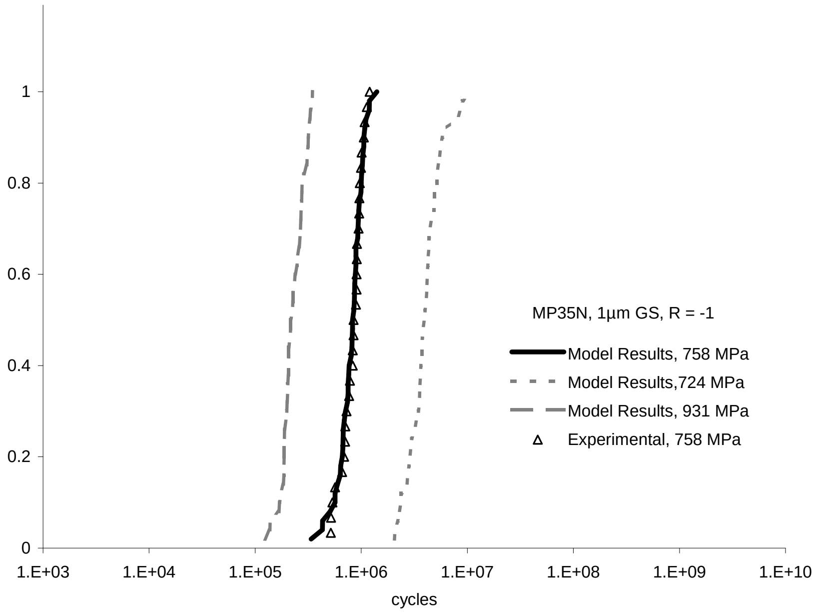

(a) CDF of experimental fatigue life data and model predictions for 1 μm GS, MP35N.

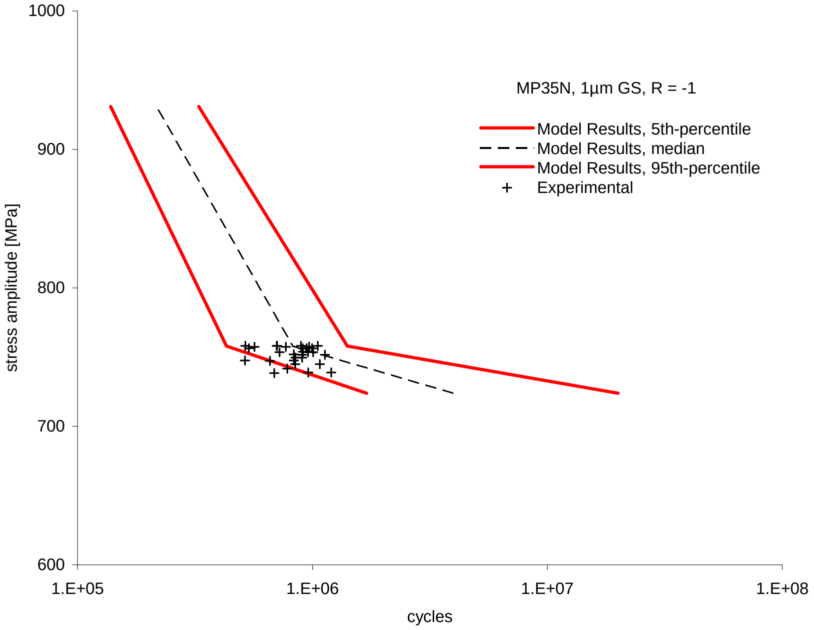

(b) S-N curve of experimental fatigue life data and model predictions for 1 μm GS, MP35N.

Figure 5.9. Experimental and modeling results for fatigue life in 1 μm GS, 177 μm MP35N medical wire.

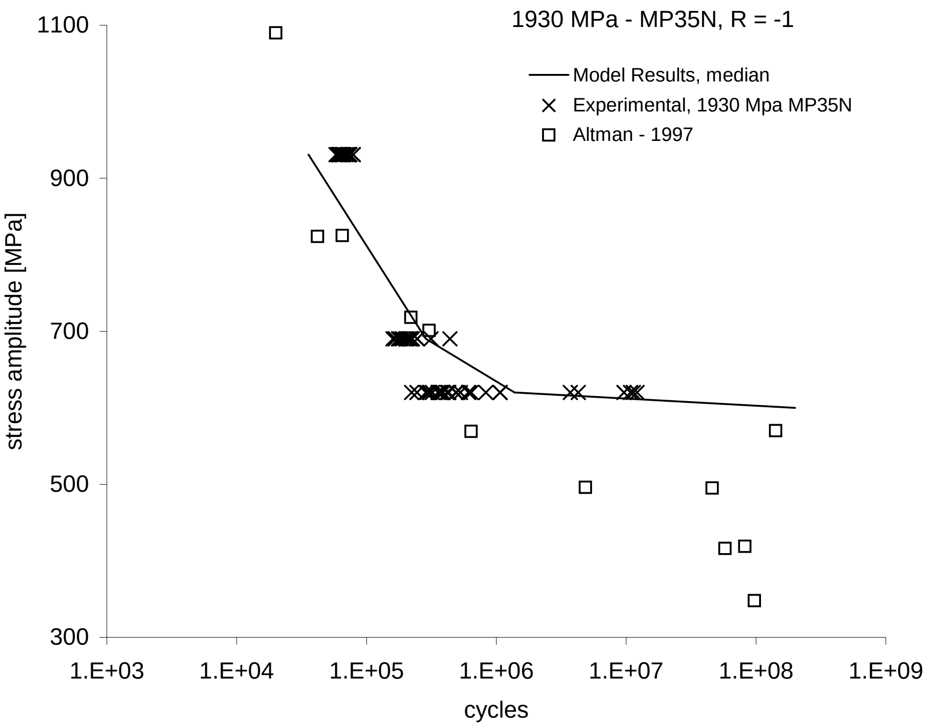

Figure 5.10. Model comparison to historically published data showing correlation to strain-hardened, 1930 MPa condition in MP35N alloy system.

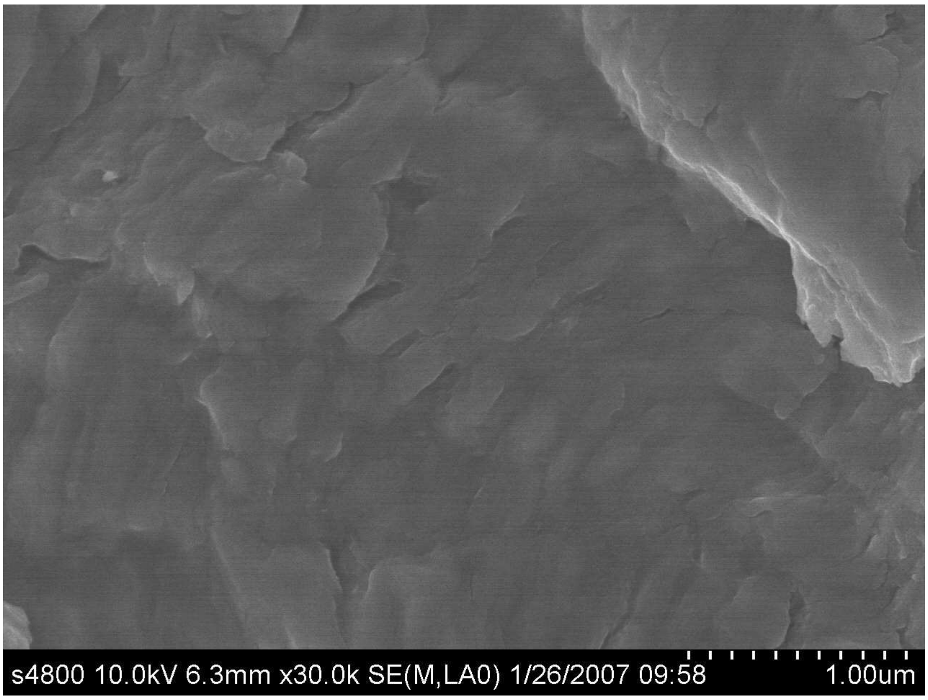

(a) Reference Table 5.1, image ID: str8.

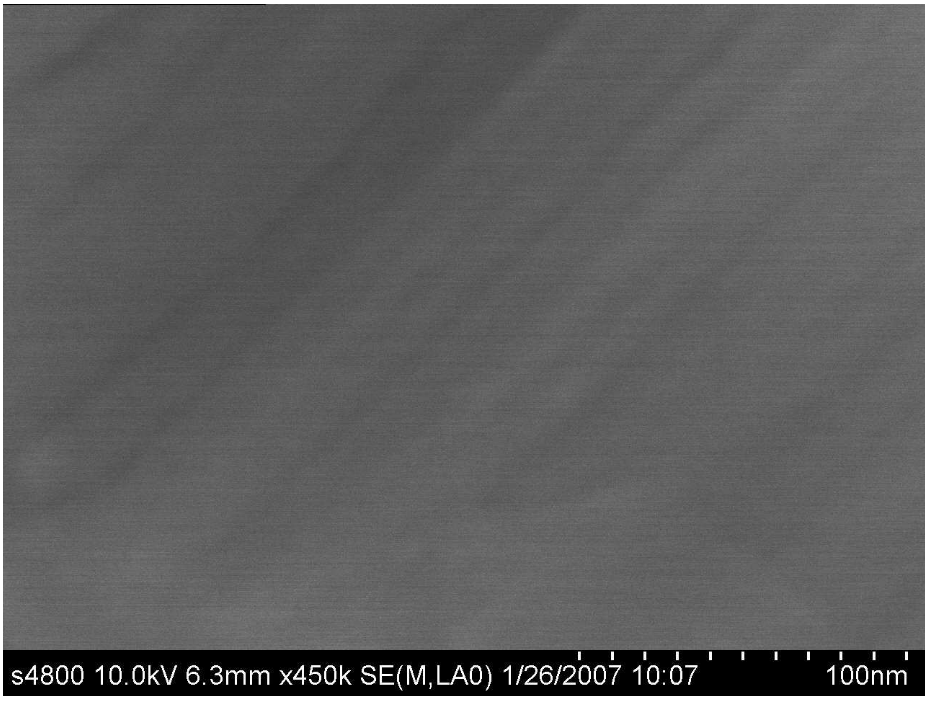

(b) Reference Table 5.1, image ID: str9.

Figure 5.11. Image ID str8 and str9 from image Table 5.1.

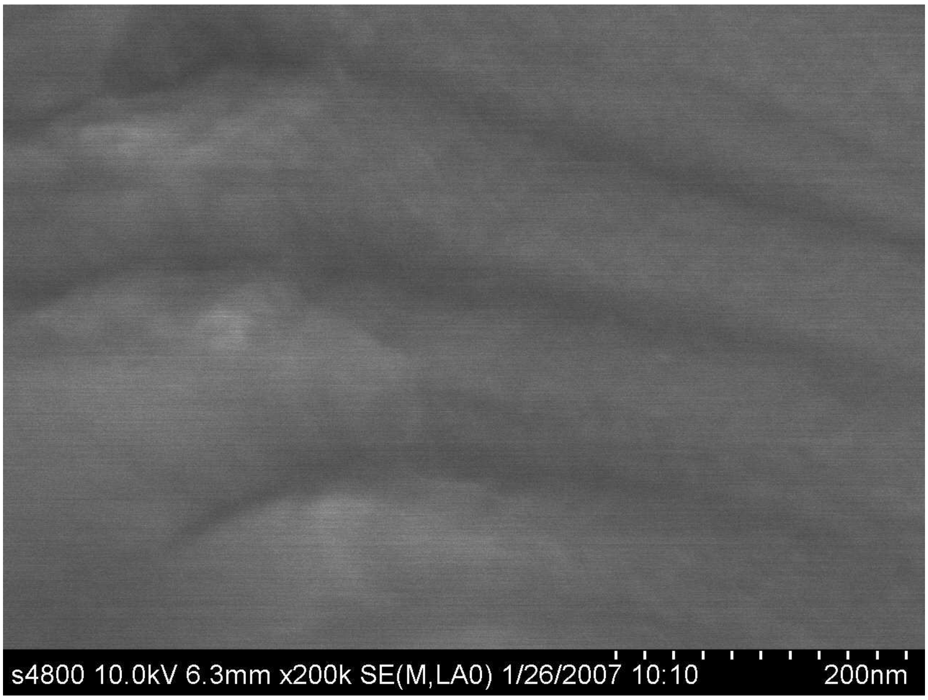

(a) Reference Table 5.1, image ID: str10.

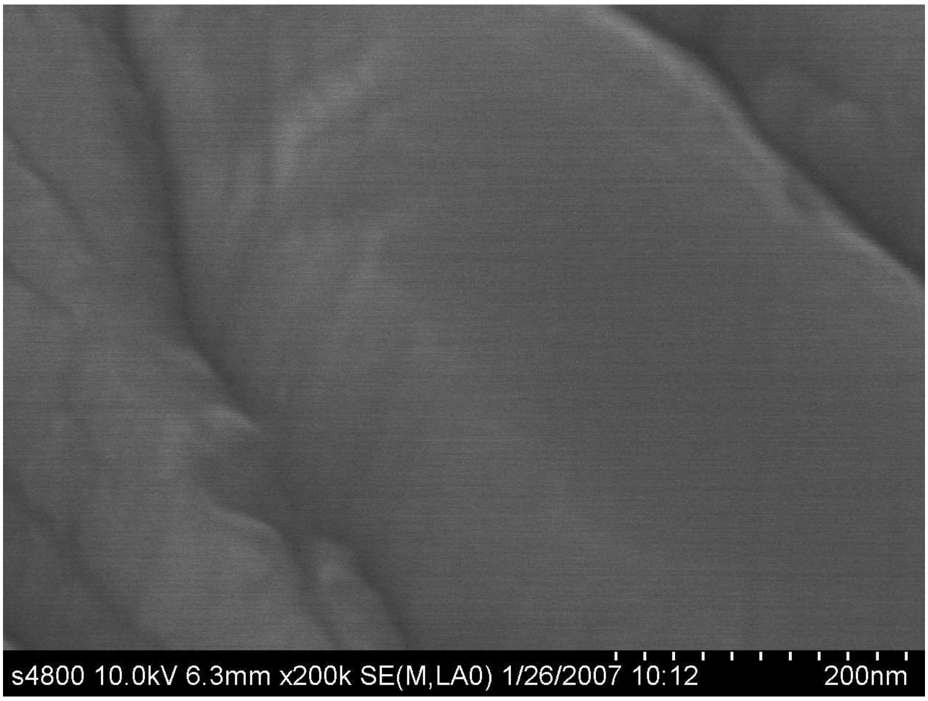

(b) Reference Table 5.1, image ID: str11.

Figure 5.12. Image ID str10 and str11 from image Table 5.1.

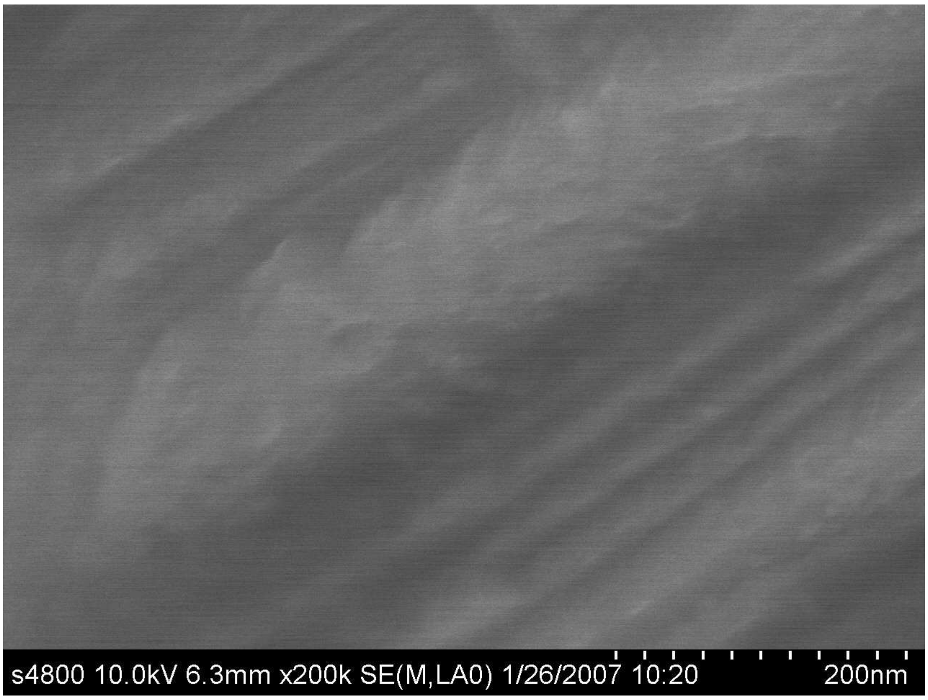

(a) Reference Table 5.1, image ID: str12.

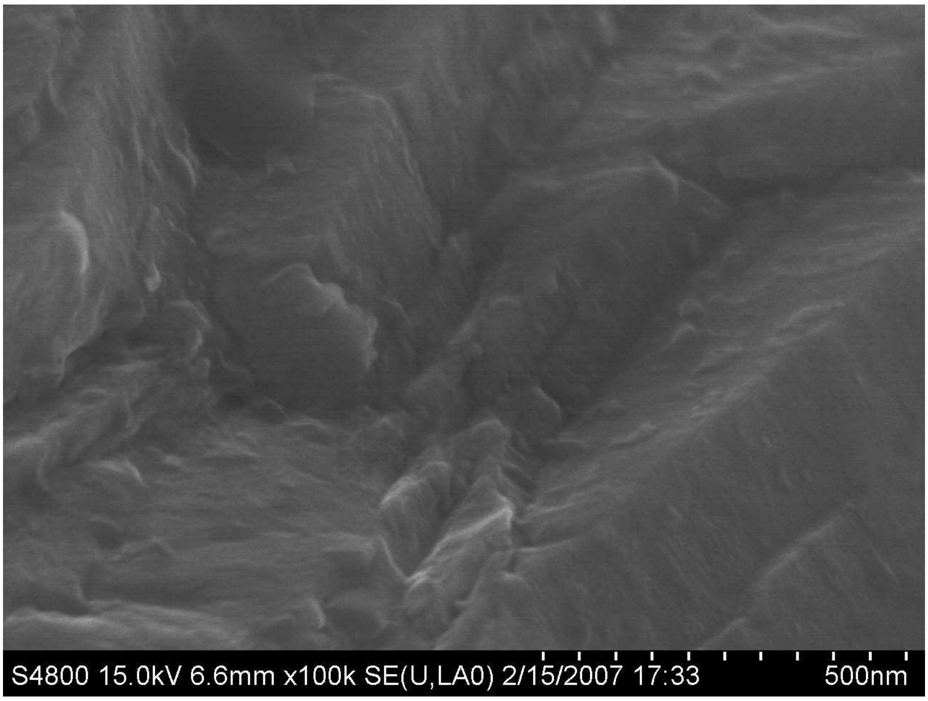

(b) Reference Table 5.1, image ID: str13.

Figure 5.13. Image ID str12 and str13 from image Table 5.1.

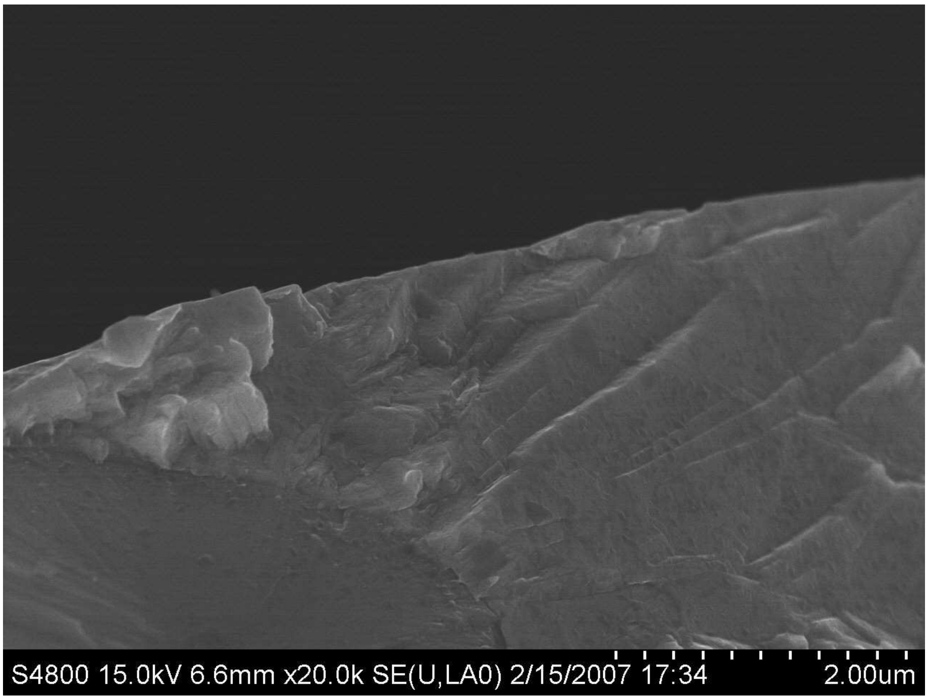

(a) Reference Table 5.1, image ID: str14.

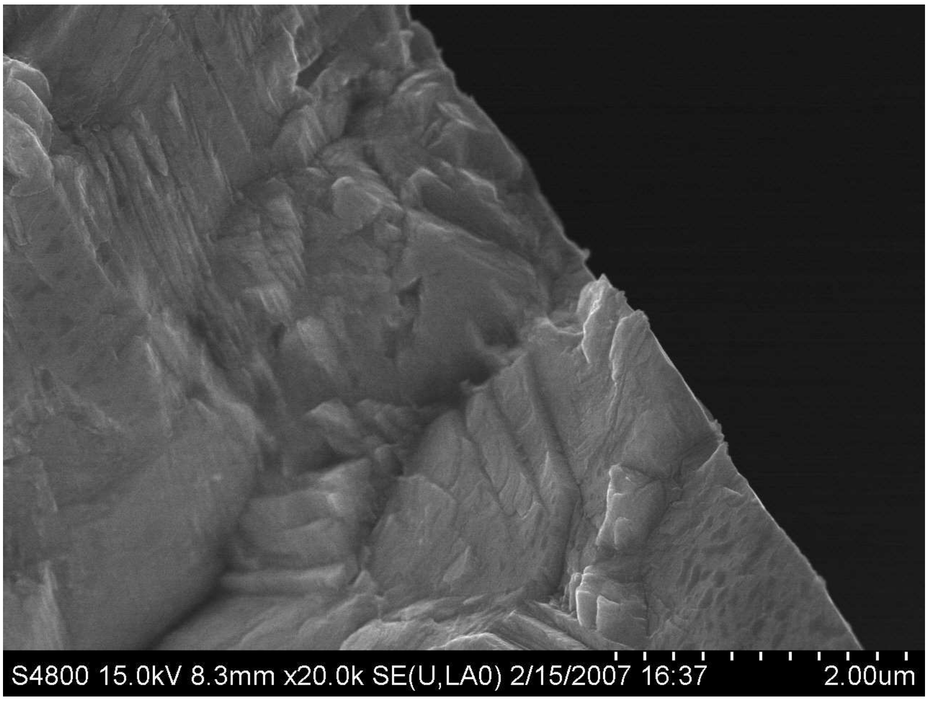

(b) Reference Table 5.1, image ID: str15.

Figure 5.14. Image ID str14 and str15 from image Table 5.1.

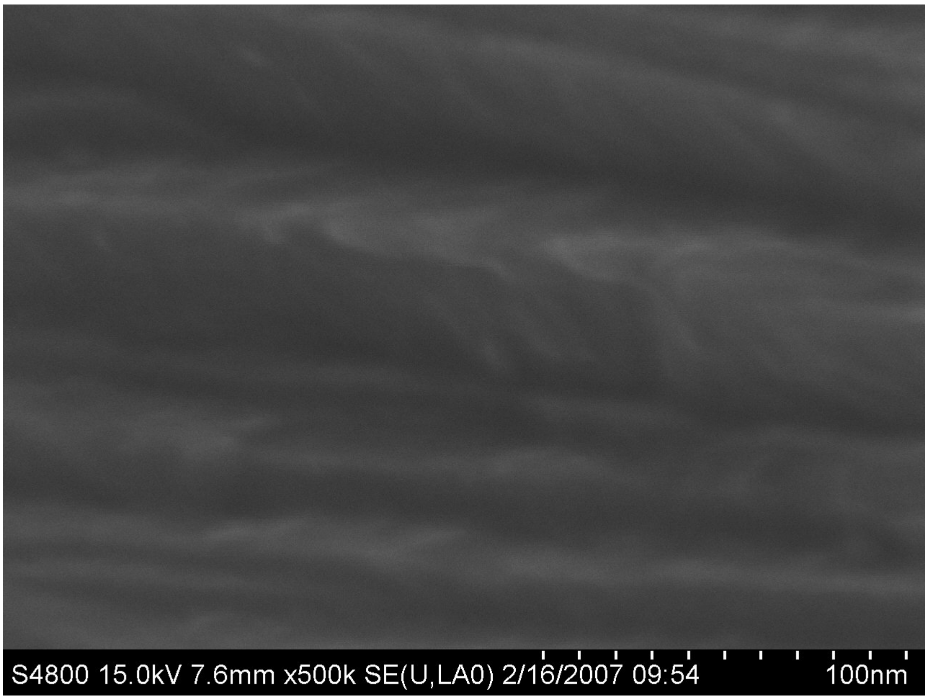

(a) Reference Table 5.1, image ID: str16.

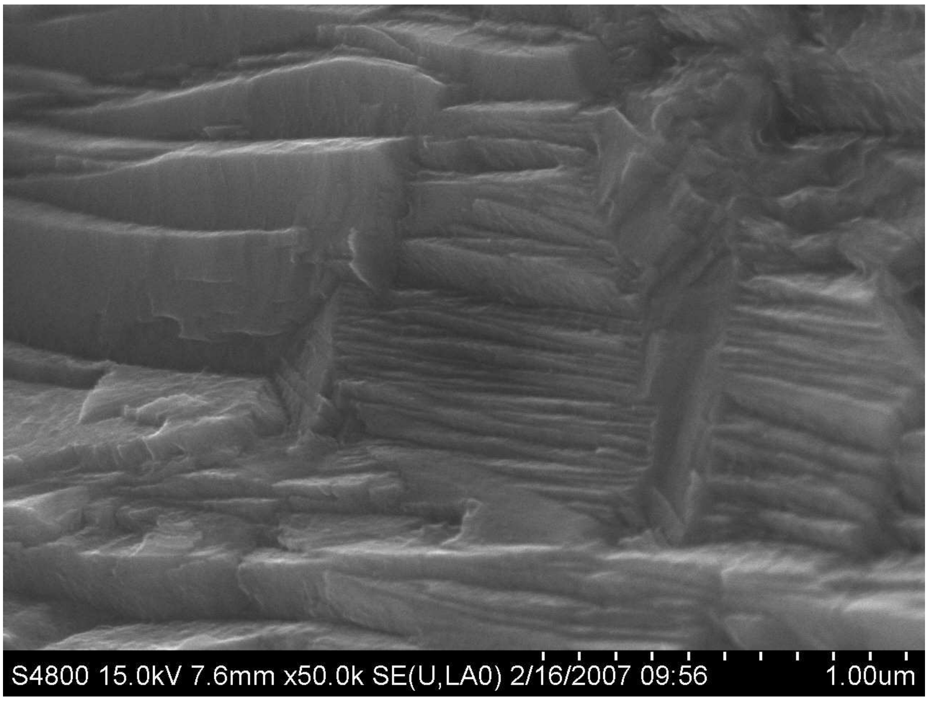

(b) Reference Table 5.1, image ID: str17.

Figure 5.15. Image ID str16 and str17 from image Table 5.1.

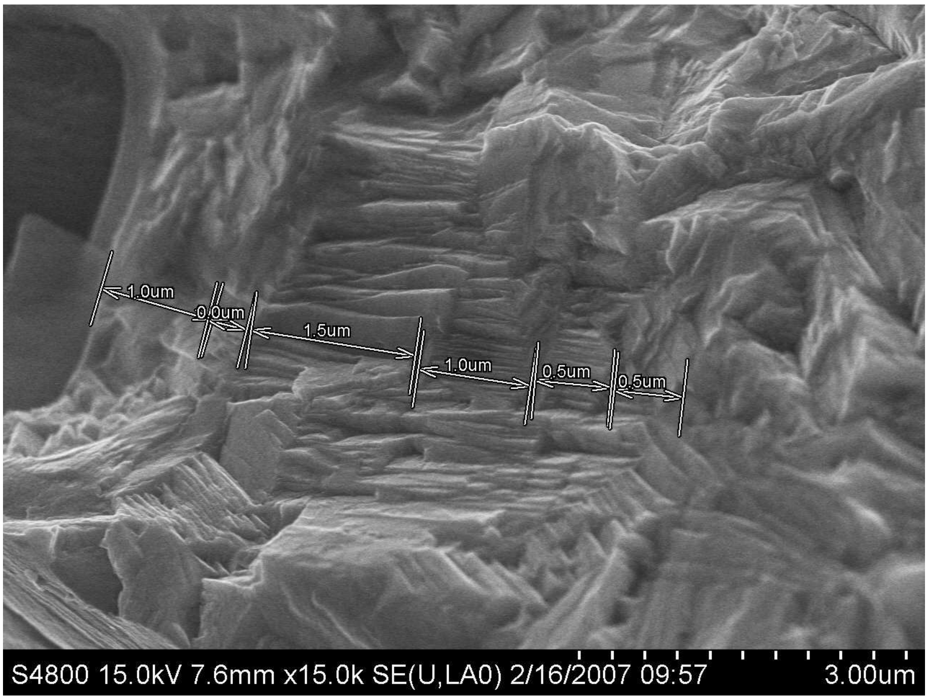

(a) Reference Table 5.1, image ID: str18.

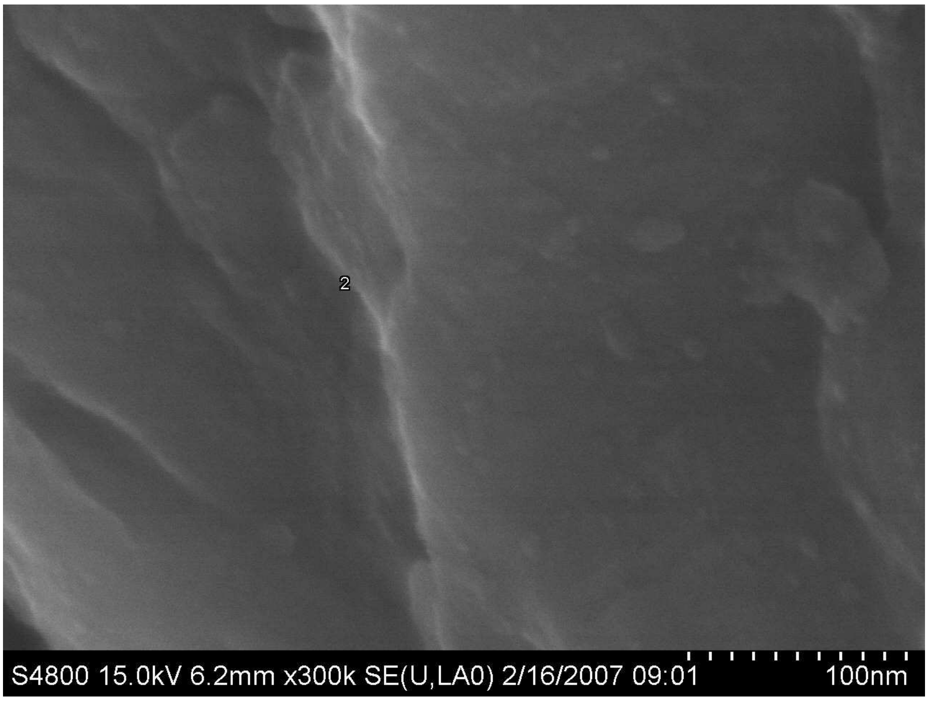

(b) Reference Table 5.1, image ID: str21.

Figure 5.16. Image ID str18 and str21 from image Table 5.1.

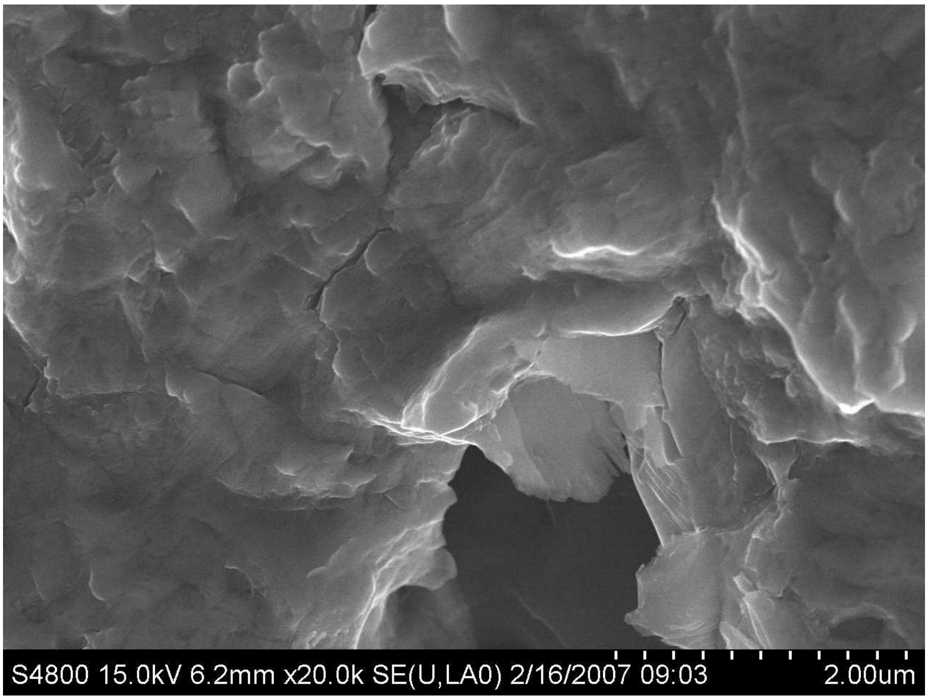

(a) Reference Table 5.1, image ID: str22.

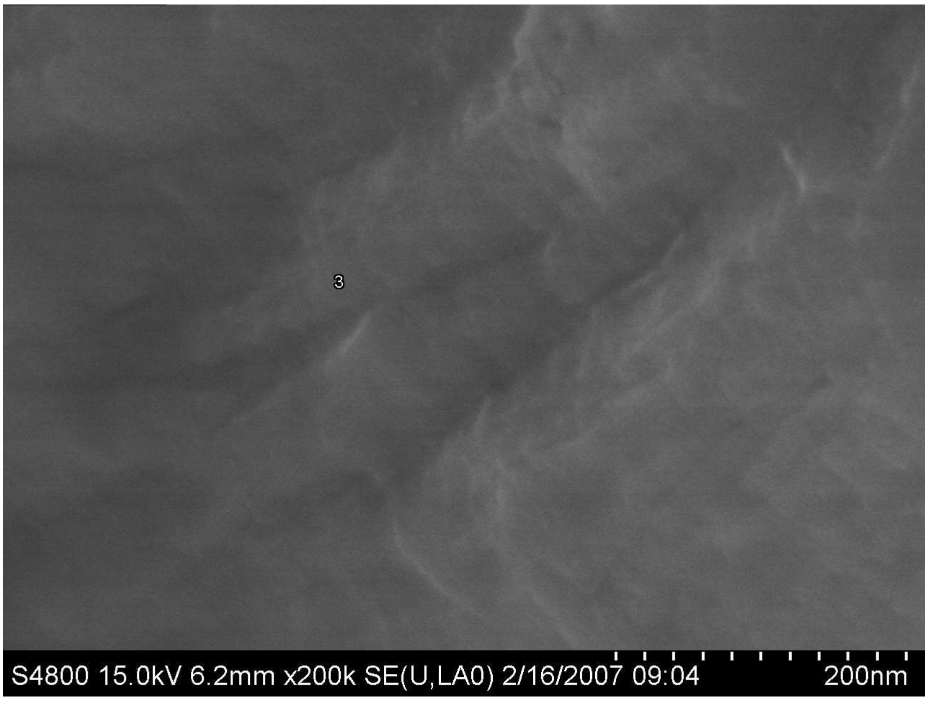

(b) Reference Table 5.1, image ID: str23.

Figure 5.17. Image ID str22 and str23 from image Table 5.1.

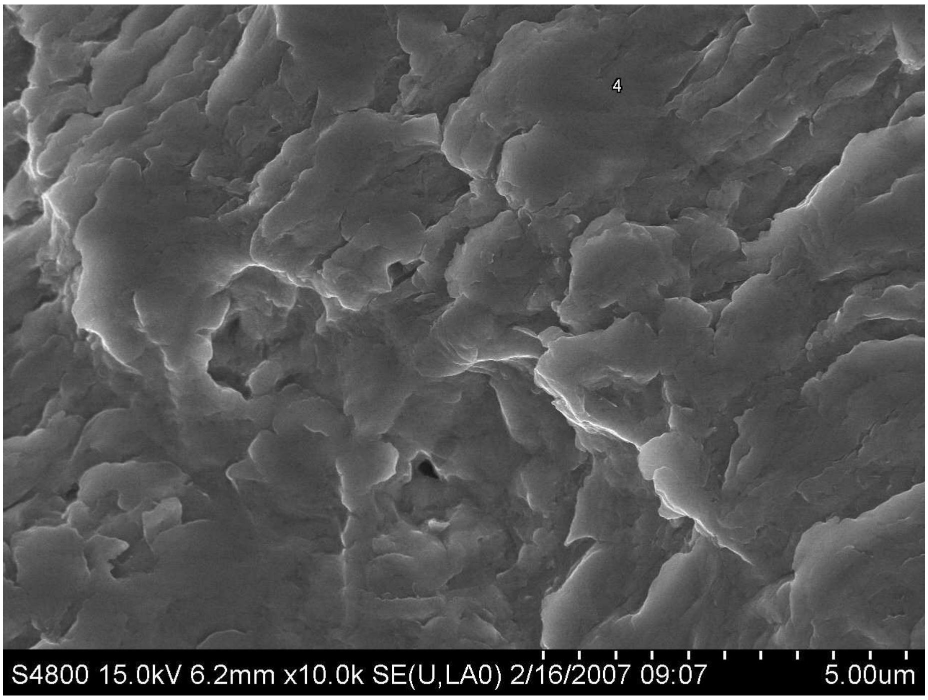

(a) Reference Table 5.1, image ID: str24.

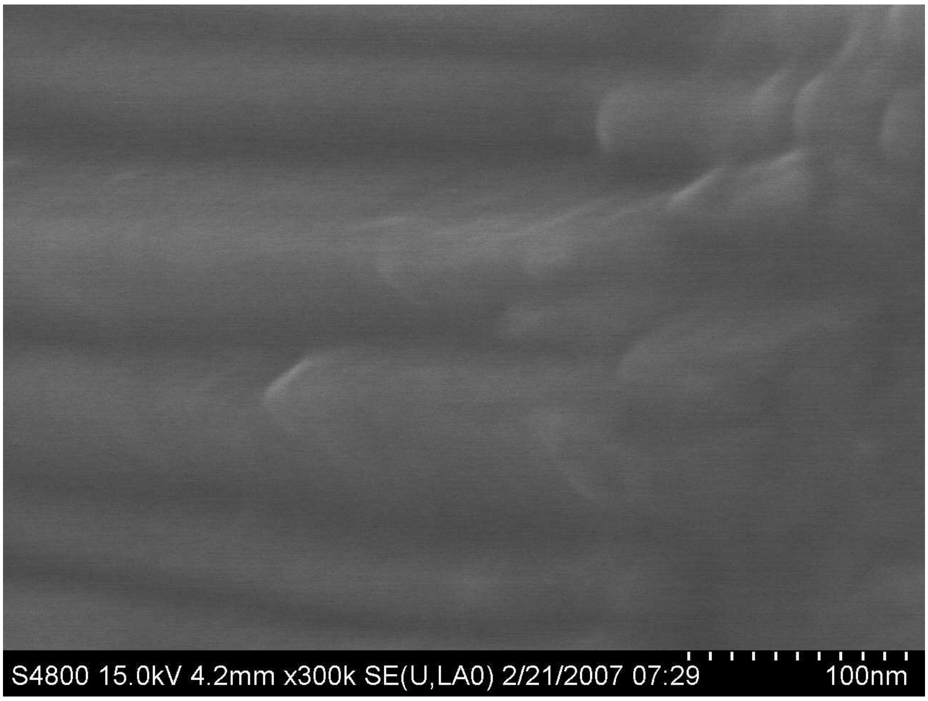

(b) Reference Table 5.1, image ID: str25.

Figure 5.18. Image ID str24 and str25 from image Table 5.1.

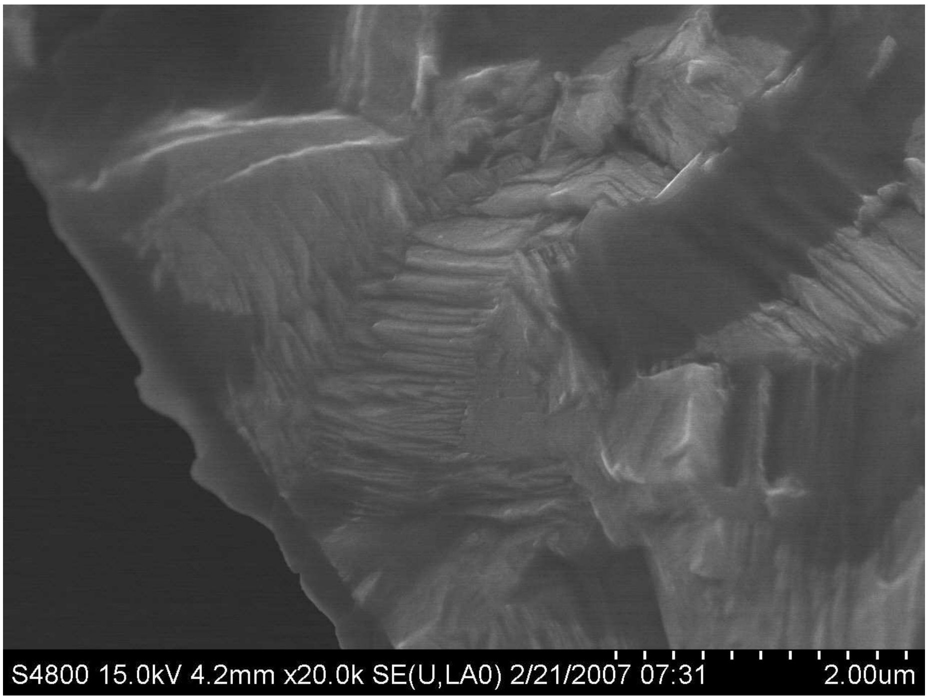

(a) Reference Table 5.1, image ID: str26.

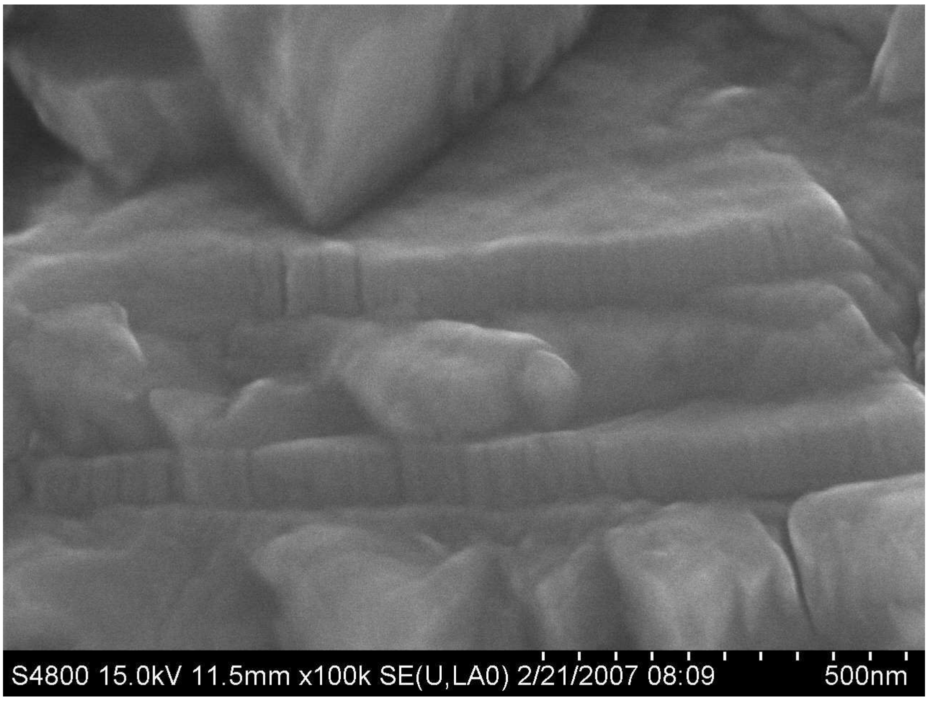

(b) Reference Table 5.1, image ID: str27.

Figure 5.19. Image ID str26 and str27 from image Table 5.1.

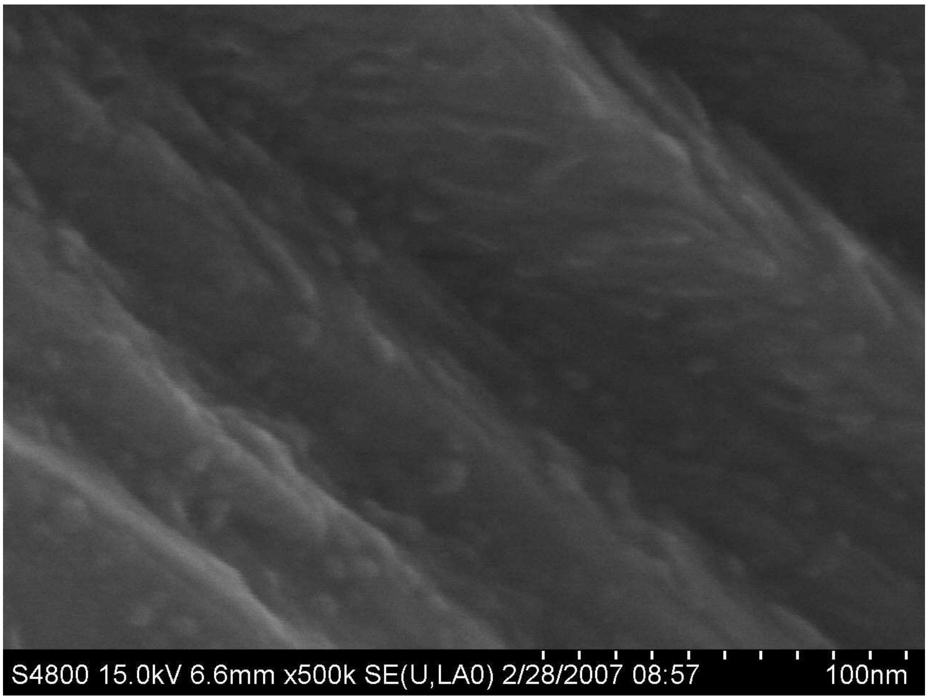

(a) Reference Table 5.1, image ID: str28.

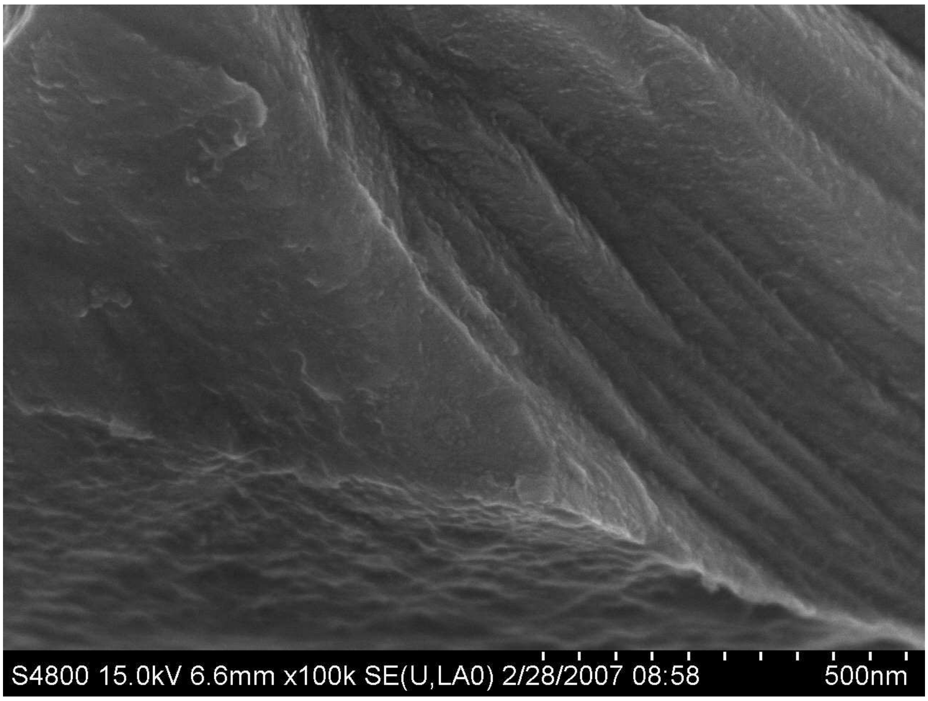

(b) Reference Table 5.1, image ID: str29.

Figure 5.20. Image ID str28 and str29 from image Table 5.1.

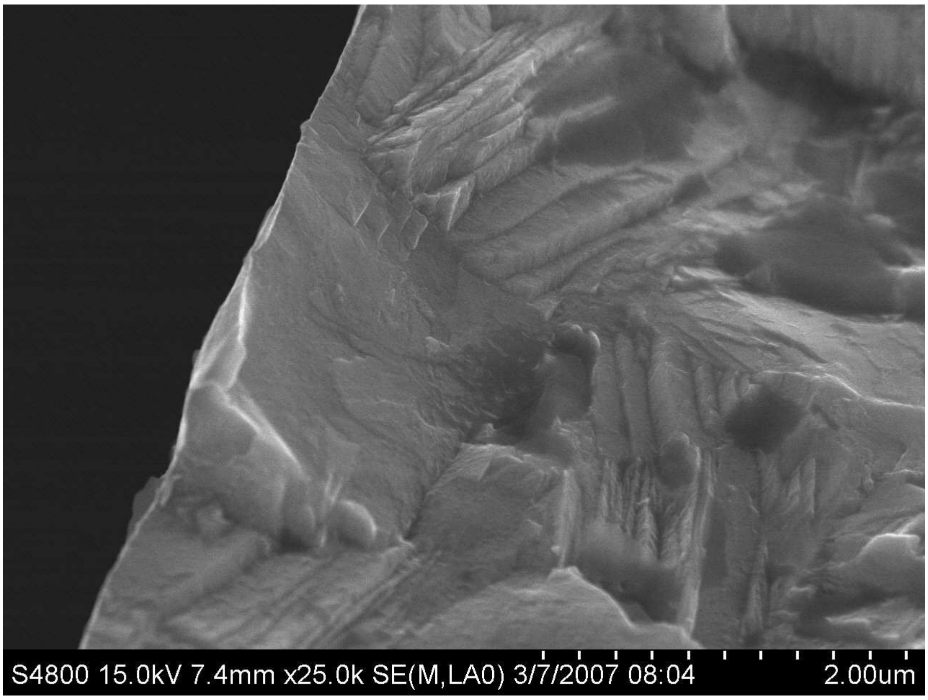

(a) Reference Table 5.1, image ID: str30.

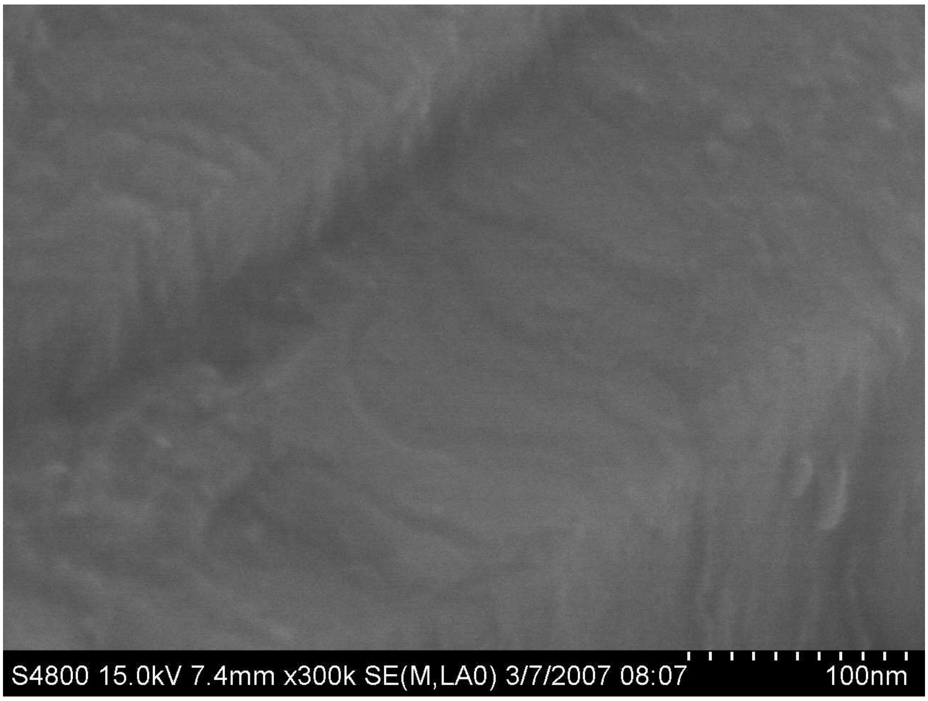

(b) Reference Table 5.1, image ID: str31.

Figure 5.21. Image ID str30 and str31 from image Table 5.1.

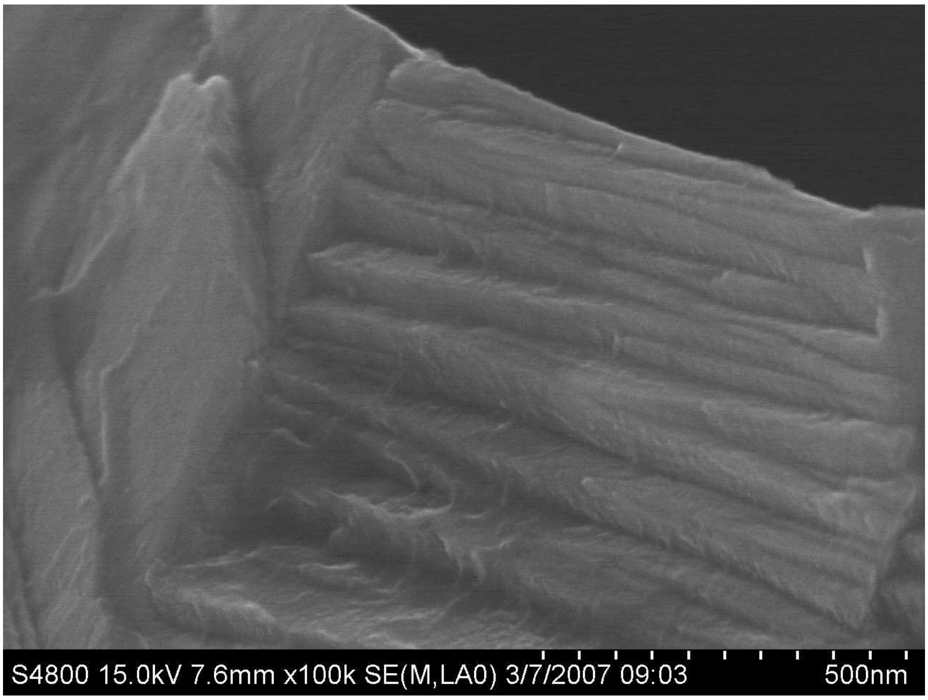

(a) Reference Table 5.1, image ID: str32.

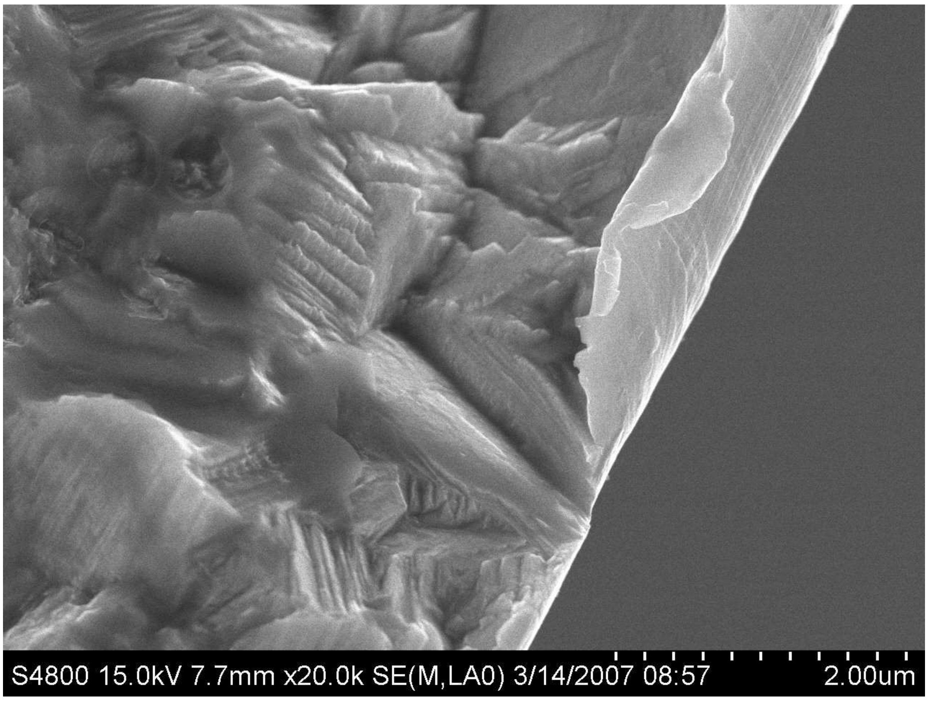

(b) Reference Table 5.1, image ID: str33.

Figure 5.22. Image ID str32 and str33 from image Table 5.1.

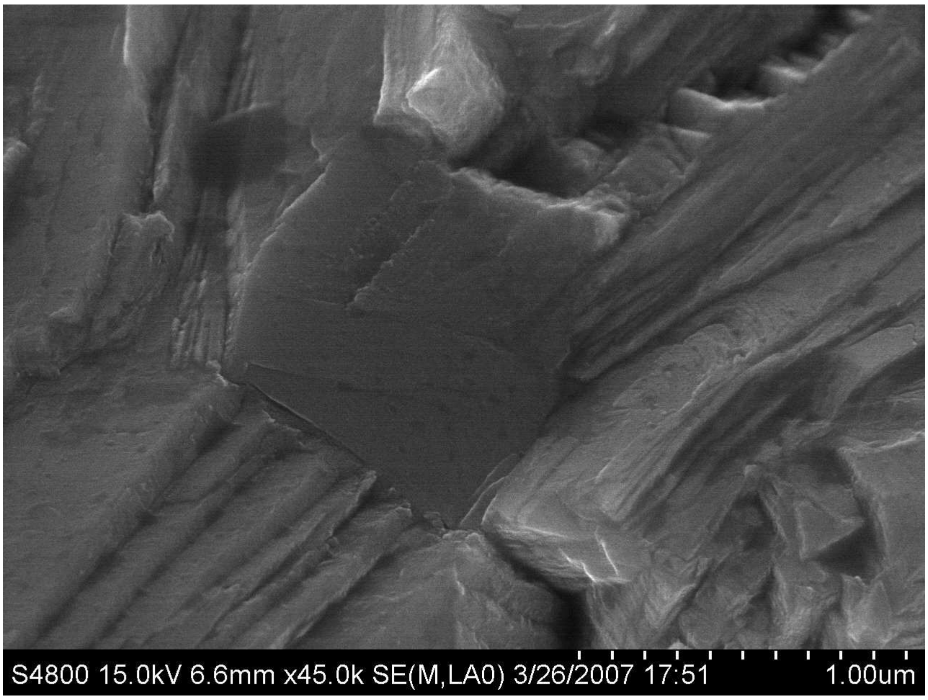

(a) Reference Table 5.1, image ID: str34.

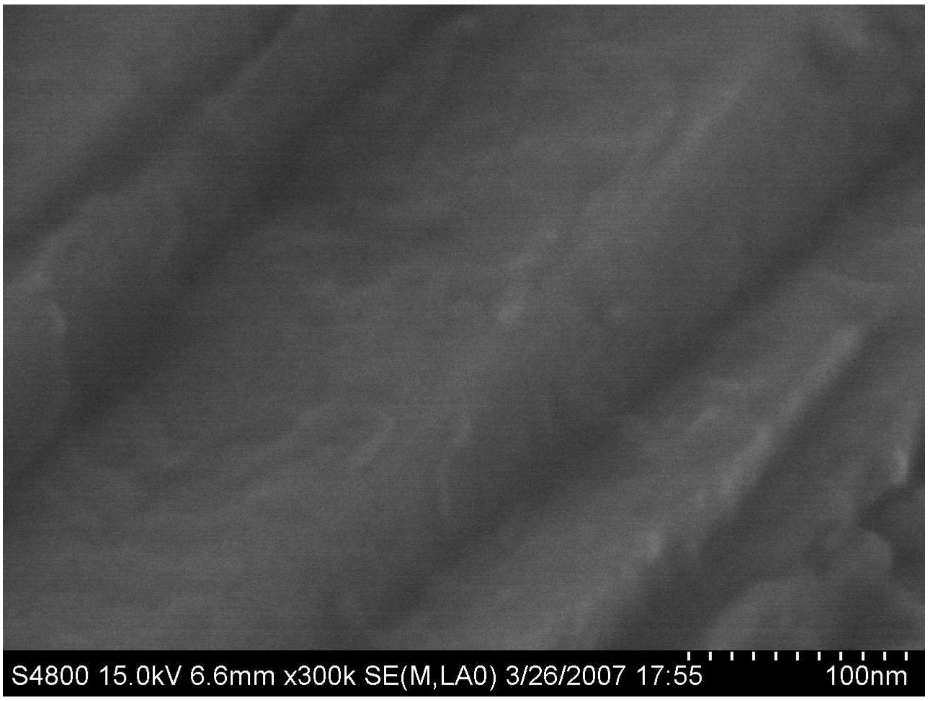

(b) Reference Table 5.1, image ID: str35.

Figure 5.23. Image ID str34 and str35 from image Table 5.1.

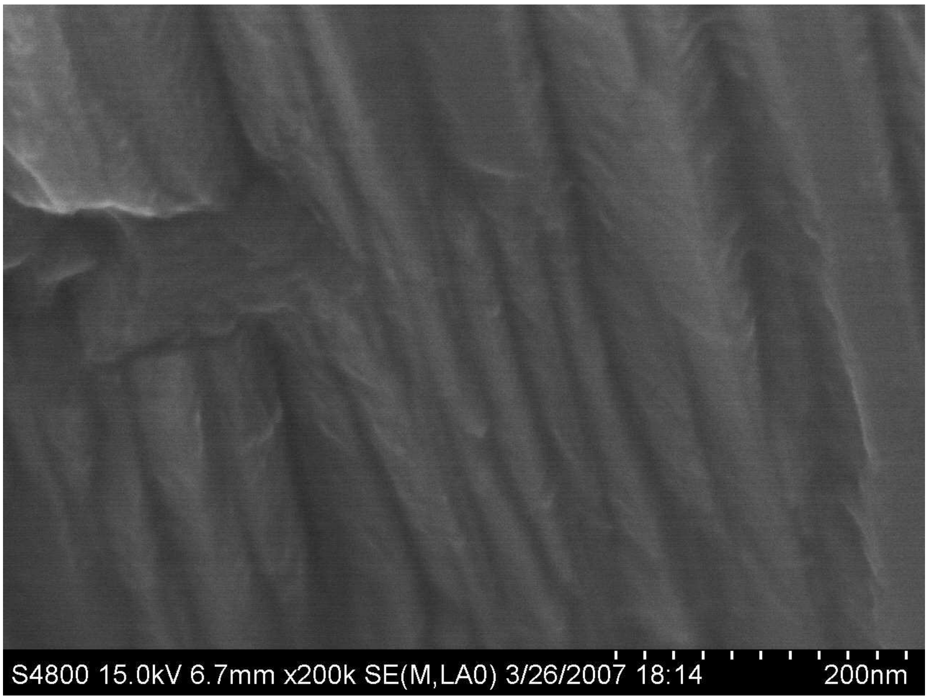

(a) Reference Table 5.1, image ID: str36.

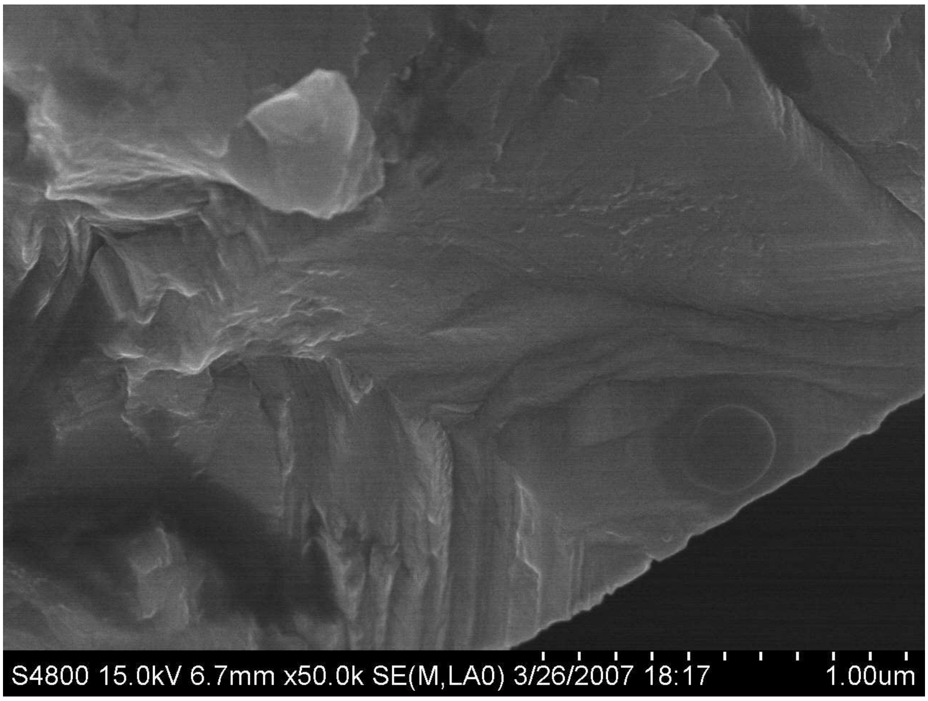

(b) Reference Table 5.1, image ID: str37.

Figure 5.24. Image ID str36 and str37 from image Table 5.1.

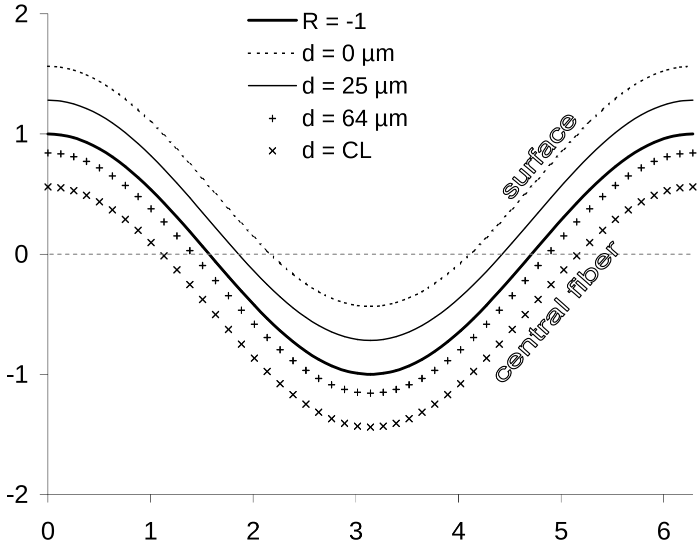

(a) Resultant stress cycle due to non zero mean stresses, at depth, in cold drawn, 1930 MPa, MP35N wire.

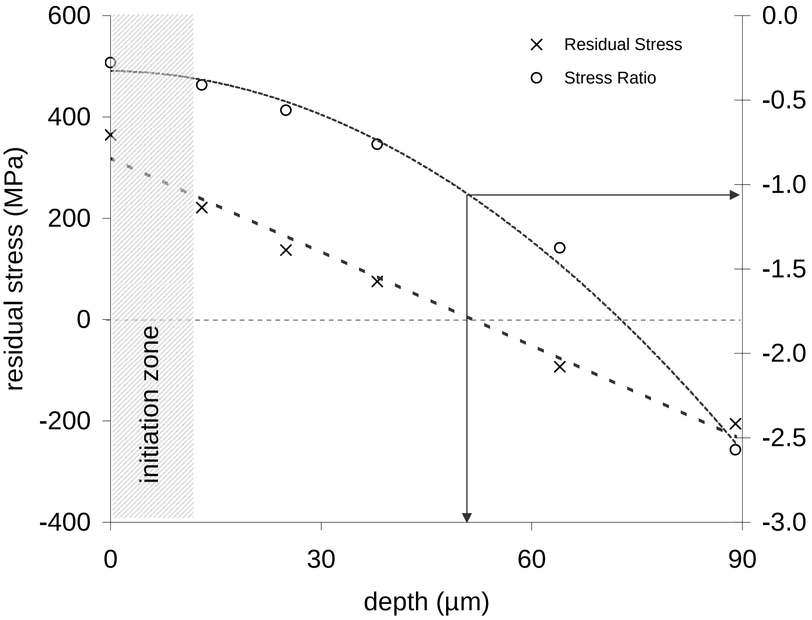

(b) Residual stress profile for 1930 MPa, MP35N wire and associated stress ratio as a function of depth from the wire surface. Note: R = -1 only far from the critical surface initiation zone.

Figure 5.25. Residual stresses and their effect on the stress ratio in cold drawn MP35N wire.

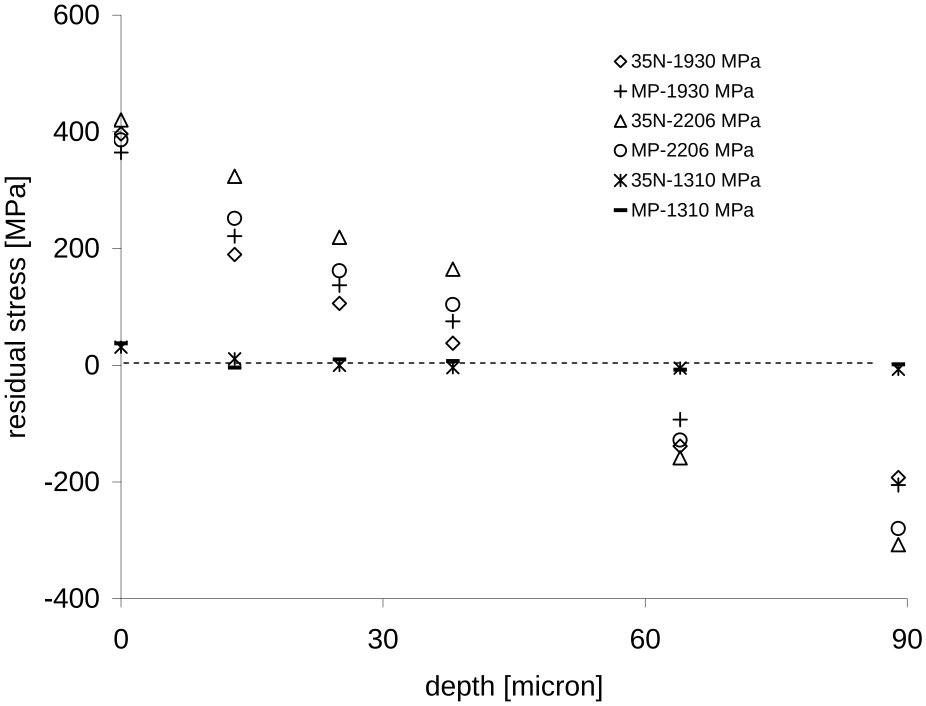

Figure 5.26. Residual stress profile determined by X-ray diffraction analysis in 177 μm MP35N and 35N LT wire. Note the relatively stress free state of the annealed wire and the high residual surface tensile stress in the strain hardened material. Adapted from [18].

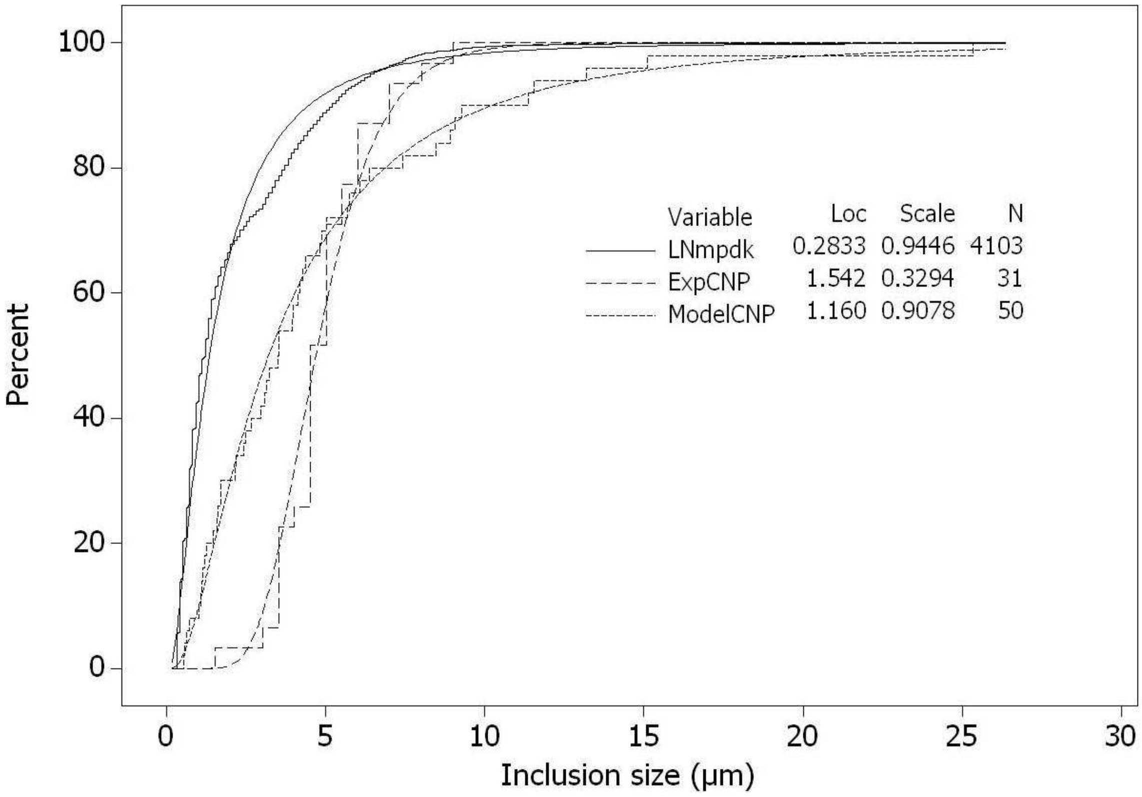

Figure 5.27. CDF of the overall inclusion size distribution found in MP35N wire compared to the model output as well as experimental data for the crack-nucleating size distribution for all configurations tested.

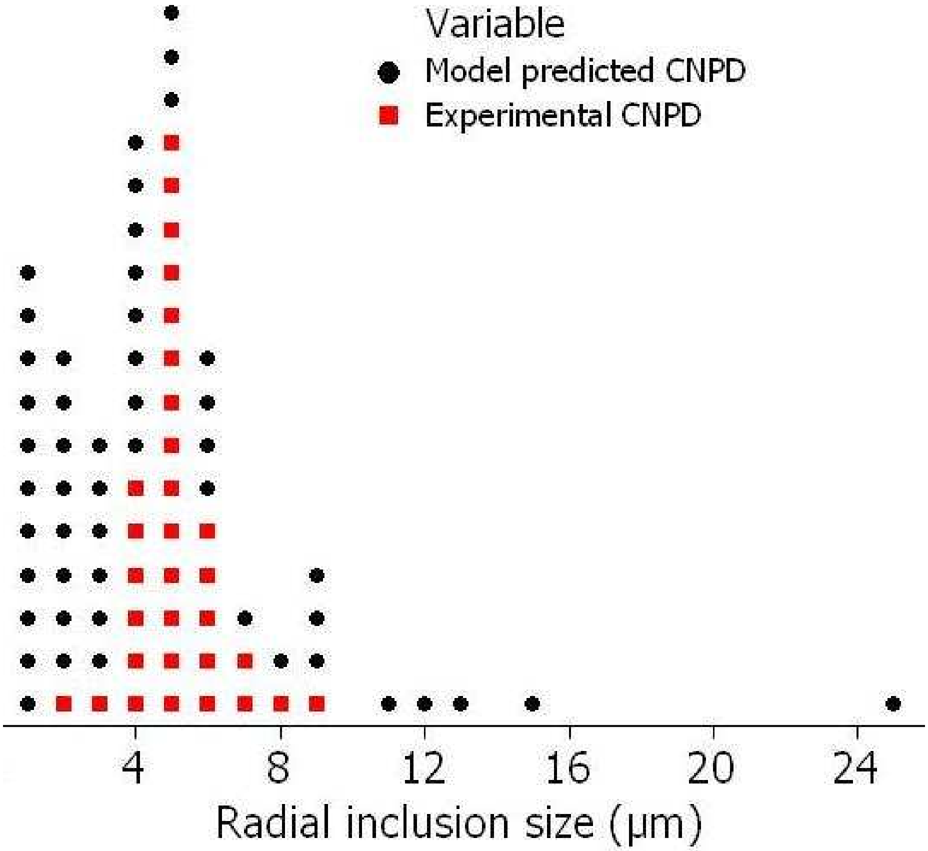

Figure 5.28. Dotplot showing the predicted crack-nucleating particle distribution (CNPD) compared to the experimentally determined CNPD in MP35N wire for all configurations tested.

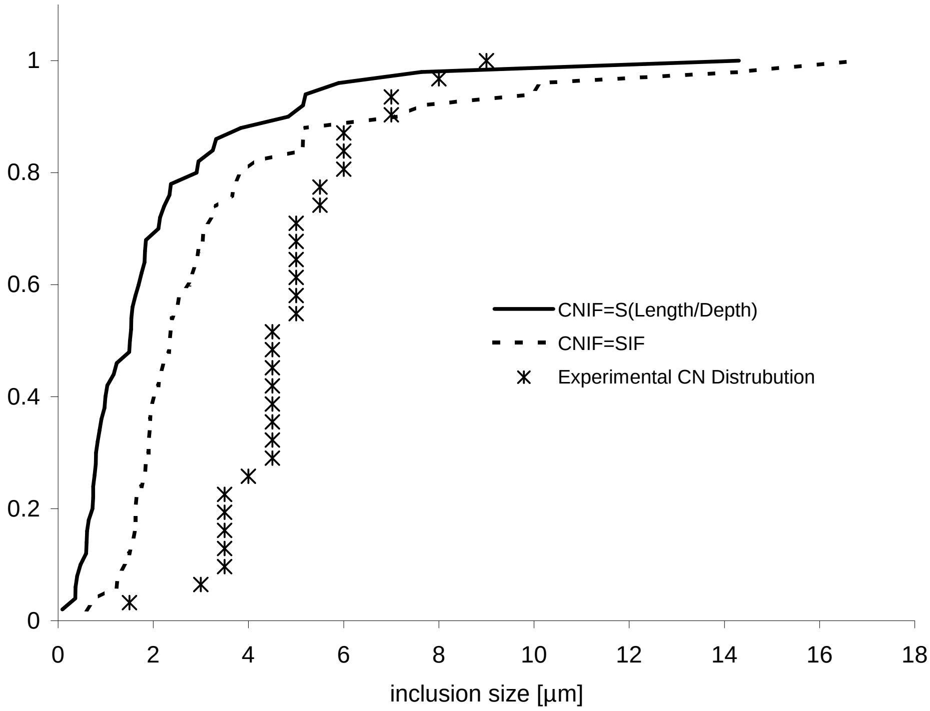

Figure 5.29. A CDF comparison of CNPD model output using Equations (3.5) and (3.4) as well as to experimental data for all test levels in 1930 MPa, 177 μm MP35N wire.

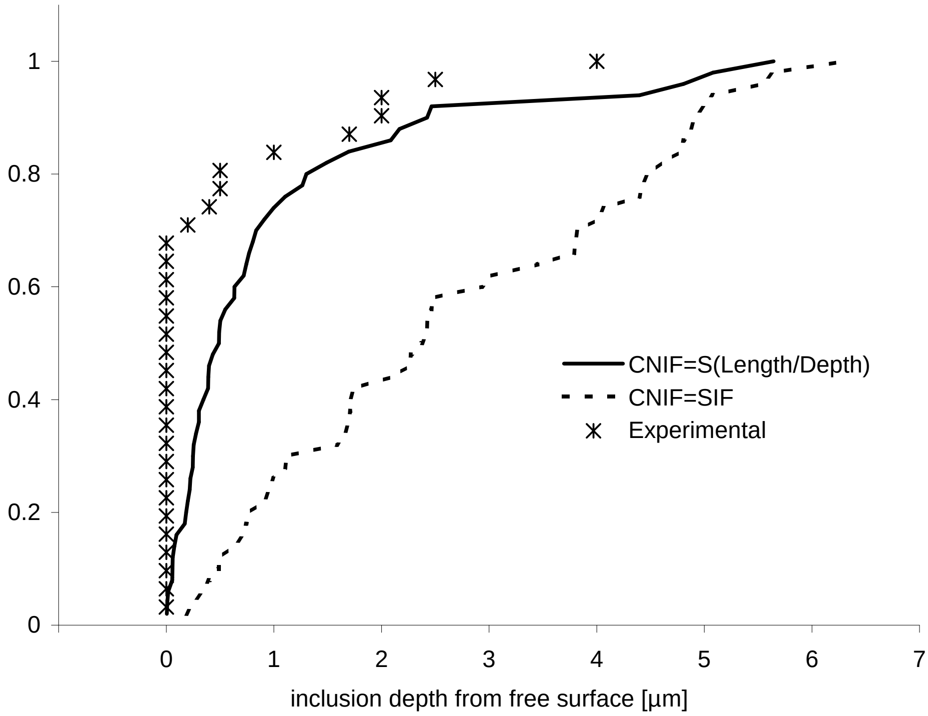

Figure 5.30. A CDF comparison of CNPD depth model output using Equations (3.5) and (3.4) as well as to experimental data for all test levels in 1930 MPa, 177 μm MP35N wire.

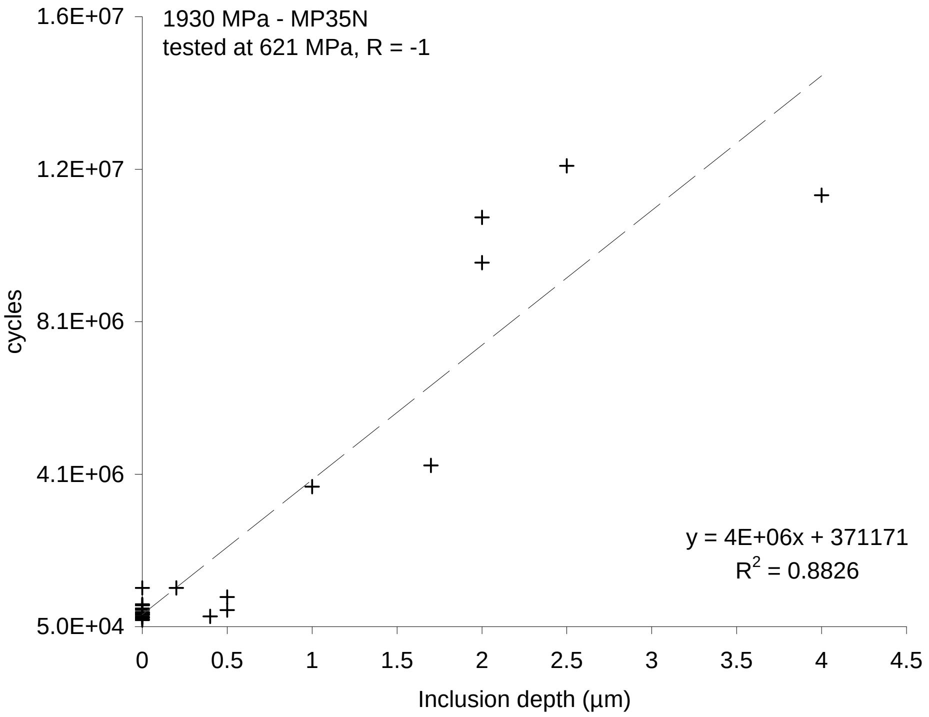

Figure 5.31. Life-inclusion depth correlation for 1930 MPa, 177 μm MP35N tested at 620 MPa, R = -1.

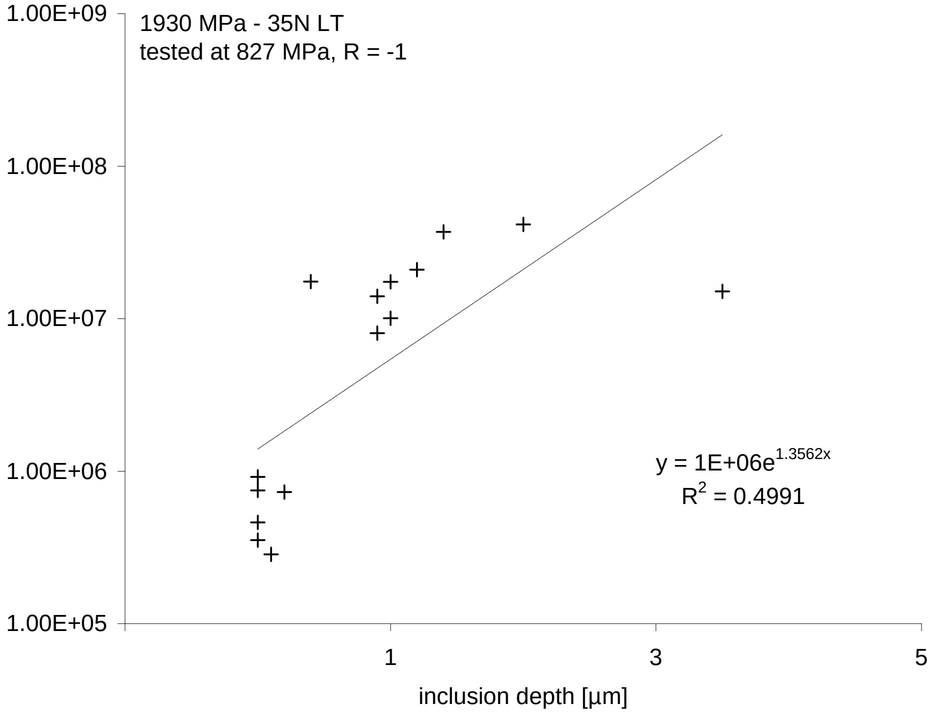

Figure 5.32. Life-inclusion depth correlation for 1930 MPa, 177 μm 35N LT tested at 827 MPa, R = -1.

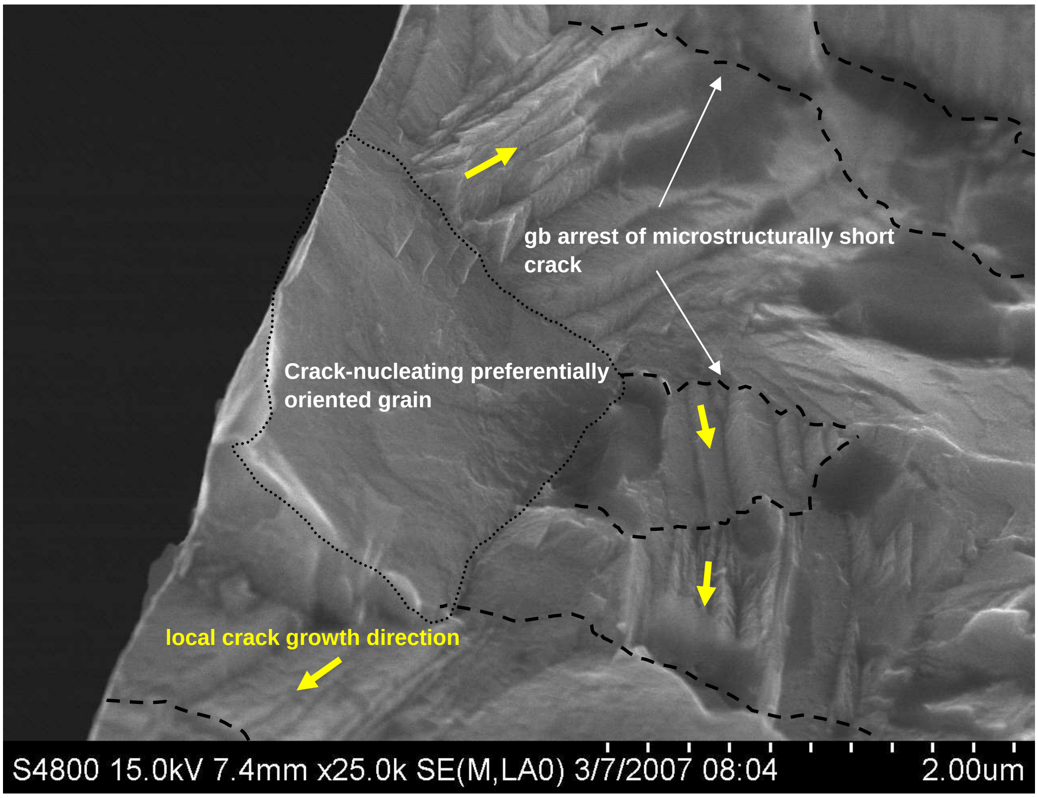

Figure 5.33. Example of incipient crack front arrest at microstructural features in 1930 MPa, 35N LT.

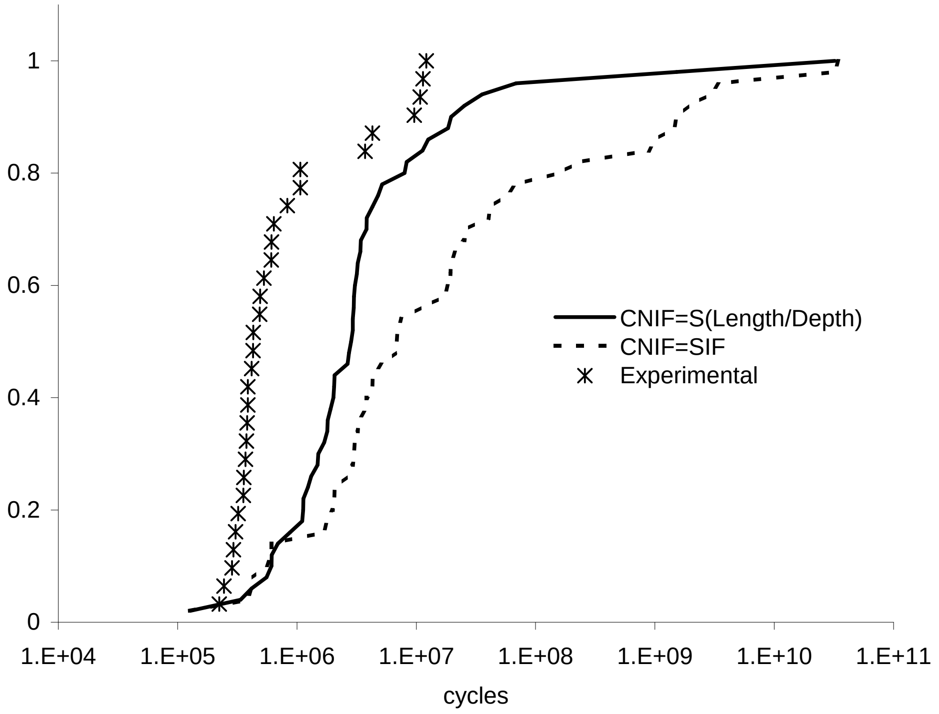

Figure 5.34. A CDF comparison of total fatigue life model output using Equations (3.5) and (3.4) as well as to experimental data for the 620 MPa test level in 1930 MPa, 177 μm MP35N wire.

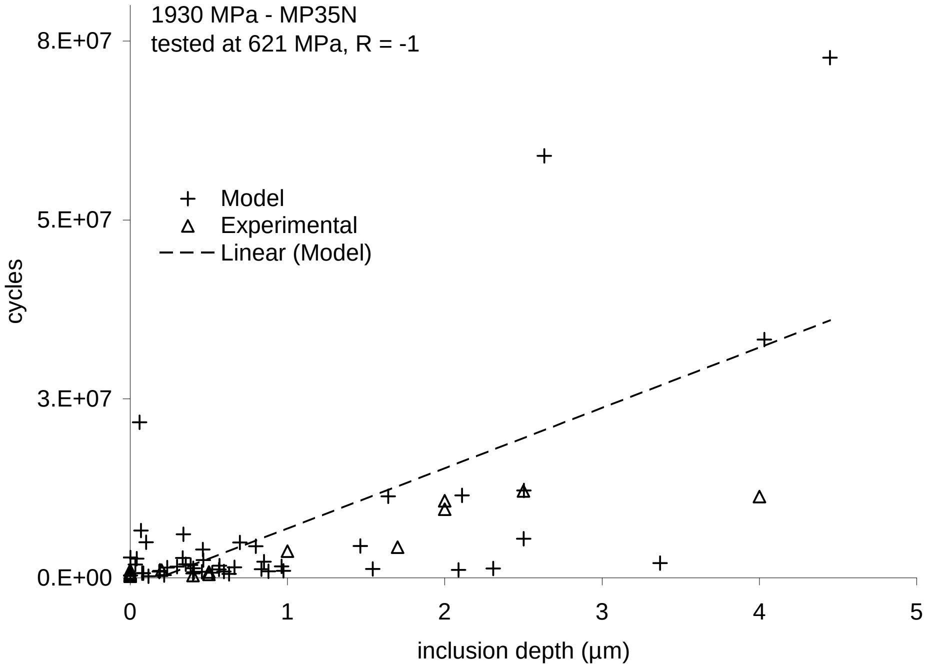

Figure 5.35. Similarity in the life-inclusion depth relationship for model output and experimental data for 1930 MPa, 177 μm MP35N tested at 620 MPa, R=-1.

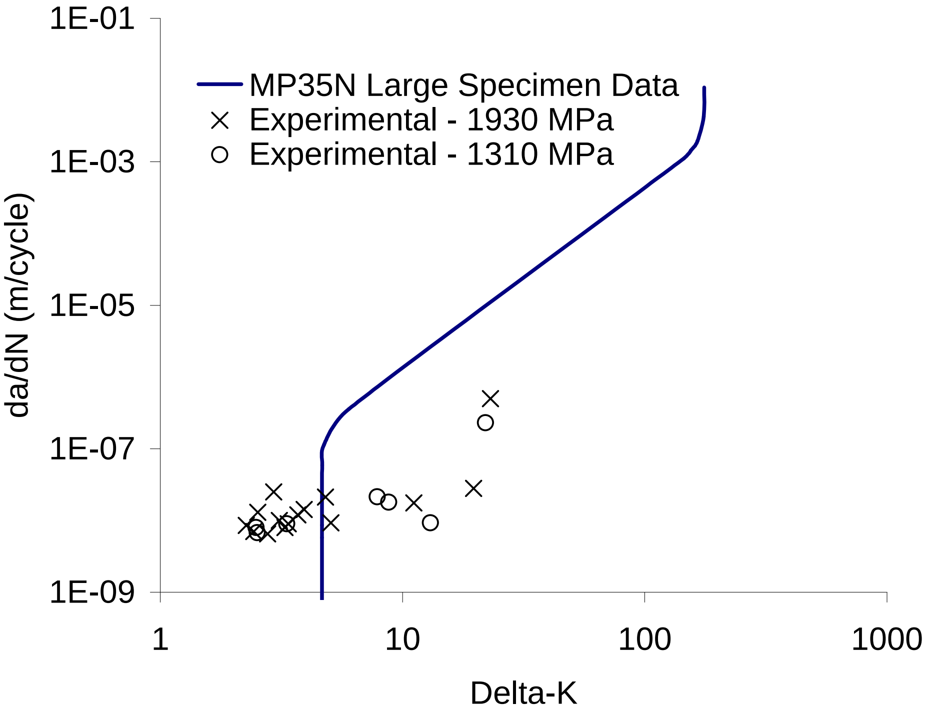

Figure 5.36. Experimentally observed $\frac{da}{dN}$ vs. ΔK inferred from striation measurements compared to large specimen data adapted from ref [89].

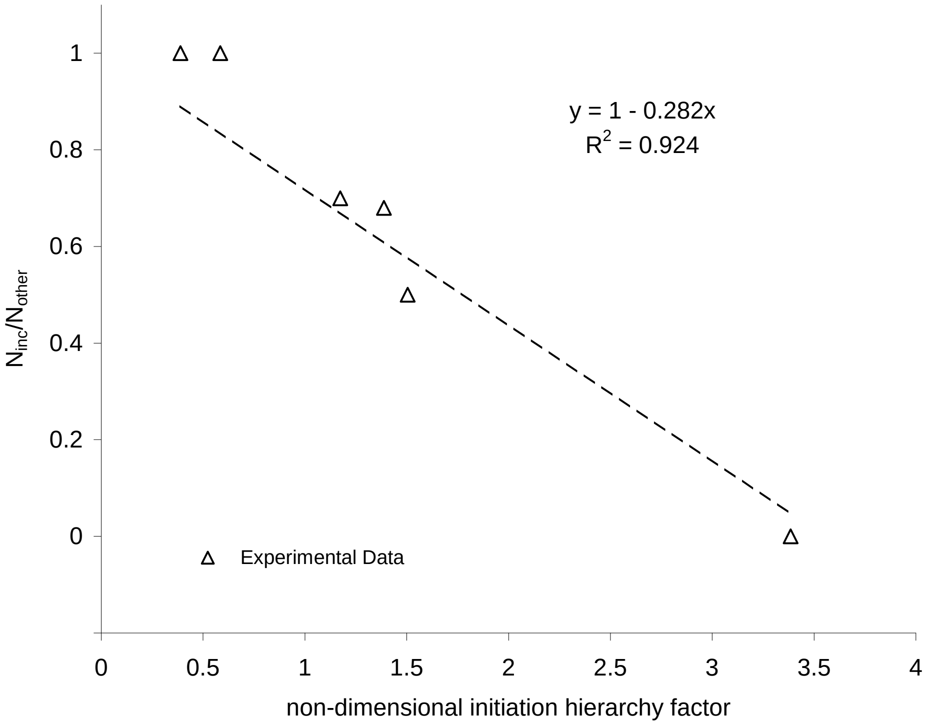

Figure 5.37. Experimentally observed IHF correlation.

X denotes initiation, arrows represent local crack growth direction at surface.

Figure 5.38. SEM collage: incipient fatigue crack formation at a microstructural feature other than a visible inclusion in 35N LT at the 1310 MPa strength level (GS 3 μm).

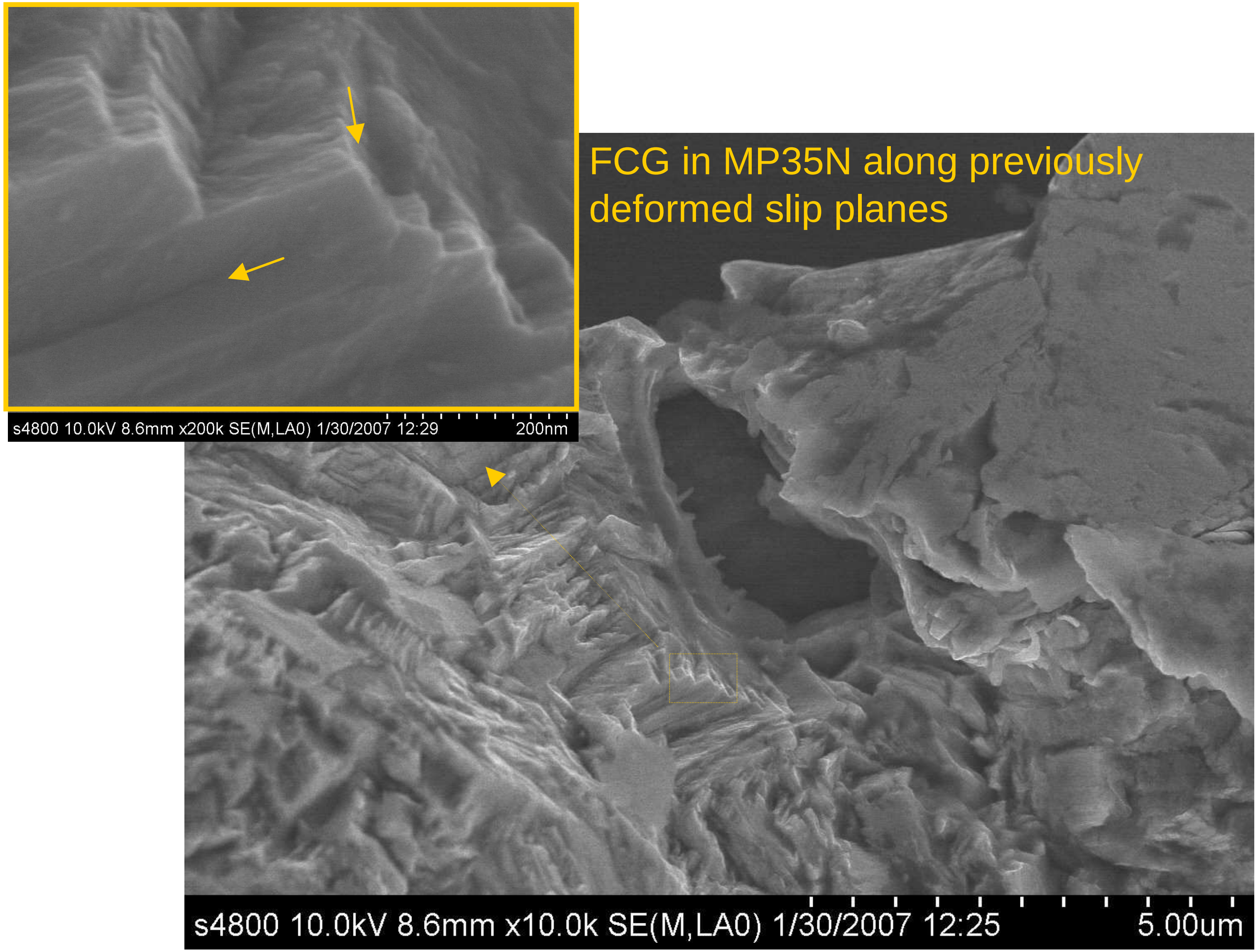

Figure 5.39. FCG growth along previously deformed slip planes in 1930 MPa, MP35N wire tested at 930 MPa.

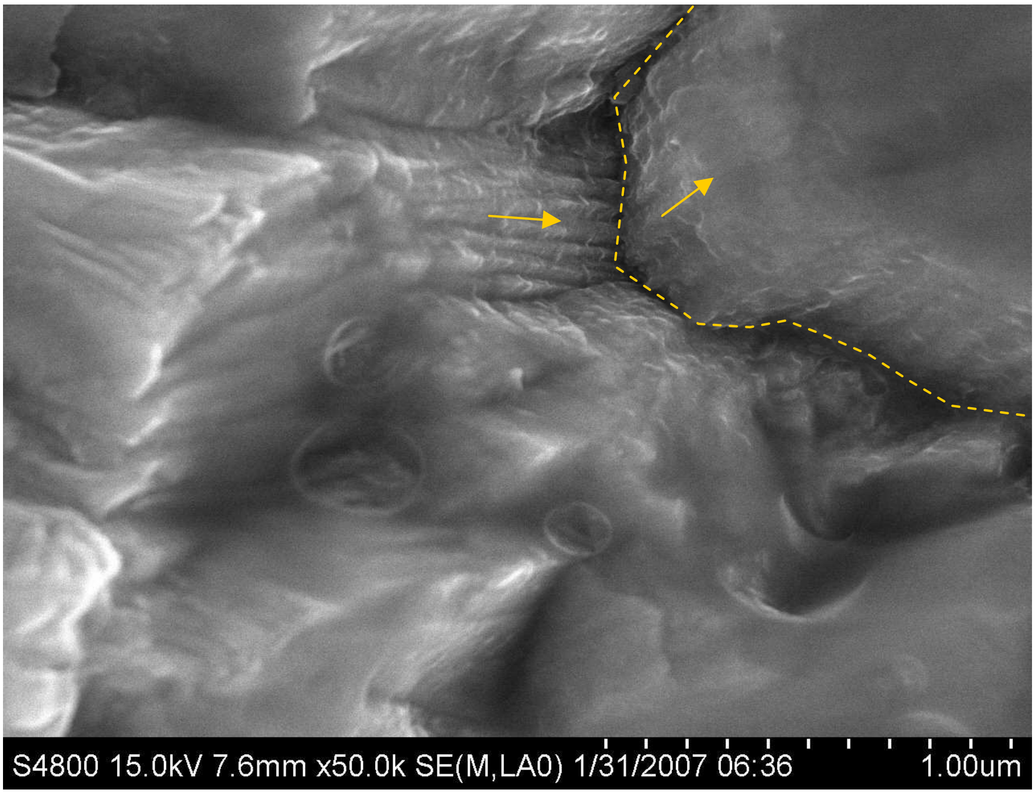

Figure 5.40. Example of GB influence on local FCG direction 1930 MPa, MP35N.

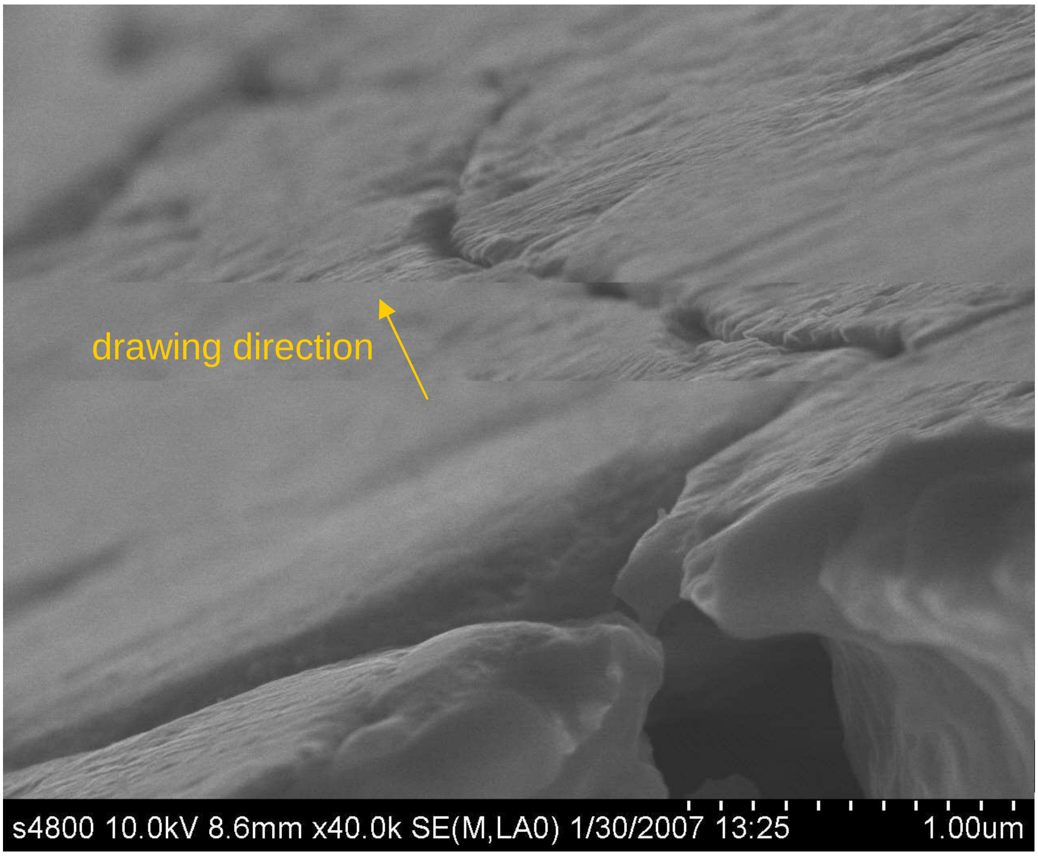

Figure 5.41. SEM collage: a crack-initiating inclusion stringer surface feature in MP35N wire.

6. CONCLUSIONS AND RECOMMENDATIONS

6.1 Conclusions

The goals of this research were to elucidate important factors affecting fatigue initiation life, develop a hierarchical lifetime model taking the same into account, verify preliminary modeling results by comparison to experimental data and attempt to sort crack-nucleating defect states from overall statistical background noise. The realized gains in pursuing these objectives may be summarized as follows:

- Multiple material configurations in 35N LT (clean version of the ASTM F562 alloy system) and MP35N (standard version of ASTM F562) were tested to failure using RBT and successfully preserved for further fractographic analysis.
- SEM and SEM/FIB methods were used to characterize microstructural parameters affecting fatigue life in fine 35N LT and MP35N wire.
- Inclusions were found to have only a marginal affect on total life in systems possessing high ductility and/or grain sizes on par with the inclusion size distribution. For example, in the equiax-grained 2.5 μm GS material, MP35N and 35N LT performed equivalently in both total life and variability.
- A crack-nucleating intensity factor (CNIF) was developed and used to successfully sort important defects in nucleation from statistical background noise.
- An initiation hierarchy function (IHF) was proposed based on non-dimensional factors to be used in predicting the prevalence rate of inclusion based fracture and was successfully fit to experimental data.

- The crack-nucleating defect distribution was well predicted by the CNIF sorting algorithm.
- Inclusion depth from the wire surface was found to be more important in life determination than inclusion size.
- Cracks were found to grow at low stress intensity levels, below the threshold found in most literature for this alloy. This effect may be due to surface tensile residual stresses, intragranular variation of residual stresses and the resultant shift in the effective stress ratio.

6.2 Recommendations

The data presented here but scratches the surface of what needs to be done in regard to fatigue life research in the realm of fine medical wire. In order to constructively proceed in the future, there are several facets of the research that deserve further exploration.

Additional work is needed to understand the effects of residual stresses on the initiation fatigue life of wire materials. Residual stresses are known to substantially impact fatigue crack growth life. Their influence on initiation life, however, has not been studied significantly in the literature - particularly for fine wire systems. Similarly, further knowledge is needed on the effects of texture distributions both on local residual stress states and on the overall fatigue damage process.

A crack-nucleating intensity factor (CNIF) was developed and used to successfully sort important defects in nucleation from background noise. While this factor worked well for the present case, additional research should be conducted to determine its applicability in other situations. A more general form and accompanying theoretical background may allow use in other industries than medical technology.

More research to study FCG at the near initiation level would help in the understanding of early crack-arrest lifetime contribution and may help improve modeling techniques. In addition to SEM methods, transmission electron microscopy (TEM) to examine near-defect dislocation activity may also aid in understanding why certain defects cause failure.

Further research should be done to explore initiation hierarchy in fine wire systems. The significance of the IHF, if it can be further validated, lies in its ability to prescreen a material based on statistical defect distributions. This would be the first step in the life modeling sequence, to determine *a priori*, the expected ratio of fractures that would occur due to relatively non-compliant material phases such as inclusion particles. The algorithm would then use this fraction of data from the respective initiation models together with a CNIF defect selection algorithm to generate total lifetime variability information pertinent to the system in question. Such a model could generate guidance in determining ideal grain sizes to limit the incidence of particle driven failure or to determine microstructural cleanliness requirements.

The overall impact of such a holistic model, encompassing everything from raw material to wire processing induced residual stresses, to the finish device, would be extremely useful in designing tomorrow's implantable medical systems against premature failure.

7. OTHER EXPERIMENTS

7.1 Influence of Small Grain Size

Changes in deformation behavior as a function of grain size (GS) have been documented for metallic, polycrystalline systems in other work [90]. In addition to the grain sizes explicitly defined in this research, another finer structure was created and tested for endurance at 100 million cycles using rotary beam analysis. The goal of this experiment was to examine the lower limit of a possible exponential relation between life and GS. While additional research is needed on this subject, the preliminary results are shown in Figure 7.1.

7.2 High Fatigue, High Ductility Medical Wire

The present experiment provides a processing method that is applicable to a variety of medical grade wire materials. The process output is a wire material possessing a relatively high degree of ductility (as measured in a uniaxial, monotonic tension test) and resistance to high cycle fatigue failure.

The process was specifically designed to limit fatigue damage by reducing the propensity for irreversible slip during high cycle, cyclic loading. A specific mechanism used to effect reduced damage was a process-resultant GS that is significantly below conventionally processed medical wire materials. Otherwise stated, the materials possess a grain size that is much smaller than conventional materials, which imparts excellent high cycle fatigue damage resistance and relatively high ductility and strength. Whereas conventional medical wire materials possess a GS on the order of 500 to 50,000 nm, the present processing results in a GS of about 0 to 500 nm.

Energetic considerations make slip activation less favorable in this *nanograin* material than in conventional materials.

A study is currently underway utilizing this process applied to the ASTM F562, 35Co-35Ni-20Cr-10Mo alloy system. In this study, a GS was achieved in the alloy system in the range of about 30 to 250 nm. Fatigue testing was carried out on this material to determine its load stress capability at 100 million cycles, at an applied extrinsic stress ratio of R = -1. The fatigue alternating stress, at a life exceeding 100 million cycles, was found to be greater than or equal to 150 ksi. In other studies, fatigue stress limits for this material in a high ductility form, have not approached this value.

Mechanical tension testing of this material demonstrated an axial strain to rupture of greater than 10% of the original test gage length. The author has not found a single instance of a medical grade fine wire, where the diameter is greater than zero and less than one millimeter, possessing combined characteristics comprising: (1) A fatigue life exceeding 100 million cycles at an alternating stress level equal to or greater than 150 ksi or 60% of the material's ultimate tensile strength and, (2) An axial strain to rupture exceeding 10% of the original gage length of a monotonic, uniaxial tension test. These characteristics are, therefore, fundamental output claims of this invention. Secondary claims include a GS falling within the range of 0 to 500 nm.

7.3 Fine Wire Fracture Toughness

ASTM calls out methods for plane strain, as well as, provisional fracture toughness testing in standard E399. Unfortunately, this document does not contain methodologies for the testing of fine wire. Intuitively, though plane stress conditions should clearly be dominant, these materials should still be definable by some metric which quantifies their fracture toughness. A first attempt was made in the F562 alloy system by creating fatigue pre-cracks of random geometry in hard drawn wire. Specimens were then pulled to break in a fast, standard tensile test. Most specimens did exhibit

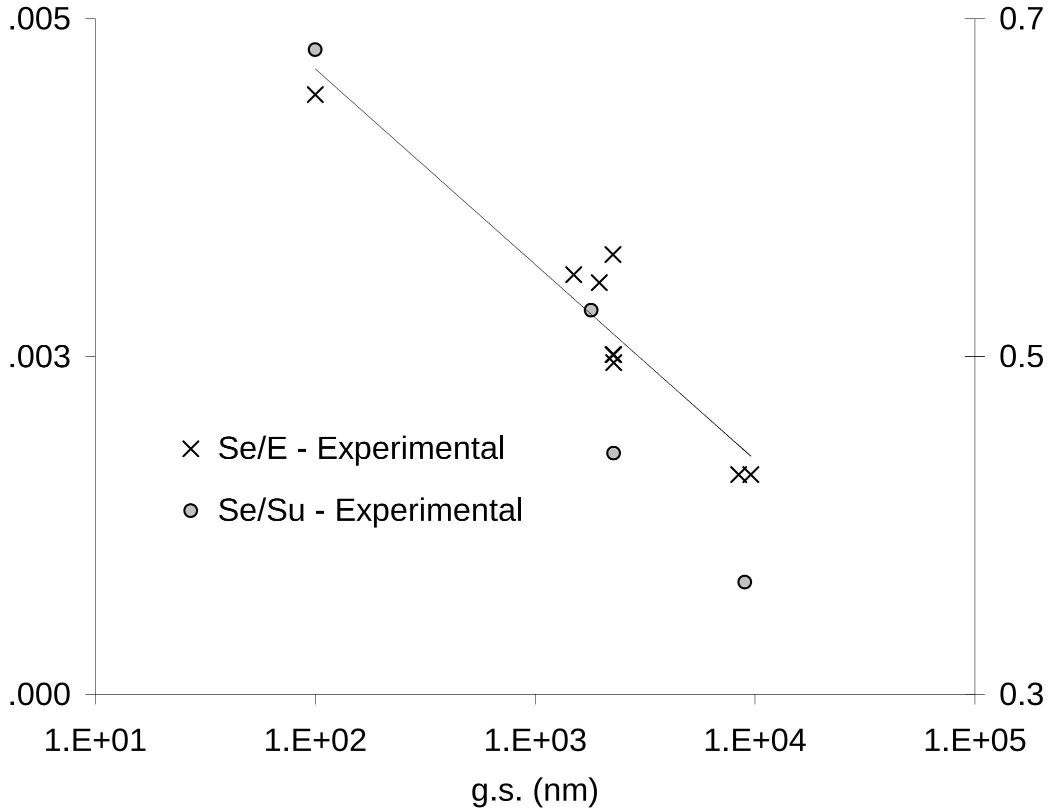

Figure 7.1. Exponential relationship (similar to Hall-Petch relation) between grain size and endurance limit in the ASTM F562 alloy system.

some brittle behavior at definable stress intensity levels, but transitioned quickly to ductile modes. Estimation of early stress intensity loading that precluded the initial stages of fracture were in the 10 - 20 $MPa\sqrt{m}$ range. The results of some of the SEM work carried out to this end are shown in Figures 7.2 through 7.4.

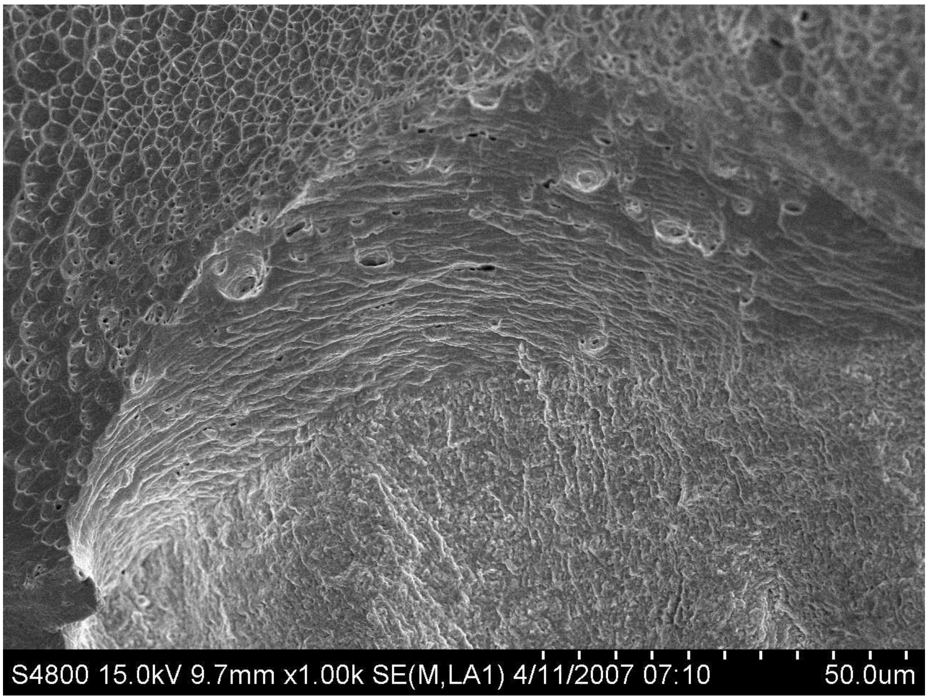

(a) Fatigue pre-crack transition to brittle overload and ultimately into what is primarily a ductile mode 1 failure mode.

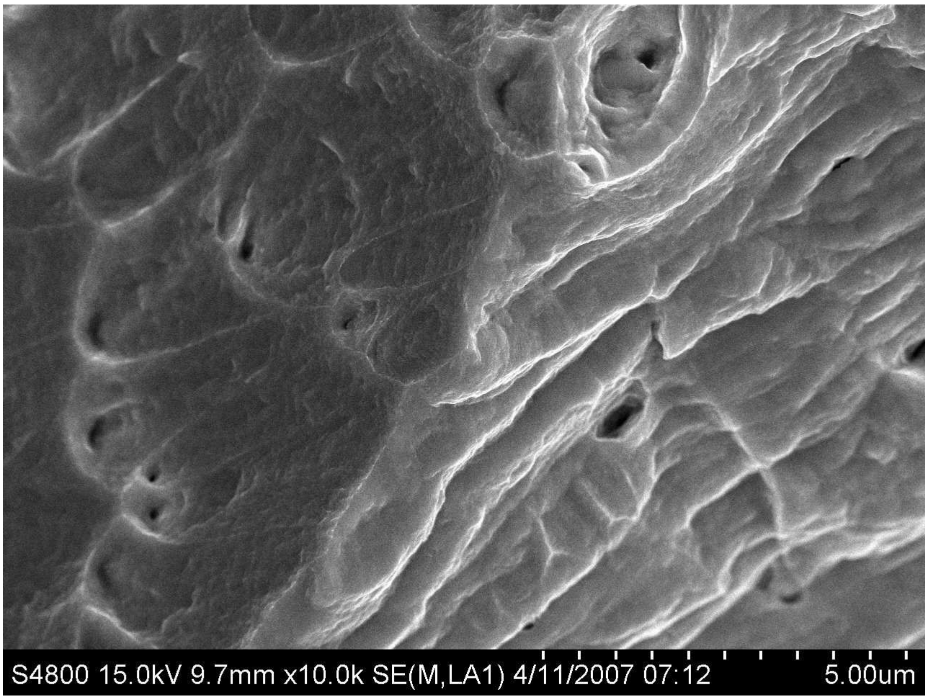

(b) Brittle to ductile zone transition.

Figure 7.2. SEM results from attempted fracture toughness testing on 250 μm 35N LT wire - I.

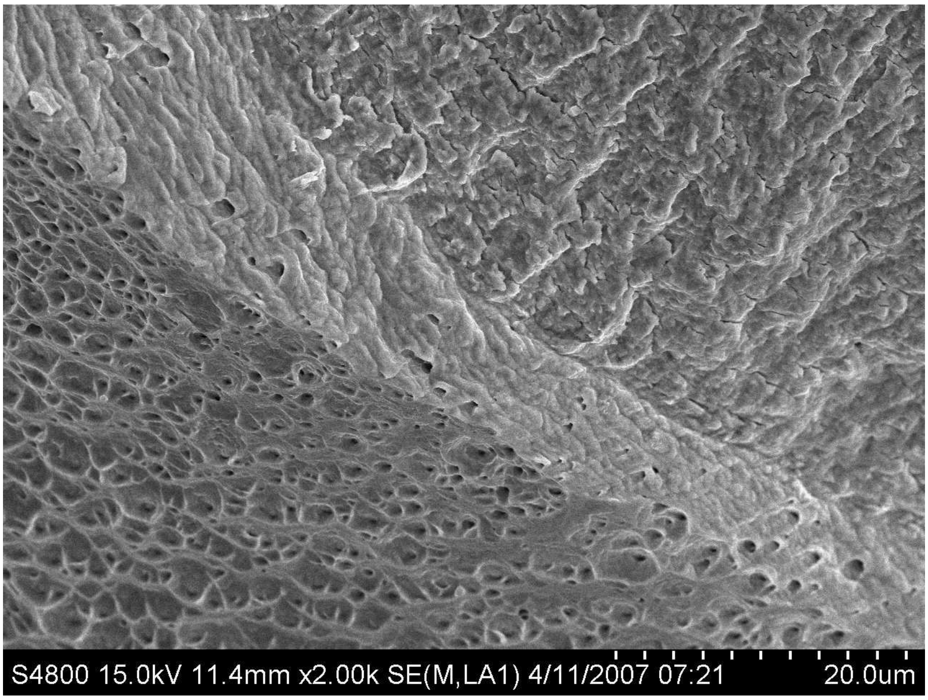

(a) Beginning of ductile fracture near plane stress dominant surface zone.

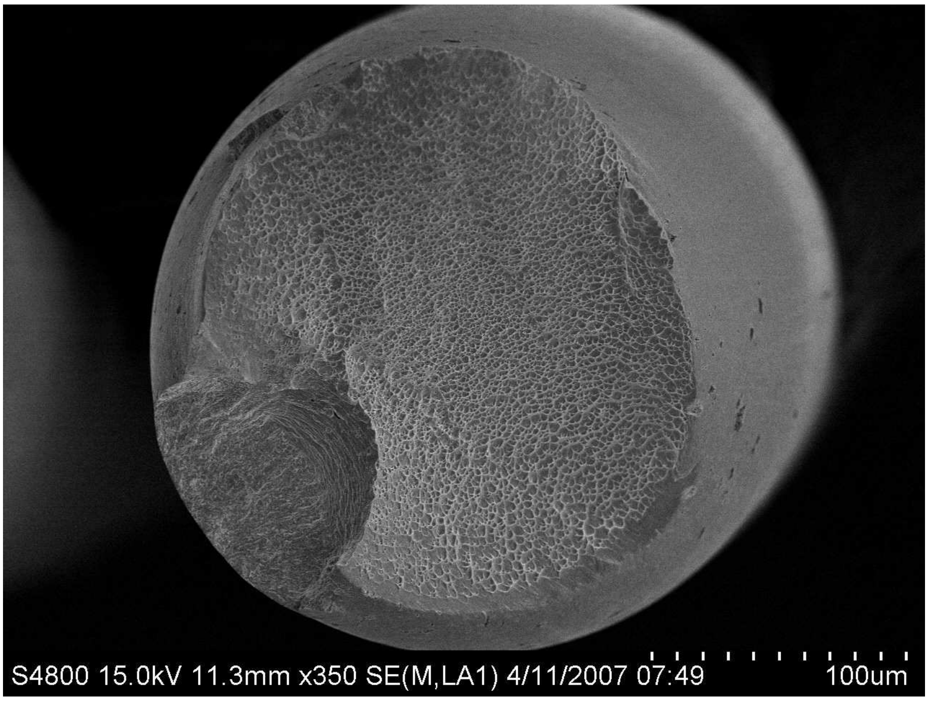

(b) 50 μm x 90 μm fatigue pre-crack loaded to a maximum est. K of 15 $MPa\sqrt{m}$ showing incipient brittle fracture.

Figure 7.3. SEM results from attempted fracture toughness testing on 250 μm 35N LT wire - II.

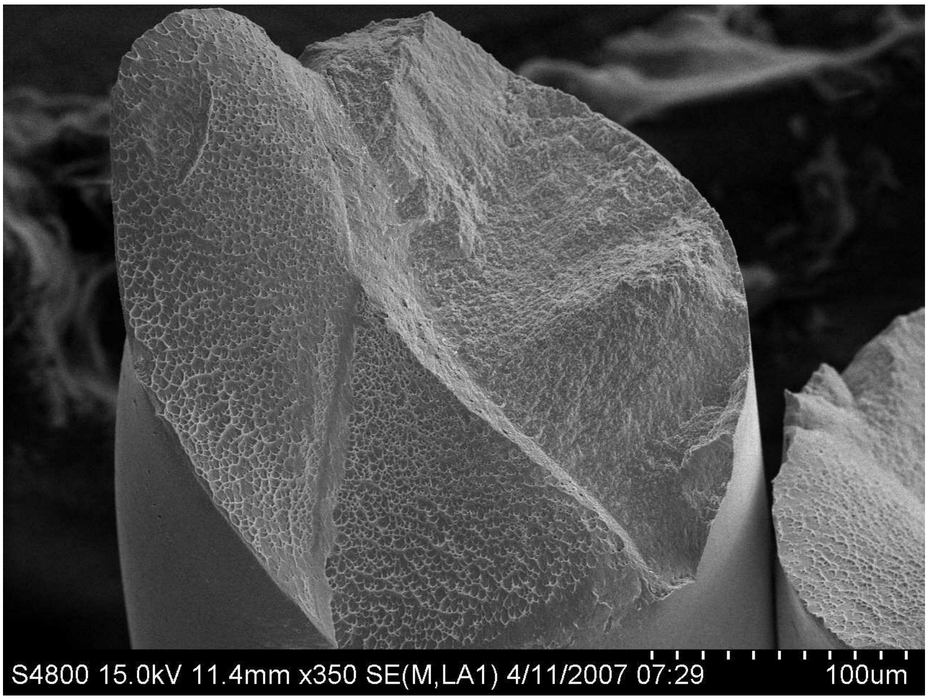

(a) 30 deg. tilted image of fracture toughness specimen.

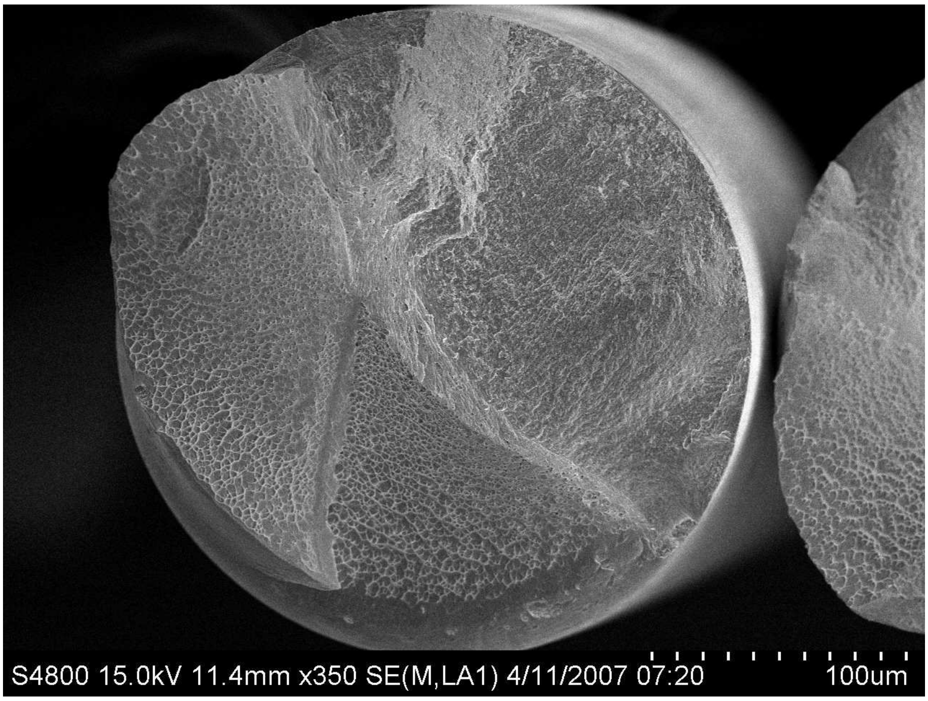

(b) Same as 7.4(a) to show deception in SEM due to depth of field.

Figure 7.4. SEM results from attempted fracture toughness testing on 250 μm 35N LT wire - III.

LIST OF REFERENCES

LIST OF REFERENCES

[1] Leslie A. Geddes and Rebecca Roeder. *Handbook of Electrical Hazards and Accidents*. CRC Press, Inc., BocaRaton, FL, 2 edition, 1995.

[2] Timothy Smith, Sheri Halverson, Hongyan Qiao, Ann Sargent, and Tim Hamann. CRDM product performance report, 2006. Product Report 55, Medtronic, Inc., Minneapolis, MN, 2006.

[3] John M. Herre. Advances in ICD lead technology. *Cardiac Electrophysiology Review*, 5(1):47–51, 2001.

[4] Lawrence Kay, David Bradley, Henry Lippard, and Timothy Stephenson. Optimization of melt chemistry and properties of 35cobalt-35nickel-20chromium-10molybdenum alloy medical grade wire. In *Proceedings of ASM International Materials and Processes for Medical Devices Conference*, MPMD, pages 1–7, Ahaheim, CA, USA, September 2003. ASM Internatinal, ASM International.

[5] Peter A. Altman, James M. Meagher, Daniel W. Walsh, and Drew A. Hoffman. Rotary bending fatigue of coils and wires used in cardiac lead design. *Journal of Biomedical Materials Research*, 43:21–37, 1998.

[6] J.E. Schaffer. DFT biocompatible wire. *Advanced Materials and Processes*, 160(10):51–54, October 2002.

[7] David T. Kawanishi, Susan Song, Seymour Furman, Victor Parsonnet, Guy Pioger, Jean-Claude Petitot, and Jacques-Franois Godin. Failure rates of leads, pulse generators, and programmers have not diminished over the last 20 years: Formal monitoring of performance is still needed. *Pacing and clinical Electrophysiology*, 19(11):1819, November 1996.

[8] Roland Stroobandt, Yves Hagers, Frank Provenier, Yvew Van Belle, Ruben Hamerlijnck, and S. Serge Barold. Silent lead malfunction detected only during defibrillator replacement. *Pacing and Clinical Electrophysiology*, 29:67–69, January 2006.

[9] M. Nabi Sharif, D. George Wyse, John M. Rothschild, and Anne M. Gillis. Changes in pacing lead impedance over time predict lead failure. *American Journal of Cardiology*, 82:600–603, 1998.

[10] Willem G. de Voogt. Pacemaker leads: Performance and progress. *The American Journal of Cardiology*, 83:187–191, 1999.

[11] Brodsky et al. A history of heart failure predicts arrhythmia treatment efficacy: Data from the antiarrythmics versus implantable defibrillators (AVID) study. *American Heart Journal*, 152(4):724–730, October 2006.

[12] Bassam C. Saliba, Robert J. Ardesia, Roy M. John, Ferdinand J. Venditti, and Mark H. Schoenfeld. Predictors of fracture in the accufix atrial j lead. *The American Journal of Cardiology*, 80(2):229–231, July 1997.

[13] P.J. Laz, B.A. Craig, and B.M. Hillberry. A probabilistic total fatigue life model incorporating material inhomogeneities, stress level and fracture mechanics. *International Journal of Fatigue*, 23:119–127, 2001.

[14] Alan E. Baker. *A Probabilistic Fracture Mechanics Method Applied to the Prediction of Low Cycle Fatigue of 2024-T3 Aluminum.* Master of Science in Mechanical Engineering, Purdue University, School of Mechanical Engineering, West Lafayette, IN, December 2002.

[15] Peter Sharpe. *The Application of a Probabilistic Fatigue Life Prediction Method to a High Strength Alloy Steel.* Master of Science in Mechanical Engineering, Purdue University, School of Mechanical Engineering, West Lafayette, IN, December 2001.

[16] Karl M. Gruenberg. *A Probabilistic Method for Predicting the Variability in Fatigue Behavior of 7075-T6 aluminum.* Master of Science in Mechanical Engineering, Purdue University, School of Mechanical Engineering, West Lafayette, IN, December 1997.

[17] Elizabeth A. DeBartolo. *A Material-Based Model of Initial Damage States for Predicting Fatigue Life.* Doctor of Philosophy, Purdue University, School of Mechanical Engineering, West Lafayette, IN, August 2000.

[18] J.E. Schaffer. A probabilistic approach to modeling microstructural variability and fatigue behavior in ASTM F562 medical grade wire. In *Proceedings of the 9th International Fatigue Congress*, Fatigue 2006, Atlanta, GA, May 2006. Georgia Institute of Technology, Elsevier, Inc.

[19] T. Connolley, P.E. McHugh, and M. Bruzzi. A review of deformation and fatigue of metals at small size scales. *Fatigue Fracture of Engineering Material Structures*, 28:1119–1152, 2005.

[20] Herbert Naegele, Sandra Hashagen, Mehmet Ergin, Mojgan Azizi, and Stefan Behrens. Coronary sinus lead fragmentation 2 years after implantation with a retained guidewire. *Pacing and clinical Electrophysiology*, 30(3):438–439, March 2007.

[21] R. Andrew Pickett, Pablo Saavedra, Muhammed F. Ali, Dawood Barbar, and Jeffrey Rottman. Implantable cardioverter-defibrillator malfunction due to mechanical failure of the header connection. *Journal of Cardiovascular Electrophysiology*, 15:1095–1099, September 2004.

[22] The greatest moments in materials science and engineering, JOM The Minerals, Metals and Materials Society. http://www.materialmoments.org/vote.html, 2006. Accessed February 12, 2007.

[23] Superalloys developed by SPS Technologies for aerospace fasteners. Product brochure, SPS Technologies, Jenkintown, PA, USA, March 1998.

[24] Scott Glaze. Private communication. March 2007.

[25] Earl E. Bakken. *One Man's Full Life.* Medtronic, Inc., Minneapolis, MN, USA, 1 edition, 1999.

[26] Walter Schtz. A history of fatigue. *Engineering Fracture Mechanics*, 54(2):263–300, 1996.

[27] J.A. Ewing and W. Rosenhain. The crystalline structure of metals. *Proceedings of the Royal Society of London. Series A, Containing Papers of a Mathematical or Physical Character*, 193:353, 1899.

[28] J.A. Ewing and J.C.W. Humfrey. The fracture of metals under repeated alternations of stress. *Proceedings of the Royal Society of London. Series A, Containing Papers of a Mathematical or Physical Character*, 200:241–250, 1903.

[29] H.J. Gough and D. Hanson. The behaviour of metals subjected to repeated stresses. *Proceedings of the Royal Society of London. Series A, Containing Papers of a Mathematical or Physical Character*, 104(727):538–565, 1923.

[30] A.A. Griffith. The phenomena of rupture and flow in solids. *Proceedings of the Royal Society of London. Series A, Containing Papers of a Mathematical or Physical Character*, 221:163–198, 1921.

[31] G.I. Barenblatt. Scaling phenomena in fatigue and fracture. *International Journal of Fracture*, 138:19–35, 2006.

[32] S. Brinckmann and E. Van der Giessen. Dislocation structures leading to fatigue crack initiation, a discrete dislocation dynamics approach. MicroMechanics Group, University of Groningen, The Netherlands, 2006.

[33] Kwai S. Chan and Michael P. Enright. A probabilistic micromechanical code for predicting fatigue life variability: Model development and application. *Journal of Engineering for Gas Turbines and Power*, 128:889–895, October 2006.

[34] Masaki Nakajima, Nami Kamiya, Hisatake Itoga, Keiro Tokaji, and Haeng-Nam Ko. Experimental estimation of crack initiation lives and fatigue limit in subsurface fracture of a high carbon chromium steel. *International Journal of Fatigue*, 28:1540–1546, 2006.

[35] Kwai S. Chan. A microstructure-based fatigue-crack-initiation model. *Metallurgical and Materials Transactions A*, 34A:43–58, January 2003.

[36] P. Villechaise, L. Sabatier, and J.C. girard. On slip band features and crack initiation in fatigued 316l austenitic stainless steel: Part 1: Analysis by electron back-scattered diffraction and atomic force microscopy. *Materials Science and Engineering A*, A323:377–385, 2002.

[37] K. Shiozawa, L. Lu, and S. Ishihara. S n curve characteristics and subsurface crack initiation behaviour in ultra-long life fatigue of a high carbon-chromium bearing steel. *Fatigue Fracture of Engineering Materials and Structures*, 24:781–790, 2001.

[38] Laurie B. Hildebrand, John A. Schmidt, John K. Prentice, and Larry J. Stotts. Quantitative, low cycle, crack initiation fatigue testing of fine wires and cenelec standard pacing coil. *Journal of Biomedical Material Research*, 48:251–257, 1999.

[39] S.E. Harvey, P.G. Marsh, and W.W. Gerberich. Atomic force microscopy and modeling of fatigue crack initiation in metals. *Acta Metallurgica et Materiala*, 42(10):3493–3502, 1994.

[40] M.R. Lin, M.E. Fine, and T. Mura. Fatigue crack initiation on slip bands: theory and experiment. *Acta Metallurgica*, 34(4):619–628, 1986.

[41] C. Bjerkn. The discrete nature of the growth and arrest of microstructurally short fatigue cracks modelled by dislocation technique. *International Journal of Fatigue*, 27:21–32, 2005.

[42] A.M. Freudenthal. The statistical aspect of fatigue of materials. *Proceedings of the Royal Society of London. Series A, Mathematical and Physical Sciences*, 187(1011):416–429, 1946.

[43] Jr. J.C. Newman, E.P. Phillips, M.H. Swain, and Jr. R.A. Everett. Fatigue mechanics: An assessment of a unified approach to life prediction. In M.R. Mitchell and R.W. Landgraf, editors, *Advances in Fatigue Lifetime Predictive Techniques*, volume 1122 of *ASTM STP 1122*, pages 5–27, Philadelphia, PA, 1992. ASTM, American Society for Testing and Materials.

[44] T. Mura and K. Tanaka. Dislocation dipole models for fatigue crack initiation. *American Society of Mechanical Engineers, Applied Mechanics Division, AMD*, 47:111–131, 1981.

[45] Michael P. Enright and Kwai S. Chan. Extension of a microstructure-based fatigue crack growth model for predicting fatigue life variability. *Journal of ASTM International*, 1(8), 2004.

[46] John A. Newman. *The Effects of Load Ratio on Threshold Crack Growth of Aluminum Alloys.* Doctor of Philosophy in Engineering Mechanics, Virginia Polytechnic Institute and State University, Blacksburg, Virginia, October 2000.

[47] S. Pearson. Initiation of fatigue cracks in commercial aluminium alloys and the subsequent propagation of very short cracks. *Engineering Fracture Mechanics*, 7:235–247, 1975.

[48] H. Kitagawa and S. Takahashi. Applicability of fracture mechanics to very small cracks or the cracks in the early stage. In *Proceedings of the Second International Conference on Mechanical Behaviour of Materials*, pages 627–631. American Society for Metals, ASM, 1976.

[49] R.O. Ritchie. *Small Fatigue Cracks.* TMS, Warrendale, PA, 1 edition, October 1986.

[50] J.C. Newman, E.P. Phillips, and M.H. Swain. Fatigue-life prediction methodology using small-crack theory. *International Journal of Fatigue*, 21:109–119, 1999.

[51] Y. Akiniwa, K. Tanaka, and H. Kimura. Microstructural effects on crack closure and propagation thresholds of small fatigue cracks. *Fatigue Fracture in Engineering Materials and Structures*, 24:817–829, 2001.

[52] Ohchang Jin, Richard W. Hamm, and W. Steven Johnson. Microstructural influences on the growth of small cracks in Ti-6Al-4V. *Fatigue and Fracture of Engineering Materials and Structures*, 25:563–574, 2002.

[53] E. Orowan. Theory of the fatigue of metals. *Proceedings of the Royal Society of London. Series A, Mathematical and Physical Sciences*, 171(944):79–106, 1939.

[54] U.F. Kocks, C.N. Tome, and H.-R. Wenk. *Texture and Anisotropy*. Cambridge University Press, New York, NY,USA, 1998. pages 27-30, 179-208, 367-390.

[55] Ebrahim M. Shaji, Surya R. Kalidindi, Roger D. Doherty, and Aleksandar S. Sedmak. Influence of cold-work and aging heat treatment on strength and ductility of mp35n. *Materials Science and Engineering A*, A272:371–379, 1999.

[56] Ebrahim M. Shaji, Surya R. Kalidindi, Roger D. Doherty, and Aleksandar S. Sedmak. Plane strain fracture toughness of mp35n in aged and unaged conditions measured using modified ct specimens. *Materials Science and Engineering A*, A340:163–169, 2003.

[57] Ebrahim M. Shaji, Surya R. Kalidindi, Roger D. Doherty, and Aleksander S. Sedmak. Fracture properties of multiphase alloy mp35n. *Materials Science and Engineering A*, A349:313–317, 2003.

[58] M.M. Shenoy, R.S. Kumar, and D.L. McDowell. Modeling effects of nonmetallic inclusions on lcf in ds nickel-base superalloys. *International Journal of Fatigue*, 27:113–127, 2005.

[59] Q.Y. Wang, N. Kawagoishi, and Q. Chen. Fatigue and fractre behaviour of structural al-alloys up to very long life regimes. *International Journal of Fatigue*, 28:1572–1576, 2006.

[60] Jr. J.C. Newman. Prediction of crack growth under variable-amplitude loading in thin-sheet 2024-t3 aluminum alloys. Engineering Against Fatigue, University of Sheffield, March 1997.

[61] J. Schijve. Fatigue of structures and materials in the 20th century and the state of the art. *International Journal of Fatigue*, 25:679–702, 2003.

[62] Keith J. Bowman. *Introduction To Mechanical Behavior of Materials*, chapter 7, pages 224–229. Wiley Publishing, Inc., Indianapolis, IN, 1 edition, December 2003.

[63] Andrew Makeev, Yuri Nikishkov, and Erian Armanios. A concept for quantifying equivalent initial flaw size distribution in fracture mechanics based life prediction models. *International Journal of Fatigue*, 29:141–145, 2007.

[64] Joo-Sung Kim, Jae Youn Kang, and Ji-Ho Song. Elucidation of fatigue crack closre behaviour in surface crack by 3-d finite element analysis. *International Journal of Fatigue*, 29:168–180, 2007.

[65] Ramesh V. Marrey, Robert Burgermeister, Randy Grishaber, and R.O. Ritchie. Fatigue and life prediction for cobalt-chromium stents: A fracture mechanics analysis. *Biomaterials*, 27:1988–2000, 2006.

[66] Yongming Liu and Sankaran Mahadevan. Multiaxial high-cycle fatigue criterion and life prediction for metals. *International Journal of Fatigue*, 27:790–800, 2005.

[67] Jr. Shelby Highsmith and W. Steven Johnson. Scatter in fatigue crack growth rate in a directionally solidified nickel-base superalloy. *Journal of ASTM International*, 1(2):1–12, February 2004.

[68] A. Fatemi and L. Yang. Cumulative fatigue damage and life prediction theories: a survey of the state of the art for homogeneous materials. *International Journal of Fatigue*, 20(1):9–34, 1998.

[69] Edwin G. Wintucky, Mark Christopher, Eugene Bahnuik, and Simon Wang. Ion beam sputter etching of orthopedic implant alloy mp35n resulting effects on fatigue properties. (nasa technical memorandum 81747). In *Fifteenth International Electric Propulsion Conference*, pages 1–31, Las Vegas, NV, April 1981. American Institute of Aeronautics and Astronautics and the Japan Society for Aeronautical and Space Sciences, NASA.

[70] D. Hull and D.J. Bacon. *Introduction to Dislocations*. Butterworth Heinemann, Burlington, MA, USA, 1st edition, 2001.

[71] Takayuki Kitamura and Takashi Sumigawa. Slip behavior and locas stress near grain boundary in high-cycle fatigue of copper polycrystal. *JSME International Journal*, 47:92–97, 2004.

[72] J.W. Morris Jr. The influence of grain size on the mechanical properties of steel. *Lawrence Berkeley National Laboratory*, 2001.

[73] Y.Qiao and S.S. Chakravarthula. Effects of randomness of grain boundary resistance on fatigue initiation life. *Internationl Journal of Fatigue*, 27:1251–1254, 2005.

[74] S.S. Chakravarthula and Y. Qiao. Fatigue crack growth in a coarse-grained iron-silicon alloy. *International Journal of Fatigue*, 27:1210–1214, 2005.

[75] G. Venkataraman, Y.W. Chung, and T. Mura. Application of minimum energy formalism in a multiple slip band model for fatigue. *Acta Metallurgia et Materialia*, 39(11):2621–2629, November 1991.

[76] Viggo Tvergaard. Overload effects in fatigue crack growth by crack-tip blunting. *International Journal of Fatigue*, 27:1389–1397, 2005.

[77] S. Pommier and M. Risbet. Time derivative equations for mode i fatigue crack growth in metals. *International Journal of Fatigue*, 27:1297–1306, 2005.

[78] Ray J. Bouthot. Private communication. April 2007.

[79] Bernard Li. Private communication. April 2007.

[80] Ning Yu, Andreas A. Polycarpou, and Amy J. Wagoner Johnson. Measuring mechanical properties of fine-wire cross-sections used in medical devices. *Wiley Periodicals*, pages 106–113, March 2004.

[81] C.T. Fallen, J. Costello, G. Crawford, and J.A. Schmidt. Measuring the elastic properties of fine wire. *Journal of Biomedical Materials Research*, 58(6):694–700, 2001.

[82] E. Mazza, S. Abel, and J. Dual. Experimental determination of mechanical properties of ni and ni-fe microbars. *Microsystem Technologies*, 2:197–202, 1996.

[83] P.S. Prevey. X-ray diffraction residual stress techniques. *Metals Handbook*, 10:380–392, 1986.

[84] Valley Instruments Co., Strongsville, Ohio, USA. *10.040 Fatigue Tester*, est. 1994.

[85] R.E. Wilson. Uses of precise time and frequency in power systems. In *Proceedings of the IEEE*, volume 79, pages 1009–1018, Moscow, ID, July 1991. IEEE, IEEE.

[86] FEI Company, Hillsboro, OR, USA. *Nova 200 NanoLab*, 08/03 edition, August 2003.

[87] S. Kwofie. An exponential stress function for predicting fatigue strength and life due to mean stresses. *International Journal of Fatigue*, 23:829–836, 2001.

[88] S. Kwofie. Equivalent stress approach to predicting the effect of stress ratio on fatigue threshold stress intensity range. *International Journal of Fatigue*, 26:299–303, 2004.

[89] Julie A. Henkener, Victor B. Lawrence, and Royce G. Forman. An evaluation of fracture mechanics properties of various aerospace materials. In ravinder Chona, editor, *Fracture Mechanics: Twenty-Third Symposium*, ASTM STP 1189, pages 474–497, Philadelphia, PA, 1993. American Society for Testing and Materials, ASTM.

[90] Zhiwei Shan, E.A. Stach, J.M.K Wiezorek, J.A. Knapp, D.M. Follstaedt, and S.X. Mao. Grain boundary-mediated plasticity in nanocrystalline nickel. *Science*, 305:654–657, July 2004.

APPENDICES

APPENDICES

Appendix A: Raw Fatigue Data

A.1 Raw Fatigue Data

The results of all fatigue testing are presented in raw form in Table A.1.

Table A.1: Raw fatigue data.

Sample ID	Material	S_{uts} [MPa]	Nominal Test S_a [MPa]	Actual S_a [MPa]	Total Life [cycles]
1	MP35N	2206	862	791	110808
2	MP35N	2206	862	829	169308
3	MP35N	2206	862	852	146196
4	MP35N	2206	862	829	169236
5	MP35N	1310	517	517	306831600
6	MP35N	1310	517	517	288410400
9	MP35N	1310	689	687	792612
10	MP35N	1310	689	687	822888
11	MP35N	1310	689	688	695304
12	MP35N	1310	689	689	743760
13	35N LT	1310	689	681	545148
14	35N LT	1310	689	687	684000
15	35N LT	1310	689	689	457488

continued on next page

Table A.1: *continued*

Sample ID	Material	S_{uts} [MPa]	Nominal S_a [MPa]	Actual S_a [MPa]	Total Life [cycles]
16	35N LT	1310	689	687	793908
17	MP35N	1310	931	928	91080
18	MP35N	1310	931	930	84600
19	MP35N	1310	931	925	93564
20	MP35N	1310	931	930	85860
21	35N LT	1310	931	928	81144
22	35N LT	1310	931	926	83052
23	35N LT	1310	931	923	79128
24	35N LT	1310	931	926	80928
25	MP35N	1931	931	927	53028
26	MP35N	1931	931	928	80820
27	MP35N	1931	931	928	52704
28	MP35N	1931	931	925	86112
29	35N LT	1931	931	921	204264
30	35N LT	1931	931	925	272232
31	35N LT	1931	931	906	137952
32	35N LT	1931	931	922	176580
33	MP35N	1931	1241	1226	27540
34	MP35N	1931	1241	1235	26784
35	MP35N	1931	1241	1235	29268
36	MP35N	1931	1241	1205	23076
37	35N LT	1931	1241	1236	40068
38	35N LT	1931	1241	1239	42948

continued on next page

Table A.1: *continued*

Sample ID	Material	S_{uts} [MPa]	Nominal S_a [MPa]	Actual S_a [MPa]	Total Life [cycles]
39	35N LT	1931	1241	1240	41652
40	35N LT	1931	1241	1241	49428
41	MP35N	2206	1034	1034	21924
41.1	MP35N	2206	1034	1023	30096
41.2	MP35N	2206	1034	1022	31356
41.3	MP35N	2206	1034	1033	30708
42	MP35N	2206	1034	1034	73188
42.1	MP35N	2206	1034	1022	66888
42.2	MP35N	2206	1034	1033	63288
42.3	MP35N	2206	1034	1033	77472
43	MP35N	2206	1034	1034	23148
43.1	MP35N	2206	1034	1009	28872
43.2	MP35N	2206	1034	1026	25164
43.3	MP35N	2206	1034	1023	28908
44	MP35N	2206	1034	1034	69228
44.1	MP35N	2206	1034	1034	62100
44.2	MP35N	2206	1034	1009	79452
44.3	MP35N	2206	1034	1034	61020
44.4	MP35N	2206	1034	1034	18000
45.1	35N LT	2206	1034	1034	178452
45.2	35N LT	2206	1034	1034	214344
45.3	35N LT	2206	1034	1034	207108
45.4	35N LT	2206	1034	1034	207756

continued on next page

Table A.1: *continued*

Sample ID	Material	S_{uts} [MPa]	Nominal S_a [MPa]	Actual S_a [MPa]	Total Life [cycles]
46.1	35N LT	2206	1034	1023	260604
46.2	35N LT	2206	1034	1031	261504
46.3	35N LT	2206	1034	1033	220680
46.4	35N LT	2206	1034	1034	179820
47.1	35N LT	2206	1034	1022	69228
47.2	35N LT	2206	1034	1031	77796
47.3	35N LT	2206	1034	1019	53856
47.4	35N LT	2206	1034	1018	61020
48.1	35N LT	2206	1034	1029	73728
48.2	35N LT	2206	1034	1026	90468
48.3	35N LT	2206	1034	1031	76500
48.4	35N LT	2206	1034	987	83484
57	MP35N	1310	621	618	3104280
58	MP35N	1310	621	620	5194656
59	MP35N	1310	621	620	2817648
60	MP35N	1310	621	620	5912352
61	MP35N	1310	621	619	1909044
62	MP35N	1310	621	614	1983240
62.1	MP35N	1310	621	620	2049372
62.2	MP35N	1310	621	609	2510280
62.3	MP35N	1310	621	616	3340728
62.4	MP35N	1310	621	618	3759156
63	35N LT	1310	621	613	2178216

continued on next page

Table A.1: *continued*

Sample ID	Material	S_{uts} [MPa]	Nominal S_a [MPa]	Actual [MPa] S_a	Total Life [cycles]
64	35N LT	1310	621	620	2928132
65	35N LT	1310	621	615	1813608
66	35N LT	1310	621	613	4064184
67	35N LT	1310	621	620	2879172
68	35N LT	1310	621	613	2177100
69	35N LT	1310	621	620	1693260
70	35N LT	1310	621	616	2882664
71	35N LT	1310	621	620	3056040
72	35N LT	1310	621	616	2845260
73	MP35N	1310	586	586	43999992
74	MP35N	1310	586	586	43999992
75	MP35N	1310 at 1 um GS	689	687	2005020
76	MP35N	1310 at 1 um GS	689	689	3516300
83	35N LT	1310 at 1 um GS	689	689	82584000
84	35N LT	1310 at 1 um GS	689	689	57150000
91	35N LT	1310 at 1 um GS	758	758	1459980
92	35N LT	1310 at 1 um GS	758	758	1093032

continued on next page

Table A.1: *continued*

Sample ID	Material	S_{uts} [MPa]	Nominal S_a [MPa]	Actual S_a [MPa]	Total Life [cycles]
93	35N LT	1310 at 1 um GS	758	758	1437876
94	35N LT	1310 at 1 um GS	758	754	1480716
95	MP35N	1310 at 1 um GS	758	758	704880
96	MP35N	1310 at 1 um GS	758	754	724716
97	MP35N	1310 at 1 um GS	758	752	901836
98	MP35N	1310 at 1 um GS	758	745	1075464
99	MP35N	1310 at 1 um GS	758	756	996120
100	MP35N	1310 at 1 um GS	758	750	903960
101	MP35N	1310 at 1 um GS	758	754	957240
102	MP35N	1310 at 1 um GS	758	756	945000
103	MP35N	1310 at 1 um GS	758	758	517788

continued on next page

Table A.1: *continued*

Sample ID	Material	S_{uts} [MPa]	Nominal S_a [MPa]	Actual S_a [MPa]	Total Life [cycles]
104	MP35N	1310 at 1 um GS	758	752	832392
105	MP35N	1310 at 1 um GS	758	747	659160
106	MP35N	1310 at 1 um GS	758	752	1128996
107	MP35N	1310 at 1 um GS	758	745	845208
108	MP35N	1310 at 1 um GS	758	742	781164
109	MP35N	1310 at 1 um GS	758	739	958752
110	MP35N	1310 at 1 um GS	758	756	535932
111	MP35N	1310 at 1 um GS	758	748	515988
112	MP35N	1310 at 1 um GS	758	754	1007100
113	MP35N	1310 at 1 um GS	758	748	832248
114	MP35N	1310 at 1 um GS	758	754	912024

continued on next page

Table A.1: *continued*

Sample ID	Material	S_{uts} [MPa]	Nominal S_a [MPa]	Actual [MPa]	S_a	Total Life [cycles]
115	35N LT	1310 at 1 um GS	758	752		1297224
116	35N LT	1310 at 1 um GS	758	753		1186200
117	35N LT	1310 at 1 um GS	758	757		2284524
118	35N LT	1310 at 1 um GS	758	749		1968552
119	35N LT	1310 at 1 um GS	758	758		2190132
120	35N LT	1310 at 1 um GS	758	756		2451852
121	35N LT	1310 at 1 um GS	758	756		2707380
122	35N LT	1310 at 1 um GS	758	751		1696500
123	35N LT	1310 at 1 um GS	758	755		1207044
124	35N LT	1310 at 1 um GS	758	755		1269000
125	35N LT	1310 at 1 um GS	758	755		1374264

continued on next page

Table A.1: *continued*

Sample ID	Material	S_{uts} [MPa]	Nominal S_a [MPa]	Actual S_a [MPa]	Total Life [cycles]
126	35N LT	1310 at 1 um GS	758	748	1867356
127	35N LT	1310 at 1 um GS	758	758	2066940
128	35N LT	1310 at 1 um GS	758	757	1935216
129	35N LT	1310 at 1 um GS	758	758	1158732
130	35N LT	1310 at 1 um GS	758	751	1328400
130.1	35N LT	1310 at 1 um GS	758	749	1255644
130.2	35N LT	1310 at 1 um GS	758	755	1760472
130.3	35N LT	1310 at 1 um GS	758	757	2028276
130.4	35N LT	1310 at 1 um GS	758	751	2408724
131	MP35N	1310 at 1 um GS	758	758	967212
132	MP35N	1310 at 1 um GS	758	757	567072

continued on next page

Table A.1: *continued*

Sample ID	Material	S_{uts} [MPa]	Nominal S_a [MPa]	Actual S_a [MPa]	Total Life [cycles]
133	MP35N	1310 at 1 um GS	758	750	846072
134	MP35N	1310 at 1 um GS	758	757	770112
135	MP35N	1310 at 1 um GS	758	758	893088
136	MP35N	1310 at 1 um GS	758	756	908568
137	MP35N	1310 at 1 um GS	758	739	1202040
138	MP35N	1310 at 1 um GS	758	758	707796
139	MP35N	1310 at 1 um GS	758	738	687708
140	MP35N	1310 at 1 um GS	758	758	1054908
151	35N LT	1930	931	926	156456
152	35N LT	1930	931	879	166176
155	35N LT	1930	931	906	140076
156	35N LT	1930	931	883	658800
159	35N LT	1930	931	908	125352
160	35N LT	1930	931	913	99756
163	35N LT	1930	931	929	178488

continued on next page

Table A.1: *continued*

Sample ID	Material	S_{uts} [MPa]	Nominal S_a [MPa]	Actual S_a [MPa]	Total Life [cycles]
164	35N LT	1930	931	915	131724
167	35N LT	1930	827	822	7973316
168	35N LT	1930	827	741	16912656
169	35N LT	1930	827	825	162576
170	35N LT	1930	827	817	12976020
171	35N LT	1930	827	810	198000
172	35N LT	1930	827	819	648324
180	35N LT	1310	621	606	4899996
181	35N LT	1310	621	620	2604420
182	35N LT	1310	621	620	1998360
183	35N LT	1310	621	620	2907468
184	35N LT	1310	621	617	3308832
185	35N LT	1310	621	615	2807136
186	35N LT	1310	621	620	1435320
187	35N LT	1310	621	612	4375548
188	35N LT	1310	621	610	1853244
189	35N LT	1310	621	619	2757672
190	35N LT	1310	621	616	3932892
191	35N LT	1310	621	618	1949868
192	35N LT	1310	621	618	2517156
193	35N LT	1310	621	608	2440440
194	35N LT	1310	621	620	1904796
195	35N LT	1310	621	618	2690532

continued on next page

Table A.1: *continued*

Sample ID	Material	S_{uts} [MPa]	Nominal S_a [MPa]	Actual S_a [MPa]	Total Life [cycles]
196	35N LT	1310	621	620	3435516
197	35N LT	1310	621	620	3094380
198	35N LT	1310	621	620	2310156
200	35N LT	1930	758	758	30780000
201	35N LT	1930	965	963	1643616
202	35N LT	1930	896	896	38912400
203	35N LT	1930	758	758	34920000
204	35N LT	1930	965	964	374904
205	35N LT	1930	896	894	683280
209	35N LT	1930	896	896	665388
210	35N LT	1930	896	895	719100
211	35N LT	1930	896	895	684000
212	35N LT	1930	896	891	711036
215	35N LT	5 um GS	621	620	123480
216	35N LT	5 um GS	448	442	706716
217	35N LT	5 um GS	689	680	1059192
218	35N LT	5 um GS	689	680	846540
219	35N LT	5 um GS	689	684	18280872
220	35N LT	5 um GS	689	680	1109232
250	MP35N	1931	931	874	74124
251	MP35N	1931	931	918	71892
252	MP35N	1931	931	926	72072
253	MP35N	1931	931	918	65232

continued on next page

Table A.1: *continued*

Sample ID	Material	S_{uts} [MPa]	Nominal S_a [MPa]	Actual S_a [MPa]	Total Life [cycles]
254	MP35N	1931	931	924	65700
255	MP35N	1931	931	921	72540
256	MP35N	1931	931	914	73080
257	MP35N	1931	931	881	74376
258	MP35N	1931	931	928	61776
259	MP35N	1931	931	931	60300
260	MP35N	1931	931	924	60588
261	MP35N	1931	931	931	62280
262	MP35N	1931	931	924	60516
263	MP35N	1931	931	927	69516
264	MP35N	1931	931	918	73008
265	MP35N	1931	931	919	66996
266	MP35N	1931	931	930	65448
267	MP35N	1931	931	930	78804
268	MP35N	1931	931	918	66384
269	MP35N	1931	931	914	66204
270	MP35N	1931	931	910	64116
271	MP35N	1931	931	926	61344
272	MP35N	1931	931	888	60768
273	MP35N	1931	931	905	78948
274	MP35N	1931	931	925	61452
275	MP35N	1931	931	931	62460
276	MP35N	1931	931	929	62748

continued on next page

Table A.1: *continued*

Sample ID	Material	S_{uts} [MPa]	Nominal S_a [MPa]	Actual S_a [MPa]	Total Life [cycles]
277	MP35N	1931	931	931	60948
278	MP35N	1931	931	926	58284
279	MP35N	1931	931	919	71604
280	MP35N	1931	689	687	212400
281	MP35N	1931	689	687	221940
282	MP35N	1931	689	677	159624
283	MP35N	1931	689	676	166320
284	MP35N	1931	689	689	177588
285	MP35N	1931	689	689	165312
286	MP35N	1931	689	678	200556
287	MP35N	1931	689	689	204516
288	MP35N	1931	689	689	438876
289	MP35N	1931	689	683	225612
290	MP35N	1931	689	689	220464
291	MP35N	1931	689	683	176508
292	MP35N	1931	689	680	313380
293	MP35N	1931	689	687	200376
294	MP35N	1931	689	683	218268
295	MP35N	1931	689	687	183420
296	MP35N	1931	689	687	245880
297	MP35N	1931	689	686	246060
298	MP35N	1931	689	670	190332
299	MP35N	1931	689	678	216144

continued on next page

Table A.1: *continued*

Sample ID	Material	S_{uts} [MPa]	Nominal S_a [MPa]	Actual S_a [MPa]	Total Life [cycles]
300	35N LT	2300	758	758	12632400
301	35N LT	2300	931	931	17334000
302	35N LT	2300	1034	1027	18944460
303	35N LT	2300	1241	1229	238608
304	35N LT	2300	1172	1170	217764
305	35N LT	2300	1103	1023	352512
316	MP35N	1931	689	689	15012
317	MP35N	1931	689	689	15012
318	MP35N	1931	689	689	15012
319	MP35N	1931	689	689	15012
320	MP35N	1931	689	689	15012
321	MP35N	1931	689	689	15012
322	MP35N	1931	689	689	15012
323	MP35N	1931	689	689	15012
324	MP35N	1931	689	689	15012
325	MP35N	1931	689	689	15012
326	MP35N	1931	689	689	99972
327	MP35N	1931	689	689	99972
328	MP35N	1931	689	689	99972
329	MP35N	1931	689	689	99972
330	MP35N	1931	689	689	99972
331	MP35N	1931	689	689	99972
332	MP35N	1931	689	689	99972

continued on next page

Table A.1: *continued*

Sample ID	Material	S_{uts} [MPa]	Nominal S_a [MPa]	Actual S_a [MPa]	Total Life [cycles]
333	MP35N	1931	689	689	99972
334	MP35N	1931	689	689	99972
335	MP35N	1931	689	689	99972
336	MP35N	1931	621	620	430236
337	MP35N	1931	621	618	245016
338	MP35N	1931	621	620	427860
339	MP35N	1931	621	614	529020
340	MP35N	1931	621	617	1066464
341	MP35N	1931	621	617	222912
342	MP35N	1931	621	620	370692
343	MP35N	1931	621	608	359136
344	MP35N	1931	621	612	387468
345	MP35N	1931	621	600	293400
346	MP35N	1931	621	617	387108
347	MP35N	1931	621	614	491760
348	MP35N	1931	621	615	376848
349	MP35N	1931	621	617	355176
350	MP35N	1931	621	600	1067724
351	MP35N	1931	621	619	3720024
352	MP35N	1931	621	620	610560
353	MP35N	1931	621	614	610344
354	MP35N	1931	621	620	286236
355	MP35N	1931	621	620	306432

continued on next page

Table A.1: *continued*

Sample ID	Material	S_{uts} [MPa]	Nominal S_a [MPa]	Actual S_a [MPa]	Total Life [cycles]
356	MP35N	1931	621	620	416916
357	MP35N	1931	621	620	9601524
358	MP35N	1931	621	611	11364732
359	MP35N	1931	621	619	10784052
360	MP35N	1931	621	612	321192
361	MP35N	1931	621	619	4282020
362	MP35N	1931	621	619	12136716
363	MP35N	1931	621	620	639216
364	MP35N	1931	621	620	487044
365	MP35N	1931	621	614	829116
366	MP35N	1931	621	616	382716
367	35N LT	1931	896	893	418500
368	35N LT	1931	896	894	184392
369	35N LT	1931	896	888	207936
370	35N LT	1931	896	888	174672
371	35N LT	1931	896	896	189396
372	35N LT	1931	896	846	296352
373	35N LT	1931	896	894	379944
374	35N LT	1931	896	896	285156
375	35N LT	1931	896	888	283248
376	35N LT	1931	896	888	241092
377	35N LT	1931	827	822	8568000
378	35N LT	1931	827	827	656748

continued on next page

Table A.1: *continued*

Sample ID	Material	S_{uts} [MPa]	Nominal S_a [MPa]	Actual S_a [MPa]	Total Life [cycles]
379	35N LT	1931	827	827	17514000
380	35N LT	1931	827	827	461448
381	35N LT	1931	827	826	769932
382	35N LT	1931	827	787	41554800
383	35N LT	1931	827	827	364212
384	35N LT	1931	827	823	353016
385	35N LT	1931	827	813	476424
386	35N LT	1931	827	815	450684
387	35N LT	1931	827	816	15112800
388	35N LT	1931	827	804	747288
389	35N LT	1931	827	824	20930400
390	35N LT	1931	827	825	17470800
391	35N LT	1931	827	809	26341200
392	35N LT	1931	827	824	917352
393	35N LT	1931	827	827	1725012
394	35N LT	1931	827	826	729180
395	35N LT	1931	827	825	284940
396	35N LT	1931	827	827	439812
397	35N LT	1931	827	808	217260
398	35N LT	1931	827	826	8026848
399	35N LT	1931	827	827	10088316
400	35N LT	1931	827	824	37149048
401	35N LT	1931	827	822	14014980

continued on next page

Table A.1: *continued*

Sample ID	Material	S_{uts} [MPa]	Nominal S_a [MPa]	Actual S_a [MPa]	Total Life [cycles]
402	35N LT	1931	827	820	651276
403	35N LT	1931	827	827	771732
404	35N LT	1931	827	820	705240
405	35N LT	1931	827	827	258264
406	35N LT	1931	827	826	334548
407	35N LT	n1a	1034	1034	43560000
408	35N LT	n1a	1103	1103	637848
409	35N LT	n1a	1103	1103	508860
410	35N LT	n1a	1103	1103	631908
411	35N LT	n1a	1103	1096	806760
412	35N LT	n1a	1103	1096	633024
413	35N LT	n1a	1103	1092	606996
414	35N LT	n1a	1103	1096	716832
415	35N LT	n1a	1103	1103	558180
416	35N LT	n1a	1103	1103	1053396
417	35N LT	n1a	1103	1076	820476
418	35N LT	n1a	1103	1103	4327200
419	35N LT	n1a	1241	1241	9658800
420	35N LT	n1a	1724	1659	26136
421	35N LT	n1a	1517	1497	60480
422	35N LT	n1a	1517	1480	55908
430	35N LT	1930	1482	1482	43092

Appendix B: Model Analysis Sample Code

B.2 Initiation Life Model Input Parameters

The nominal data that was used as input to the initiation life Equations 2.4 and 2.5 for 177 μm MP35N and 35N LT wire are given in Tables B.1, B.2 and B.3. Data listed as "monte carlo" was selected randomly from the statistical distribution given in the text while "not used" refers to data not used for the specific model for that configuration.

Table B.1 Initiation model Input Parameters for 1930 MPa wire.

Parameter	35N LT 1930 MPa	MP35N 1930 MPa	Units
σ_e	758.4	572.3	MPa
μ	89631	89631	MPa
μ'	155000	240000	MPa
λ	0.093	0.175	non dim
M	3	3	non dim
h	0.064	0.064	μm
D	2.5	2.5	μm
c	5	5	μm
ξ	(Monte Carlo)	(Monte Carlo)	μm
α	0.22	0.22	non dim

B.3 Monte Carlo Simulated Inclusion Data

An example of raw, Monte Carlo simulated, inclusion geometry data is presented in Table B.4. In this table, inclusion size and depth were chosen randomly from the appropriate distributions given in the text. Z1 and Z2 are random normal variables of mean zero and standard deviation one that were used for selection from size and depth distributions respectively. The "F-red" is the stress reduction factor related to inclusion depth and random variability along the wire length with respect to the maximally stressed test apex during RBT. The "Local Alternating Stress" gives the

Table B.2 Initiation model Input Parameters for 1310 MPa wire.

Parameter	35N LT 1310 MPa	MP35N 1310 MPa
σ_e	586	586
μ	89631	89631
μ'	not used	not used
λ	0.209	0.209
M	2.5	2.5
h	0.064	0.064
D	(Monte Carlo)	(Monte Carlo)
c	3	3
ξ	not used	not used
α	0.22	0.22

Table B.3 Initiation model input parameters for 1 μm grain size wire.

Parameter	35N LT 1 μm GS	MP35N 1 μm GS
σ_e	690	620
μ	89631	89631
μ'	155000	240000
λ	0.0461	0.0721
M	2.5	2.5
h	0.0014	0.0014
D	(Monte Carlo)	1.8
c	3	3
ξ	not used	(Monte Carlo)
α	0.22	0.12

remote stress experienced at the randomly selected inclusion or defect site. In cases where the initiation life is listed as "exceed", the alternating stress at the inclusion was less than the material's fatigue limit. The CNIF sorting algorithm generally results in finite lifetimes due to the fact that only the most damaging defects are selected based on maximum CNIF for a given sampling size. Any data that makes it through the first round of CNIF evaluation which is non-numeric is kicked out of the final data set.

Table B.4: Example Monte Carlo data simulation and life calculation for MP35N wire.

Z1	Z2	ξ	Inclusion Depth	$\frac{size}{depth}$	F-red	CNIF	Local Alternating Stress	Initiation Life
0.25	1.25	0.84	29.7	0.03	0.65	23.1	812	exceed
0.84	-1.53	1.46	16.8	0.09	0.76	81.7	938	exceed
0.92	2.19	1.58	62.9	0.03	0.29	9.1	363	exceed
2.18	-1.02	5.2	11.1	0.47	0.86	499.4	1065	exceed
-0.19	1.91	0.56	79.5	0.01	0.11	0.9	132	exceed
-0.6	0.81	0.38	5.7	0.07	0.93	76.7	1159	1.60E+10
-0.23	1.06	0.54	31.5	0.02	0.64	13.5	797	exceed
-0.43	0.33	0.44	53.6	0.01	0.39	4	482	exceed
-1.82	2.91	0.12	62.2	0	0.3	0.7	369	exceed
-1.45	1.38	0.17	0.5	0.34	0.99	418.1	1233	8.47E+06
-0.66	-2.9	0.36	6.1	0.06	0.93	67.3	1153	1.86E+11
-0.29	1.63	0.5	19.5	0.03	0.78	24.8	965	exceed
0.63	0.26	1.21	40	0.03	0.54	20.4	676	exceed
-0.48	1.88	0.42	19.5	0.02	0.78	20.9	966	exceed
0.83	1.91	1.45	77.8	0.02	0.12	2.9	154	exceed
-1.28	-0.81	0.2	17.6	0.01	0.8	11.1	992	exceed
-1.13	-0.64	0.23	43.6	0.01	0.5	3.3	623	exceed
0.07	-0.69	0.71	34.4	0.02	0.61	15.8	762	exceed
0.3	-0.16	0.88	31.7	0.03	0.64	22.2	797	exceed
0.2	0.06	0.8	14.1	0.06	0.83	58.7	1035	exceed
1.03	0.85	1.75	80.2	0.02	0.1	2.6	121	exceed

continued on next page

Table B.4: *continued*

Z1	Z2	ξ	Inclusion Depth	$\frac{size}{depth}$	F-red	CNIF	Local Alternating Stress	Initiation Life
0.07	-1.28	0.71	31.5	0.02	0.64	17.8	795	exceed
2.24	0.21	5.5	22.1	0.25	0.75	231.6	929	exceed
1.53	-0.34	2.81	3.7	0.77	0.95	902.1	1179	3.22E+07
-0.29	-1.88	0.5	16.4	0.03	0.81	30.9	1010	exceed
-1.18	-1.36	0.22	2.9	0.08	0.95	89.9	1177	6.02E+08
-0.34	0.4	0.48	23.9	0.02	0.72	18	893	exceed
-0.87	-0.09	0.29	7.7	0.04	0.9	42.8	1121	exceed
1.78	-0.32	3.56	3.6	1	0.94	1162.6	1165	2.88E+08
0.23	0.82	0.83	35.3	0.02	0.59	17	727	exceed
0.64	0.91	1.21	75.4	0.02	0.15	3	187	exceed
0.81	0.07	1.42	5	0.28	0.94	328.4	1162	1.34E+09
0.18	0.92	0.79	27.9	0.03	0.68	23.7	841	exceed
-0.26	1.57	0.52	22.7	0.02	0.74	21.2	924	exceed
0.07	0.38	0.71	38.5	0.02	0.56	12.8	692	exceed
0.28	-1.57	0.87	23.8	0.04	0.73	33.1	908	exceed
-0.57	-0.39	0.39	17	0.02	0.79	22.3	980	exceed
-0.18	0.26	0.56	11	0.05	0.85	53.8	1057	exceed
-0.85	-1.34	0.3	58.4	0.01	0.34	2.1	423	exceed
0.04	0.72	0.69	40.1	0.02	0.54	11.4	664	exceed
-0.8	-0.81	0.31	67.6	0	0.24	1.4	298	exceed
0.49	-1.17	1.05	41.1	0.03	0.51	16.3	639	exceed
0.11	-0.45	0.73	42.5	0.02	0.52	11.1	643	exceed

continued on next page

Table B.4: *continued*

Z1	Z2	ξ	Inclusion Depth	$\frac{size}{depth}$	F-red	CNIF	Local Alternating Stress	Initiation Life
-0.55	0.17	0.4	51	0.01	0.42	4.1	525	exceed
-1.71	-0.5	0.13	33.4	0	0.62	3	767	exceed
0.25	0.62	0.84	49.6	0.02	0.44	9.3	549	exceed
1.22	-0.15	2.11	5.8	0.36	0.92	410.9	1139	exceed
0.98	-0.67	1.68	23.2	0.07	0.74	66.3	917	exceed
-1.06	-1.45	0.24	71.6	0	0.19	0.8	241	exceed
0.1	2.63	0.73	78.4	0.01	0.12	1.3	144	exceed
-1.13	-1.53	0.23	36.2	0.01	0.59	4.6	734	exceed
0.59	-1.58	1.16	22.2	0.05	0.75	48.5	928	exceed
-0.71	-0.31	0.34	2	0.17	0.96	203.5	1196	4.88E+07
-0.58	-0.43	0.38	85.6	0	0.04	0.2	46	exceed
0.85	-0.12	1.48	31.5	0.05	0.65	37.8	802	exceed
0.73	-2.08	1.33	54	0.02	0.39	11.8	479	exceed
0.86	-1.31	1.49	57.6	0.03	0.35	11.1	430	exceed
0.15	0.38	0.76	28.6	0.03	0.68	22.4	840	exceed
0.21	-0.15	0.81	36.8	0.02	0.58	16	725	exceed
-0.48	-0.44	0.42	39.2	0.01	0.54	7.3	672	exceed
0.63	-0.15	1.2	9.7	0.12	0.89	136.8	1100	exceed
-0.07	0.76	0.62	55.1	0.01	0.37	5.2	464	exceed
-0.18	-0.55	0.56	78.5	0.01	0.12	1	144	exceed
-0.47	-0.58	0.43	27	0.02	0.7	13.7	863	exceed
0.92	0.66	1.58	5.9	0.27	0.91	301.1	1125	exceed

continued on next page

Table B.4: *continued*

Z1	Z2	ξ	Inclusion Depth	$\frac{size}{depth}$	F-red	CNIF	Local Alternating Stress	Initiation Life
1.08	1.99	1.84	28.6	0.06	0.68	54	841	exceed
-0.99	-0.59	0.26	36.2	0.01	0.58	5.2	725	exceed
1.19	0.72	2.04	2.1	0.98	0.97	1180.9	1199	5.74E+06
0.58	0.03	1.14	30.6	0.04	0.65	30.1	804	exceed
0.66	-2.18	1.24	12	0.1	0.86	110.6	1073	exceed
0.46	-0.13	1.02	25.5	0.04	0.71	35.2	881	exceed
-0.91	1.06	0.28	70.7	0	0.2	1	250	exceed
0.3	-0.79	0.88	59.3	0.01	0.33	6.2	414	exceed
0.58	-0.48	1.15	41.7	0.03	0.52	18	651	exceed
-0.24	1.3	0.53	41.9	0.01	0.53	8.3	656	exceed
0.4	-0.26	0.97	37.6	0.03	0.58	18.4	714	exceed
-0.8	-0.71	0.31	1.1	0.3	0.97	360.4	1209	1.88E+07
0.29	-0.46	0.87	19.9	0.04	0.77	41.9	957	exceed
0.87	1.58	1.51	72.6	0.02	0.18	4.7	225	exceed
-1.07	-1.93	0.24	30.2	0.01	0.65	6.5	811	exceed
-0.11	-0.07	0.6	62.6	0.01	0.29	3.5	366	exceed
-0.99	1.47	0.26	60.8	0	0.31	1.7	391	exceed
-0.67	-1.87	0.35	6	0.06	0.93	67.6	1153	1.38E+11
-0.45	-0.18	0.44	8.9	0.05	0.9	54.1	1113	exceed
-0.5	0.38	0.42	6.5	0.06	0.93	73.5	1149	3.63E+12
-0.59	0.21	0.38	11.1	0.03	0.86	36.7	1065	exceed
0.71	2.26	1.3	67.6	0.02	0.24	5.7	296	exceed

continued on next page

Table B.4: *continued*

Z1	Z2	ξ	Inclusion Depth	$\frac{size}{depth}$	F-red	CNIF	Local Alternating Stress	Initiation Life
0.84	0.93	1.47	59	0.02	0.33	10.2	410	exceed
0.07	-1.13	0.71	15.1	0.05	0.83	48.1	1024	exceed
-0.95	-0.79	0.27	8.6	0.03	0.9	35.3	1120	exceed
0.01	0.34	0.67	0.1	8.18	0.99	10033.4	1227	2.87E+06
0.3	0.69	0.88	12.6	0.07	0.84	72.9	1043	exceed
0.38	0.49	0.95	3	0.31	0.97	372.5	1198	1.38E+07
-0.53	-0.86	0.4	24	0.02	0.73	15.1	904	exceed
0.22	1.39	0.82	3.3	0.25	0.94	291.8	1173	3.07E+08
1.44	0.52	2.58	10.3	0.25	0.88	274.4	1093	exceed
-1.68	0.07	0.14	42.8	0	0.52	2	642	exceed
0.21	-0.12	0.81	68.5	0.01	0.23	3.4	284	exceed
-0.39	-0.52	0.46	37.9	0.01	0.57	8.6	709	exceed
-0.92	1.93	0.28	42.5	0.01	0.52	4.2	643	exceed
-0.39	-1.07	0.46	32.2	0.01	0.63	11.1	777	exceed
0.24	0.09	0.84	29.9	0.03	0.66	22.8	818	exceed
0.02	-1.02	0.68	2.2	0.31	0.96	373.2	1187	5.99E+07
1.11	-0.24	1.89	51.6	0.04	0.41	18.9	514	exceed
1.58	0.15	2.96	62.7	0.05	0.29	17.3	366	exceed
-1.75	0.06	0.13	45.5	0	0.48	1.7	596	exceed
1.26	0.19	2.18	50.9	0.04	0.42	22.3	523	exceed
0.19	0.43	0.8	65.5	0.01	0.26	3.9	325	exceed
0.92	1.48	1.58	11	0.14	0.86	152.3	1061	exceed

continued on next page

Table B.4: *continued*

Z1	Z2	ξ	Inclusion Depth	$\frac{size}{depth}$	F-red	CNIF	Local Alternating Stress	Initiation Life
0.22	-0.76	0.82	24.4	0.03	0.72	30	895	exceed
0.45	0.03	1.02	46	0.02	0.48	13	589	exceed
-0.31	-1.84	0.5	27.8	0.02	0.68	15.2	848	exceed
-0.85	0.34	0.3	21.6	0.01	0.75	12.8	935	exceed
0.07	-0.04	0.71	63.3	0.01	0.29	4	355	exceed
-0.37	-1.22	0.47	20.2	0.02	0.76	21.6	939	exceed
1.01	-0.91	1.73	18.7	0.09	0.78	89.5	966	exceed
0.54	0.14	1.11	9.5	0.12	0.89	129.7	1107	exceed
-0.4	0.67	0.45	29.9	0.02	0.65	12.3	808	exceed
0.82	0.42	1.45	61.5	0.02	0.3	8.9	378	exceed
0.25	-0.2	0.84	21.5	0.04	0.72	34.9	889	exceed
1.5	0.09	2.73	10.1	0.27	0.86	286.1	1062	exceed
-1.39	0.61	0.18	23.8	0.01	0.71	6.7	886	exceed
-0.39	0.82	0.46	0.1	7.29	1	9029.7	1239	2.22E+06
0.76	0.96	1.36	29.9	0.05	0.66	37	817	exceed
0.65	0.35	1.22	26.1	0.05	0.7	40.8	873	exceed
0.98	-0.03	1.68	30.8	0.05	0.64	43.5	799	exceed
-0.01	-0.91	0.66	2.3	0.29	0.97	350.9	1209	exceed
-0.19	-0.39	0.55	31.2	0.02	0.64	14.1	798	exceed
0.95	0.98	1.63	28.8	0.06	0.66	46.5	821	exceed
0.89	0.64	1.55	34.6	0.04	0.61	33.7	755	exceed
-0.62	-0.76	0.37	11	0.03	0.87	36.3	1078	exceed

continued on next page

Table B.4: *continued*

Z1	Z2	ξ	Inclusion Depth	$\frac{size}{depth}$	F-red	CNIF	Local Alternating Stress	Initiation Life
0.14	-1.08	0.75	0.7	1.05	0.98	1277.2	1211	6.62E+06
-2.3	1.46	0.08	40.5	0	0.54	1.3	674	exceed
-1.81	-1.26	0.12	19.5	0.01	0.77	5.8	952	exceed
-0.73	0.15	0.33	5.2	0.06	0.93	74.8	1157	3.29E+10
-1.13	-0.52	0.23	23.6	0.01	0.73	8.8	911	exceed
-1.63	-1.35	0.14	30.3	0	0.66	3.8	816	exceed
-1.27	-2.12	0.2	12	0.02	0.86	17.8	1065	exceed
0.41	0.89	0.98	42.5	0.02	0.52	14.8	646	exceed
0.34	1.14	0.92	28.5	0.03	0.67	26.8	829	exceed
1.69	0.4	3.28	73.6	0.04	0.17	9.5	213	exceed
-0.5	0.22	0.41	7.1	0.06	0.92	65.8	1137	exceed
-2.06	-0.64	0.1	17.8	0.01	0.8	5.3	988	exceed
-0.12	-1.24	0.59	3.8	0.16	0.96	187.3	1187	6.81E+07
-1.75	-2.44	0.13	34.2	0	0.59	2.7	737	exceed
-0.08	-0.69	0.61	35.9	0.02	0.6	12.7	740	exceed
-0.08	0.6	0.62	4.1	0.15	0.95	176.4	1178	1.81E+08
-0.69	1.17	0.35	10.8	0.03	0.86	34.5	1072	exceed
-0.17	0.46	0.57	18.7	0.03	0.78	29.2	966	exceed
0.44	-1.81	1.01	21.6	0.05	0.74	42.5	913	exceed
-0.83	1.22	0.3	41.6	0.01	0.53	4.8	659	exceed
-0.63	-0.71	0.37	59.4	0.01	0.33	2.5	407	exceed
0.26	0.74	0.85	27	0.03	0.69	26.9	854	exceed

continued on next page

Table B.4: *continued*

Z1	Z2	ξ	Inclusion Depth	$\frac{size}{depth}$	F-red	CNIF	Local Alternating Stress	Initiation Life
1.2	-0.5	2.05	17.4	0.12	0.8	116.8	991	exceed
-1.49	-0.58	0.16	79.5	0	0.11	0.3	130	exceed
-1.98	-0.3	0.1	43.4	0	0.5	1.5	620	exceed
1.66	-0.39	3.17	24.2	0.13	0.71	116.3	887	exceed
1.2	0.43	2.07	16.2	0.13	0.82	129.6	1013	exceed
-2.07	-0.01	0.09	56.5	0	0.36	0.7	452	exceed
-0.72	-0.46	0.34	32.2	0.01	0.63	8.2	788	exceed
0.87	-1.25	1.51	0.3	5.31	0.96	6346.4	1194	1.20E+07
-1.59	-0.7	0.15	55.6	0	0.37	1.2	462	exceed
-1.07	0.93	0.24	31.7	0.01	0.64	6.1	798	exceed
0.04	-0.22	0.69	56.8	0.01	0.35	5.3	434	exceed
0.93	-0.89	1.6	17.4	0.09	0.8	90.7	989	exceed
3.42	0.6	16.73	23.7	0.71	0.73	639.5	904	exceed
0.48	-0.53	1.05	19.7	0.05	0.76	50.2	945	exceed
-0.15	-0.43	0.58	17	0.03	0.8	33.7	992	exceed
-1.74	-1	0.13	8.5	0.02	0.89	16.9	1106	exceed
0.56	-1.01	1.13	32.8	0.03	0.63	26.9	783	exceed
-0.06	0.35	0.63	24.6	0.03	0.72	22.8	895	exceed
-1.01	-1.09	0.26	39.8	0.01	0.55	4.4	682	exceed
-0.65	-1.05	0.36	16.2	0.02	0.82	22.6	1014	exceed
-1.42	-2.12	0.17	2.9	0.06	0.97	72.2	1201	6.58E+07
0.75	0.33	1.35	5.9	0.23	0.93	264.6	1155	1.99E+10

continued on next page

Table B.4: *continued*

Z1	Z2	ξ	Inclusion Depth	$\frac{size}{depth}$	F-red	CNIF	Local Alternating Stress	Initiation Life
-1.18	-0.48	0.22	43.9	0.01	0.49	3	605	exceed
-0.22	1.27	0.54	21	0.03	0.76	24.2	946	exceed
-0.69	-1.53	0.35	39.1	0.01	0.56	6.2	694	exceed
0.44	-0.32	1	41.1	0.02	0.53	16	657	exceed
-0.92	1.23	0.28	27.6	0.01	0.64	8	798	exceed
0.88	-0.16	1.52	5	0.31	0.94	357.2	1170	2.30E+08
-0.77	-0.24	0.32	19.1	0.02	0.78	16.3	968	exceed
0.11	1.79	0.74	50.8	0.01	0.43	7.7	531	exceed
-0.15	-1.99	0.58	22.7	0.03	0.74	23.1	914	exceed
0.63	0.43	1.2	52.2	0.02	0.41	11.8	511	exceed
0.44	-0.33	1.01	0.1	9.59	0.98	11716	1222	2.43E+06
-0.76	0.51	0.33	0.6	0.54	0.99	662.6	1226	6.18E+06
1.88	0.03	3.93	18.3	0.22	0.79	211.9	984	exceed
0.11	-0.42	0.74	52	0.01	0.41	7.2	512	exceed
0.67	-0.37	1.25	4.8	0.26	0.94	308.2	1172	2.35E+08
0.69	1.11	1.27	58.1	0.02	0.35	9.4	429	exceed
-0.09	0.77	0.61	9.6	0.06	0.87	68.2	1081	exceed
-0.91	1.08	0.28	46	0.01	0.48	3.6	597	exceed
-1.53	0.8	0.16	59.2	0	0.33	1.1	410	exceed
-0.63	-0.27	0.37	25.9	0.01	0.68	12	846	exceed
0.13	0.64	0.75	34.4	0.02	0.61	16.5	753	exceed
-0.79	-1.67	0.31	15.7	0.02	0.82	20.4	1018	exceed

continued on next page

Table B.4: *continued*

Z1	Z2	ξ	Inclusion Depth	$\frac{size}{depth}$	F-red	CNIF	Local Alternating Stress	Initiation Life
0.07	3.26	0.71	10.4	0.07	0.88	74.5	1093	exceed
-0.94	0.89	0.27	19.3	0.01	0.78	13.7	971	exceed

B.4 Mathematica CNIF Sorting Algorithm

```
CNIF Sorting algorithm to transform total life prediction data from overall \
defect distributions to life prediction data from only maximally damaging \
defect sites (i.e. the crack - nucleating defect states)
AUTHOR : Jeremy E. Schaffer
Date : 20 - March, 2007
Revision : 1
Material : MP35N
Diameter : 177 micron
Material Strength Level : 1930 MPa

<< LinearAlgebra‘MatrixManipulation‘
<< Statistics‘DataManipulation‘
Needs["Personal‘ExcelDatFile‘"]
(*Read EXCEL Data (.dat files) in for processing*)
{mp1row, mp1col, mp1tab} =
    datFileFromExcel["C:\THESIS\ThesisWIP\Test90K_25.dat"];
{mp2row, mp2col, mp2tab} =
```

```
    datFileFromExcel["C:\THESIS\ThesisWIP\Test100K_25.dat"];
{mp3row, mp3col, mp3tab} =
    datFileFromExcel["C:\THESIS\ThesisWIP\Test135K_25.dat"];
{mp4row, mp4col, mp4tab} =
    datFileFromExcel["C:\THESIS\ThesisWIP\Test90K_25.dat"];
group = 100;
num = 5000;
mp1res = ZeroMatrix[num/group, 2];
mp2res = ZeroMatrix[num/group, 2];
mp3res = ZeroMatrix[num/group, 2];
mp4res = ZeroMatrix[num/group, 2];
temp = ZeroMatrix[group, 2];
For[i = 1, i < (num/group + 1),
  For[j = 1, j < (group + 1),
    temp[[j, 1]] = mp1tab[[j + group*(i - 1), 1]];
    temp[[j, 2]] = mp1tab[[j + group*(i - 1), 3]];
    j++];
  temp2 = DropNonNumeric[temp];
  temp3 = Max[Column[temp2, 1]];
  For[k = 1, k < (Count[Column[temp2, 1], _Real] + 1) && t =!= temp3,
    t = temp2[[k, 1]]; temp4 = temp2[[k, 2]]; k++];
  mp1res[[i, 1]] = temp3;
  mp1res[[i, 2]] = temp4;
  i++]
For[i = 1, i < (num/group + 1),
  For[j = 1, j < (group + 1),
    temp[[j, 1]] = mp2tab[[j + group*(i - 1), 1]];
    temp[[j, 2]] = mp2tab[[j + group*(i - 1), 3]];
    j++];
```

```
    temp2 = DropNonNumeric[temp];
    temp3 = Max[Column[temp2, 1]];
    For[k = 1, k < (Count[Column[temp2, 1], _Real] + 1) && t =!= temp3,
      t = temp2[[k, 1]]; temp4 = temp2[[k, 2]]; k++];
    mp2res[[i, 1]] = temp3;
    mp2res[[i, 2]] = temp4;
    i++]
  For[i = 1, i < (num/group + 1),
    For[j = 1, j < (group + 1),
      temp[[j, 1]] = mp3tab[[j + group*(i - 1), 1]];
      temp[[j, 2]] = mp3tab[[j + group*(i - 1), 3]];
      j++];
    temp2 = DropNonNumeric[temp];
    temp3 = Max[Column[temp2, 1]];
    For[k = 1, k < (Count[Column[temp2, 1], _Real] + 1) && t =!= temp3,
      t = temp2[[k, 1]]; temp4 = temp2[[k, 2]]; k++];
    mp3res[[i, 1]] = temp3;
    mp3res[[i, 2]] = temp4;
    i++]
  For[i = 1, i < (num/group + 1),
    For[j = 1, j < (group + 1),
      temp[[j, 1]] = mp4tab[[j + group*(i - 1), 1]];
      temp[[j, 2]] = mp4tab[[j + group*(i - 1), 3]];
      j++];
    temp2 = DropNonNumeric[temp];
    temp3 = Max[Column[temp2, 1]];
    For[k = 1, k < (Count[Column[temp2, 1], _Real] + 1) && t =!= temp3,
      t = temp2[[k, 1]]; temp4 = temp2[[k, 2]]; k++];
    mp4res[[i, 1]] = temp3;
```

```
  mp4res[[i, 2]] = temp4;
  i++]
cols = Count[Column[mp1res, 1], _Real];
rowtemp = ZeroMatrix[cols, 1];
coltemp = ZeroMatrix[2, 1];
datFileToExcel["C:\THESIS\ThesisWIP\Test90K_25R.dat", rowtemp, coltemp,
    mp1res];
datFileToExcel["C:\THESIS\ThesisWIP\Test100K_25R.dat", rowtemp, coltemp,
    mp2res];
datFileToExcel["C:\THESIS\ThesisWIP\Test135K_25R.dat", rowtemp, coltemp,
    mp3res];
datFileToExcel["C:\THESIS\ThesisWIP\Test90K_25R.dat", rowtemp, coltemp,
      mp4res];*)
```

B.5 Filtered Inclusion Data for Crack-Nucleating Population

Table B.5 shows typical crack-nucleating inclusion data after processing the raw data through the CNIF selection algorithm. Notice that the inclusions are generally (1) larger and (2) shallower than those comprising the overall distribution. In addition, all non numeric (”exceed”) life values have been rejected.

Table B.5: Example of data set after CNIF sorting algorithm for 1930 MPa, MP35N wire.

CNIF	ξ	Inclusion Depth	Initiation Life
3.5E+02	0.37	1.30	7.99E+06
7.6E+02	3.32	5.08	1.52E+09
7.8E+03	0.60	0.09	2.73E+06
8.5E+03	1.69	0.25	6.91E+05

continued on next page

Table B.5: *continued*

CNIF	ξ	Inclusion Depth	Initiation Life
7.9E+02	1.62	2.47	4.30E+06
1.1E+03	1.85	2.09	3.84E+06
2.6E+03	0.64	0.30	8.31E+06
5.9E+03	2.37	0.49	6.16E+05
4.8E+03	1.51	0.39	1.14E+06
1.9E+03	0.47	0.30	3.41E+06
2.2E+03	0.40	0.22	5.18E+06
6.0E+02	2.95	5.64	3.23E+10
9.7E+04	1.54	0.02	1.81E+06
1.4E+03	5.15	4.40	1.84E+07
1.0E+03	1.23	1.49	3.17E+06
7.1E+03	2.34	0.40	3.24E+06
2.4E+03	0.83	0.43	2.05E+06
1.6E+03	2.23	1.70	2.66E+06
2.3E+03	0.72	0.39	1.69E+06
1.0E+04	0.09	0.01	1.26E+07
1.6E+04	0.77	0.06	1.51E+06
2.6E+03	0.61	0.28	1.13E+07
4.1E+03	1.82	0.55	1.13E+06
7.1E+02	2.91	4.81	6.88E+07
1.5E+03	0.79	0.63	4.78E+06
3.7E+03	1.49	0.49	1.79E+06
1.6E+04	14.30	1.11	1.27E+05
4.9E+03	0.80	0.20	1.49E+06
5.1E+03	3.84	0.91	5.57E+05

continued on next page

Table B.5: *continued*

CNIF	ξ	Inclusion Depth	Initiation Life
1.9E+04	0.87	0.06	1.92E+06
5.3E+03	3.25	0.72	2.52E+07
1.6E+04	1.00	0.08	2.02E+06
7.1E+02	0.74	1.27	3.42E+06
3.0E+03	1.83	0.74	3.06E+06
2.7E+03	4.83	2.17	1.24E+06
8.9E+03	5.89	0.81	3.37E+05
8.7E+02	1.75	2.42	3.83E+06
2.9E+03	1.17	0.50	1.32E+06
7.5E+03	2.14	0.35	2.94E+06
2.2E+04	1.03	0.06	2.85E+06
1.0E+04	2.11	0.25	6.11E+05
3.0E+03	1.56	0.63	3.00E+06
8.5E+03	1.54	0.22	8.71E+05
3.8E+03	0.59	0.18	1.96E+07
1.9E+05	0.97	0.01	1.10E+06
3.5E+03	0.74	0.25	2.99E+06
2.5E+03	0.36	0.17	3.56E+07
9.1E+03	7.63	1.00	2.07E+06
8.3E+03	5.20	0.77	4.16E+05
1.3E+03	0.91	0.84	2.94E+06